

**ANALYSIS, DESIGN AND CONTROL OF
PERMANENT MAGNET SYNCHRONOUS MOTORS
FOR WIDE-SPEED OPERATION**

Liu Qinghua

B.Eng., Huazhong University of Science & Technology

M.Eng., Huazhong University of Science & Technology

**A THESIS SUBMITTED
FOR THE DEGREE OF DOCTOR OF PHILOSOPHY
DEPARTMENT OF ELECTRICAL ENGINEERING
NATIONAL UNIVERSITY OF SINGAPORE**

2005

Summary

This thesis presents aspects of analysis, design and control of permanent magnet synchronous motors (PMSMs) for wide-speed operations.

An analytical method has been developed based on d- and q- axis equivalent circuit model of interior PMSMs, which is used to determine the influence of motor parameters and inverter power rating on motor output power capability. This analysis provides design criteria to obtain optimal combination of motor parameters in order to achieve a wide speed range of constant power operation.

Response surface methodology (RSM) has been used to build the second-order empirical model for the estimation of motor parameters. Numerical experiments were designed using modified central composite design and have been conducted using finite element software to fit the second-order model. The developed model by RSM provides an accurate description of effects of rotor geometric design on the motor parameters. The RSM models were then used for the optimization of an interior PMSM for wide speed operation.

The combination of RSM models which are used for estimation of motor parameters, and genetic algorithms which is used for searching method, provides

an effective methodology for the interior PMSM design optimization. Compared to traditional analytical methods, the proposed computational method improves the accuracy of estimating motor parameters, and at the same time reduces computing time and effort in the optimization process. The optimized values were verified using an FEM software.

An experimental method for the determination of d- and q-axis inductances has been proposed based on the load test with rotor position feedback. The accurate measurement of motor parameters not only validate the developed numerical design approach, but also improve the speed and torque control performance over a wide speed range.

The conventional current vector control of interior PMSMs has been implemented for a smooth and accurate speed and torque control. The advantages and disadvantages on the control performance were investigated through theoretical analysis and experimental work. It was noted that the flux-weakening performance of current vector control deteriorates because of the saturation effects of current regulator in the high speed and high current conditions.

Stator flux based modified direct torque control by using space vector modulation has been proposed to overcome the difficulties met in the current vector control. The application of modified direct torque control for interior PMSM drives has been developed through analysis and experimental implementation. Important conditions which are necessary for the applicability of direct torque control to an interior PMSM has been put forward. Compared to conventional current vector control, the proposed control scheme improves the dynamic response on speed

and torque control on the wide-speed operation. Current regulator saturation, the worst degrading factor of torque production in the extended flux-weakening range, is eliminated. The experimental results show modified direct torque control is more suitable for the applications on extended speed range for interior PMSMs.

Acknowledgments

I would like to express my sincere gratitude and appreciation to my supervisors Dr. M. A. Jabbar and Dr. Ashwin M. Khambadkone for their help and advice. Their invaluable and insightful guidance, support and encouragement inspired me in my work.

I am also thankful to Dr. Sanjib Kumar Panda, Head of Electrical Machines and Drives Lab, for his suggestions and help to this work in all possible aspects.

I would like to express my sincere gratitude to Mr. Y. C. Woo, Principal Laboratory Technologist, for his help. In addition, we want to thank Mr. M. Chandra in Electrical Machines and Drives Lab for his constant and immediate help in the mechanical arrangements for my experimental setup.

I would like to thank my colleagues in the laboratory, Mr. Tripathi Anshuman, for his smart ideas and valuable discussions on the motion control application for my work. I also owe many thanks to my friends in the lab: Mr. Liang Zhihong, Mr. Wang Zhongfang, Mr. Shi Chunming, Mr. Zhang Yanfeng, Mr. Nay Lin Htun Aung, Ms. Wu Mei, Mr. Azmi Bin Azeman, Ms. Dong Jing, Ms. Hla Nu Phyu, Ms. Qian Weizhe, Mr. Sahoo Sanjib Kumar and Mr. Ho Chin Kian Ivan for their

precious help with my study at NUS.

I wish to acknowledge the financial support provided by National University of Singapore in the form of a Research Scholarship.

Finally, my dedication is due to my wife and my parents, for their constant support and encouragement.

Contents

Summary	i
Acknowledgments	iv
List of Symbols	xiii
List of Acronyms	xvii
List of Figures	xix
List of Tables	xxvi
1 Introduction	1
1.1 Permanent Magnet Motors	2
1.2 PM motors in Variable Speed Drives	3
1.3 Characteristics of PM Materials	5
1.4 Structure of PMSMs	7

1.5	Literature Review	10
1.5.1	Constant Power Operation of PMSM Drives	10
1.5.2	The Design of PMSMs	12
1.5.3	Numerical Optimization	14
1.5.4	The Control of PMSMs	18
1.6	Research Goals and Methodology	21
1.6.1	Analysis of Constant Power Speed Range for IPMSM Drive	22
1.6.2	Design Optimization of Interior PMSM	23
1.6.3	Control of IPMSM in Wide Speed Operation	24
1.7	Outline of the Thesis	25
2	Analysis of Interior Permanent Magnet Synchronous Motors for Wide-Speed Operation	27
2.1	Introduction	27
2.2	Mathematical Modelling	28
2.3	Theoretical Analysis of Steady-State Operation	33
2.3.1	Current limited maximum torque operation	34
2.3.2	Current and voltage limited maximum power operation	36
2.3.3	Voltage limited maximum power operation	38

2.3.4	Optimum current vector trajectory	41
2.4	Effects of Motor Parameters on Torque-Speed Characteristics	44
2.5	Design Considerations on Constant Power Speed Range	46
2.6	Conclusions	48
3	Determination of Motor Parameters in Interior PMSMs	50
3.1	Introduction	50
3.2	Design of The Stator Winding	51
3.3	Selection of The Rotor Design Variables	55
3.4	Determination of Motor Parameters	59
3.4.1	Analytical Method	59
3.4.1.1	Stator permanent magnet flux linkage	59
3.4.1.2	Calculation of inductances	62
3.4.2	Finite Element Method	66
3.4.3	Response Surface Method	68
3.4.3.1	Building empirical models	68
3.4.3.2	Estimation of the regression coefficients	70
3.4.3.3	Fitting the second-order model	72
3.4.3.4	Model adequacy checking	74

3.5	Design of The Rotor Structure	75
3.6	Conclusion	83
4	Numerical Optimization of an Interior PMSM for Wide Constant Power Speed Range	84
4.1	Introduction	84
4.2	Optimization Method	85
4.2.1	Formulation of the design optimization	85
4.2.2	Description of genetic algorithms	88
4.3	Implementation of Proposed Design Optimization Procedure	93
4.4	Numerical Results and Discussions	93
4.5	Conclusion	103
5	Tests and Performance of the Prototype Interior PMSM	105
5.1	Introduction	105
5.2	The Prototype Interior PMSM	106
5.3	Experimental Interior PMSM Drive System	108
5.3.1	DS1102 controller board	111
5.3.2	PWM voltage source inverter	112
5.3.3	Integrated interface platform	112

5.3.4	Current sensor	114
5.3.5	Loading system	115
5.4	Experimental Determination of Motor Parameters	116
5.4.1	Permanent magnet flux linkage λ_m	116
5.4.2	Torque angle measurement	117
5.4.3	Load test to measure L_d and L_q	120
5.5	Experimental Evaluation of Wide Speed Operation Performance . .	122
5.5.1	Torque and Power Capability	123
5.5.2	Efficiency and Power Factor	125
5.5.3	Performance under Reduced DC Link Voltages	128
5.6	Conclusion	131
6	Control of The Prototype Interior Permanent Magnet Synchronous Motor	133
6.1	Introduction	133
6.2	Field Oriented Current Control Scheme	134
6.2.1	Description and features of the current control scheme . . .	134
6.2.2	Discussions on current control schemes	139
6.3	Space Vector Modulation based Direct Torque Control Scheme . . .	140
6.3.1	Principle of torque production in interior PMSMs	140

6.3.2	Stator flux control in DTC-SVM	142
6.3.3	Calculation of switching on time	145
6.3.3.1	Normal modulation range	147
6.3.3.2	In overmodulation range	148
6.3.4	Stator flux estimation	149
6.3.5	Operating Limits for DTC-SVM scheme in IPMSM drives .	150
6.3.6	Current Constraints	152
6.3.7	Proposed Wide Speed Operation	155
6.4	Description and Features of the Proposed Scheme	158
6.4.1	Speed Range for Operation at Constant Torque	158
6.4.2	Operating in flux-weakening speed range	160
6.5	Experimental Results and Discussions	160
6.6	Conclusion	168
7	Discussions and Conclusions	171
7.1	Discussions of Major Work	171
7.1.1	Analysis of constant power operation	171
7.1.2	Design optimization methodology	173
7.1.3	Steady state tests of the prototype interior PMSM	175

7.1.4	Speed and torque control by DTC-SVM	176
7.2	Major Contributions of the Thesis	177
7.3	Suggestions for Future Research	178
A	Design Details for The Prototype Interior PMSM	195
B	Additional Experimental Data	198

List of Symbols

A_z	cross area of winding conductor
B	damping coefficient
B_{ad}	flux density in air gap due to d-axis armature MMF
B_{aq}	flux density in air gap due to q-axis armature MMF
B_D	knee flux density
B_g	peak flux density in air gap due to magnets
B_r	remanent flux density
B_s	air gap flux density due to armature reaction
B_{1g}	rms value of fundamental flux density in air gap due to magnets
D	inner diameter of stator frame
d_c	bare diameter of conductor
E	rms value of phase back EMF
e_{coil}	back EMF in one coil
F_{ad}	d-axis armature MMF
F_{aq}	q-axis armature MMF
F_{a1}, F_{b1}, F_{c1}	phase fundamental MMF

F	total value of fundamental MMF
f	electrical frequency
f_s	slot space factor
g_e	air gap length including magnet thickness
g	actual uniform air gap length
g'	effective air gap length
H_c	coercive magnetizing force
$I_{a,b,c}$	phase armature current
$I_{d,q}$	d- and q-axis current
I_{ph}	phase current
I_s	current space vector
I_{sm}	current constraints
J	inertial of the rotor
J_c	current density in conductor
K_{1s}	rms value of linear current density
k_c	Carter's effect coefficient
k_d	d-axis inductance factor
k_q	q-axis inductance factor
k_ω	winding factor
$L_{aa,bb,cc}$	phase self inductance
$L_{ab,ac,bc}$	phase mutual inductance

L	stator stack length
L_{ad}	d-axis magnetizing inductance
L_{aq}	q-axis magnetizing inductance
L_{s}	synchronous inductance
l_{m}	magnet thickness
N_{coil}	number of turns per phase in equivalent full pitch winding
N_{ph}	number of turns per phase in actual winding
P	number of poles
P_{in}	motor input power
P_{o}	motor output power
p_{c}	crossover probability
p_{m}	mutation probability
R_{s}	phase resistance
S	number of slots
S_{a}	slot area
T_{e}	motor electromagnetic torque
T_{l}	motor loading torque
t	time, second
$V_{\text{a,b,c}}$	phase terminal voltage
V_{s}	voltage space vector
V_{sm}	voltage constraints
x_1, x_2, x_3	scaled design variables
X_{s}	synchronous reactance

φ	electrical angle in rotor w.r.t d-axis
θ	rotor position angle w.r.t phase A axis
λ_m	stator permanent magnet flux linkage
$\lambda_{a,b,c}$	phase flux linkage
β	current angle
$\lambda_{ma,mb,mc}$	phase flux linkage provided by rotor magnets
$\lambda_{d,q}$	d- and q-axis flux linkage
ω_s	electrical velocity
δ	torque angle
ω_r	mechanical velocity
ω_b	base speed
ω_c	crossover speed
ω_{max}	maximum speed for rated power operation
ω_p	minimum speed for the voltage-limited maximum output power operation
β_b	current angle for maximum torque operation
α	magnet pole angle
γ	magnet position
ϕ	flux in one full pitch winding
μ_0	permeability in air gap
μ_r	relative permeability in magnets
ϵ	voltage adjusting coefficient

List of Acronyms

AC	Alternating Current
AM	Analytical Method
BLDC	Brushless DC
CPSR	Constant Power Speed Range
CVC	Current Vector Control
DC	Direct Current
DFC	Direct Flux Control
DSP	Digital Signal Processor
DTC	Direct Torque Control
EMF	Electro-motive Force
FEM	Finite Element Method
GA	Genetic Algorithms
MMF	Magneto-motive Force

MTPA	Maximum Torque Per Ampere
PI	Proportional Integral
PM	Permanent Magnet
PMSM	Permanent Magnet Synchronous Motor
PWM	Pulse Width Modulation
RMS	Root Mean Square
RSM	Response Surface Methodology
SD	Slot Depth
SWF	Slot Width Factor
SVM	Space Vector Modulation
THD	Total Harmonic Distortion

List of Figures

1.1	Basic excitation waveform for (a) sinusoidal and (b) trapezoidal PM ac motors	4
1.2	Characteristics of Permanent Magnet Materials	6
1.3	Structures for exterior permanent magnet motors	8
1.4	Structures for interior permanent magnet motors	8
1.5	Ideal Torque vs. speed characteristics for variable speed AC drives .	10
1.6	Cross section of axially laminated rotor for interior PMSM [16] . . .	13
1.7	Cross section of rotor with $L_q/L_d < 1$ for interior PMSM [17]	14
1.8	Two-part rotor with $L_q/L_d < 1$ for interior PMSM [18]	15
2.1	Permanent magnet synchronous motor	29
2.2	Equivalent Circuit of an interior PMSM	31
2.3	The stator flux linkage in the dq reference frame	32

2.4	The current limit circle and voltage limit ellipse for interior PMSMs	34
2.5	The optimum current vector trajectory in the d-q coordinate plane for $\lambda_m < L_d I_{sm}$	40
2.6	The optimum current vector trajectory in the d-q coordinate plane for $\lambda_m > L_d I_{sm}$	43
2.7	The maximum obtainable torque vs. speed profile	43
2.8	Torque vs. speed characteristics with optimum current vector tra- jectory	44
2.9	Torque-speed characteristics with different magnet flux linkages	45
2.10	Torque-speed characteristics with different q-axis inductance	46
2.11	Torque-speed characteristics with different d-axis inductances	47
2.12	Comparison of power vs. speed characteristics for 5 designs	48
3.1	Stator frame structure	52
3.2	Stator and rotor structure for interior PMSMs	56
3.3	Permanent magnet excitation flux plot	56
3.4	Permanent magnet excited flux distribution in the air gap	57
3.5	Rotor configuration of the interior PMSM	58
3.6	Actual and effective air gap flux density	60

3.7	Air gap flux distribution due to permanent magnet	61
3.8	MMF distribution of an interior PMSM over 180°	63
3.9	Air gap profile along the rotor surface	64
3.10	Central composite design for second-order model	73
3.11	λ_m as a function of rotor geometry	81
3.12	L_d as a function of rotor geometry	82
3.13	L_q as a function of rotor geometry	83
4.1	Determination of maximum power capability w.r.t to motor speed .	87
4.2	Main steps of genetic algorithms technique	89
4.3	Example of one individual of design variable	91
4.4	Schematic samples of crossover and mutation process	92
4.5	Flowchart for the proposed design optimization of the interior PMSM	94
4.6	Average and maximum CPSR trend combining GA and RSM . . .	95
4.7	Effects of magnetic saturation on L_d and L_q	97
4.8	Permanent magnet excited flux distribution in the air gap	98
4.9	Air gap flux density curve with maximum flux-weakening condition $\beta = 180$ degree	98

4.10	The stator flux linkage in the dq reference frame	99
4.11	The optimum current vector trajectory in the d-q coordinate plane for $\lambda_m > L_d I_{sm}$	100
4.12	Torque vs. current angle β characteristics for FEM and RSM	100
4.13	Stator flux vs. current angle β characteristics for FEM and RSM . .	101
4.14	Power capability vs speed characteristics for the optimized design by FEM and RSM	101
4.15	Comparison of optimal design with other design cases	103
5.1	Hardware schematic of the interior PMSM drive system	106
5.2	The optimized rotor structure for the prototype interior PMSM . .	107
5.3	Standard stator and designed rotor for the prototype interior PMSM	107
5.4	Experimental set-up for the interior PMSM drive system	108
5.5	dSPACE DS1102 based integrated PMSM drive test platform . . .	109
5.6	Configuration of the controller board used for hardware implemen- tation	110
5.7	Interfacing the controller board with the control circuit	113
5.8	Configuration for the interior PMSM loading system	115
5.9	PMSM generator phasor diagram for testing	118

5.10	Experimental measurement of d-axis position	118
5.11	Experimental measurement of load angle	119
5.12	Experimental results for the maximum torque capability vs. speed .	125
5.13	Experimental results for the maximum power capability vs. speed .	126
5.14	Experimental results for the efficiency for constant current and full voltage operation	127
5.15	Experimental results for the power factor for constant current and full voltage operation	128
5.16	Experimental results for the torque capability for constant current and reduced DC link voltage operation	129
5.17	Experimental results for the power capability for constant current and reduced DC link voltage operation	130
5.18	Experimental results for the efficiency for constant current and re- duced DC link voltage operation	130
5.19	Experimental results for the power factor for constant current and reduced DC link voltage operation	131
6.1	The optimum current profile in the d-q coordinate plane for $\lambda_m >$ $L_d I_{sm}$	135
6.2	Block diagram of current controlled IPMSM drive system	135
6.3	Current regulator with decoupling feedforward compensation	137

6.4	The stator flux linkage in the dq reference frame	141
6.5	The steady state operation of stator flux control	144
6.6	Three-phase converter and phase voltage	146
6.7	Switching state vectors in the $\alpha - \beta$ plane	146
6.8	Space vector modulation with switching state vectors	147
6.9	Modified voltage model for flux estimation	149
6.10	The torque vs. load angle characteristics	151
6.11	The phase current vs. load angle characteristics	153
6.12	The comparison of maximum load angle: δ_{m0} and δ_{m1} Vs. λ_s	154
6.13	The characteristics of torque capability vs. stator flux linkage . . .	156
6.14	The Stator Flux Reference Profile: (a) Constant torque operation with MTPA control; (b) Flux-weakening Operation	157
6.15	Block diagram of IPMSM drive system	159
6.16	Current Control: The dynamic response with step speed change in the normal range	162
6.17	SVM based DTC: The dynamic response with step speed change in the normal range	162
6.18	Current Control: The dynamic response with step loading torque change in constant torque speed range	163

6.19 SVM based DTC: The dynamic response with step loading torque change in constant torque speed range	164
6.20 Current Control: The dynamic response with step speed change in flux-weakening range	165
6.21 SVM based DTC: The dynamic response with step speed change in flux-weakening range	166
6.22 Dynamic response of the IPMSM drive system in transition from constant torque to flux-weakening regions	167
6.23 Flux Weakening Operation with the variation of DC link voltage . .	167
6.24 Transient performances of flux and voltage for step speed change in flux-weakening range	168
6.25 Torque performance of SVM based DTC and Current Control for a wide speed operation	169
6.26 Power performance of SVM based DTC and Current Control for a wide speed operation	170
A.1 Rotor mechanical design drawing	195
A.2 Stator winding distribution	196
A.3 Magnet design specification	197

List of Tables

1.1	Comparison between PMSMs with exterior and interior magnets . .	9
2.1	Motor parameters for 5 Interior PMSMs	48
3.1	Stator frame data for the prototype interior PMSM	53
3.2	Specifications of the Interior PMSM	53
3.3	Winding specifications for the prototype interior PMSM	55
3.4	Data for multiple linear regression	71
3.5	The domain of design variables in the rotor structure	75
3.6	Central composite design for the design example of interior PMSM .	76
3.7	Comparison of results with AM, FEM and RSM	79
3.8	Residual for the fitted second-order RSM model	80
3.9	Test of adequacy for the fitted second-order RSM model	80

4.1	The domain of design variables in the rotor structure	90
4.2	Optimized design values and motor parameters	96
4.3	Comparison of motor parameters with GA+RSM and FEM	96
4.4	Comparison of flux distribution for open circuit and flux-weakening condition	99
4.5	Comparison of 9 design cases	102
5.1	Experimental measurements of back EMF and calculated values of λ_m	117
5.2	Experimental measurements of L_d and L_q	121
5.3	Comparison of motor parameters with The Commercial and The Prototype	123
5.4	Test Condition with The Commercial and The Prototype	124
6.1	Base values of motor parameters	161

Chapter 1

Introduction

Permanent magnet synchronous motors (PMSMs) are increasingly used in variable speed industrial drives. New developments and applications have been greatly accelerated by improvements in permanent magnet (PM) materials, especially rare-earth magnets. While the methods for analysis and design of conventional AC electrical machines are becoming mature, extensive research is still required to develop a systematic methodology for analysis, design and control of PMSMs.

In this thesis, a design and control method for PMSMs is developed based on the analysis of PMSMs with different rotor structures. The prototype PMSM was designed to achieve a wide-speed and constant power operation. Tests made on the fabricated prototype motor prove the validity of the design optimization methodology and control algorithm developed.

1.1 Permanent Magnet Motors

The use of permanent magnets (PM) in construction of electrical machines brings the following benefits [1]:

- no electrical energy is absorbed by the field excitation system and thus there are no excitation losses which means substantial increase in the efficiency
- higher torque and output power per unit volume compared to electromagnetic excitation
- better dynamic performance than motors with electromagnetic excitation (higher magnetic flux density in the air gap)
- simplification of construction and maintenance
- reduction of lifetime cost for some types of machines.

Cage induction motors have been the most popular electric motors in the 20th century. Recently, owing to the fast progress made in the field of power electronics and control technology, the applications of induction motors to electrical drives have increased. The main advantages of cage induction motors are their simple construction, easy maintenance, no commutator or slip rings, low price and high reliability. The disadvantages are their lower efficiency and poorer power factor than PM synchronous motors.

The use of PM motors in electrical drives has become a more attractive option than induction motors. The improvements made in the field of semiconductor drives mean that the control of PM motors has become easier and cost effective with the possibility of operating the motor over a large speed range and still maintaining a good efficiency and power factor. The price of rare earth magnets are also coming down making these motors more popular.

1.2 PM motors in Variable Speed Drives

In a variable-speed drive or servo drive system, a speed or position feedback is used for precision control of motors. The response time and the accuracy with which the motor follows the speed and position commands are important performance parameters. A power electronic converter interfaces the power supply and the motor. Industrial drives technology has changed in recent years from conventional DC or two-phase AC motor drives to new maintenance-free brushless three-phase vector-controlled AC drives for all motor applications where quick response, light weight and large continuous and peak torques are required.

Permanent magnet ac motors combine some of the desirable advantages of conventional induction and synchronous motors and deserve special attention. Permanent magnet motors can be classified into two categories, one group is sinusoidally excited and the other is square wave (trapezoidally excited) motors [2]. Motors with a sinusoidal excitation are fed with three-phase sinusoidal waveforms (Fig. 1.1 (a)) and operate on the principle of a rotating magnetic field. They are

simply called sinewave motors or permanent magnet synchronous motors (PMSMs).

All phase windings conduct current at the same time.

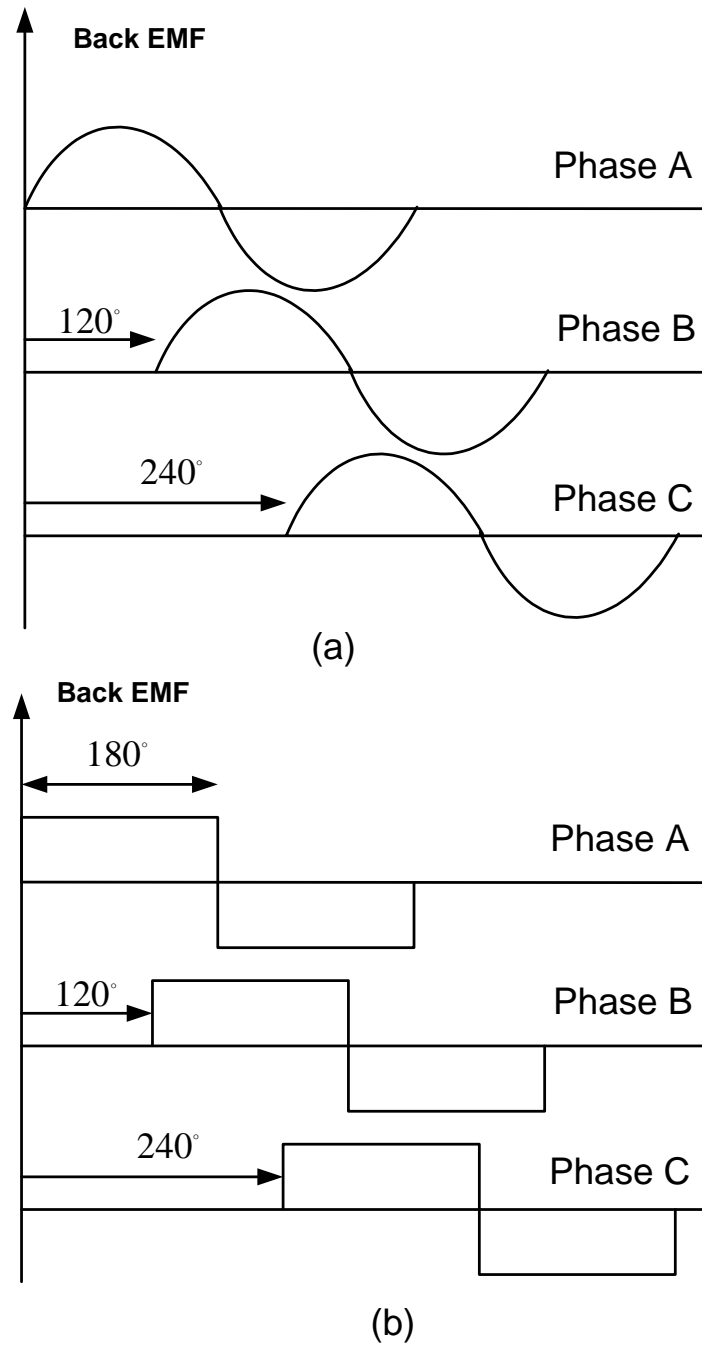


Figure 1.1: Basic excitation waveform for (a) sinusoidal and (b) trapezoidal PM ac motors

Square wave motors are also fed with three-phase waveforms shifted one from

another by 120° , but these waveshapes are rectangular or trapezoidal as shown in Fig. 1.1 (b). Such a shape is produced when armature current (MMF) is precisely synchronized with the rotor instantaneous position and frequency (speed) [3]. The most direct and popular method of providing the required rotor position information is to use an angular position sensor mounted on the rotor shaft. Such a control scheme or electronic commutation is functionally equivalent to the mechanical commutation in DC motors. This explains why motors with squarewave excitation are called brushless DC motors (BLDC). These two kinds of permanent magnet motors are different in performance and control. In this research, the emphasis was placed on permanent magnet synchronous motors.

PMSMs have been broadly developed for industrial applications such as servo motors, elevator drive motors, and electric vehicle traction motors [4]. At the same time, the development in high-strength rare-earth permanent magnet materials, especially neodymium alloyed with iron and boron (NdFeB), have greatly enhanced the potential applications of PMSMs. Before discussing design configurations of PMSMs, it is necessary to understand the characteristics of permanent magnet materials used in electric motors for excitation.

1.3 Characteristics of PM Materials

The development of permanent magnets with high flux density and large coercive force resulted in the wide use of PMSM drives with high performance. Three main magnetic materials are used in PMSM. They are: Ferrite, samarium-cobalt and

neodymium-iron-boron (NdFeB). Characteristic demagnetization curves for these magnet materials are shown in Fig. 1.2. Ferrite material is low in cost and has

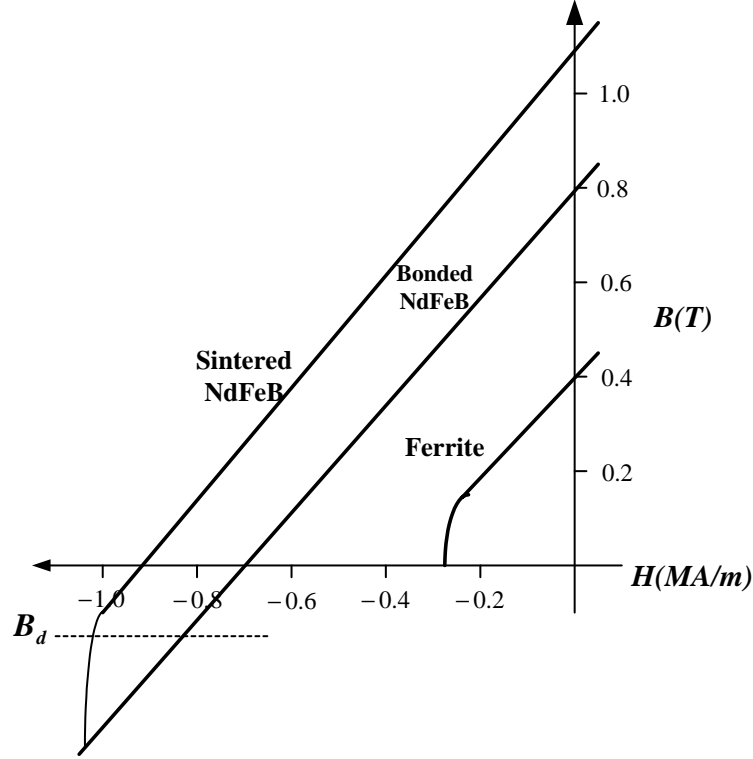


Figure 1.2: Characteristics of Permanent Magnet Materials

excellent linearity in demagnetization, but the remanence is low. So it occupies big rotor space. Samarium-Cobalt has substantially increased residual flux density and coercivity as compared with ferrites, but the cost is rather high which limits its application. Both ferrites and Samarium cobalt are hard and brittle. Since the introduction of neodymium-iron-boron (NdFeB) magnet materials 1980s, increased attention has been given to the application of these materials in PMSM. It has been shown that NdFeB magnets have the similar merits as Ferrite and Samarium-Cobalt but have lower cost. High air gap flux density of 0.8-1.0 T can be produced with relatively small magnet volume using these magnets. Furthermore, PMSMs using

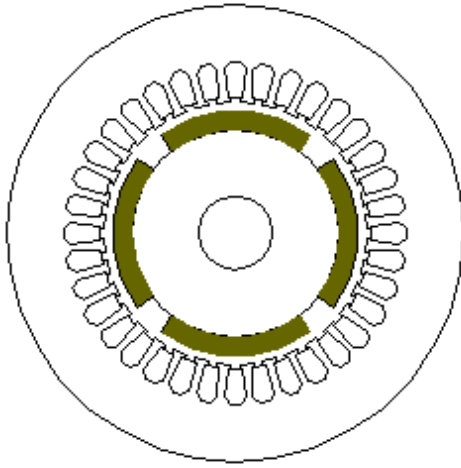
NdFeB are well suited for high performance and variable speed drives because of their high peak torque capability and their linear relationship between torque and stator current. Some potential limitations of NdFeB material in comparison with other high energy magnets are its relatively low temperature limit and vulnerability to corrosion [5].

1.4 Structure of PMSMs

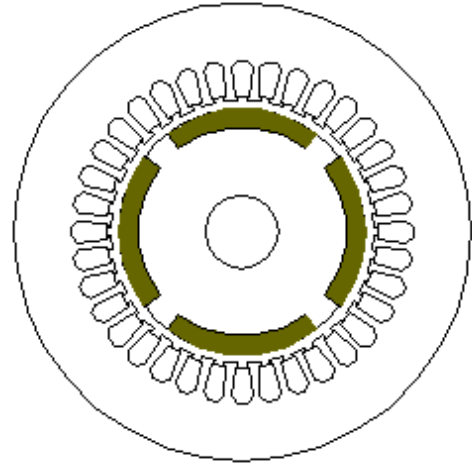
The stator of a PMSM is essentially of the same structure as that of an induction motor or a synchronous motor. Three phase stator windings produce an approximately sinusoidal distribution of rotating MMF in the air gap. There are many rotor configurations for PMSMs. Depending on the location of the magnets on the rotor, typical PMSMs can be divided into two kinds: Exterior Permanent Magnet (EPM) motors which have the permanent magnets directly facing to the air gap and stator armature winding, Fig. 1.3, and Interior Permanent Magnet (IPM) motors in which the permanent magnets are hidden inside the rotor, Fig. 1.4.

The surface-mounted PMSM (Fig. 1.3 a) in EPM motors can have magnets magnetized radially. An external high conductivity non-ferromagnetic cylinder can be used to protect the magnets against the demagnetizing action of armature reaction and centrifugal forces and provides an asynchronous starting torque, and also acts as a damper [6].

In the inset-type motors (Fig. 1.3 b) permanent magnets are magnetized

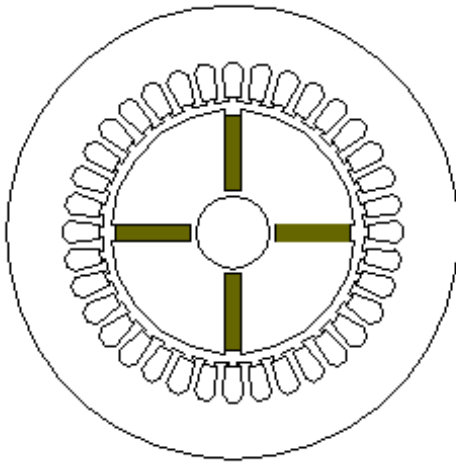


(a) Surface Mounted

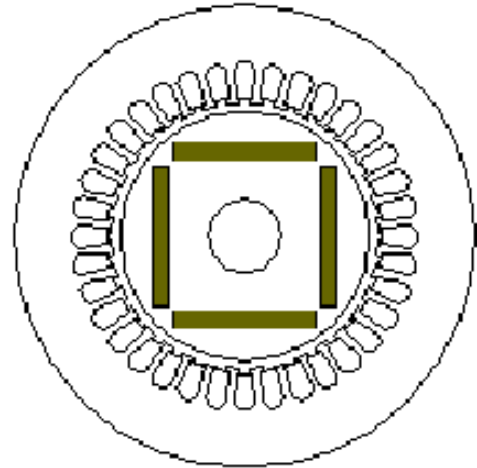


(b) Inset

Figure 1.3: Structures for exterior permanent magnet motors



(a) Spoked



(b) Buried

Figure 1.4: Structures for interior permanent magnet motors

radially and embedded in shallow slots. The rotor magnetic circuit can be laminated or made of solid steel. With the existence of permanent magnets, the d-axis synchronous reactance is lower than that in the q-axis. Because of the leakage flux in rotor, the back EMF induced by the permanent magnets is lower than that in surface-mounted PM rotors.

The spoked-magnet rotor in IPM motors has circumferentially magnetized magnets embedded in deep slots (Fig. 1.4 a). The application of a non-ferromagnetic shaft is essential.

The buried-magnet rotor in IPM motors has alternately poled magnets (Fig. 1.4 b). Since the magnet pole area is smaller than that at the rotor surface, the air gap flux density on open circuit is less than the flux density in the magnet. The synchronous reactance in d -axis is smaller than that in q -axis since the q -axis armature flux can pass through the steel pole pieces without crossing the PMs. The magnets are very well protected against centrifugal forces [7].

A brief comparison between exterior and interior magnet synchronous motors is given in Table 1.1.

Table 1.1: Comparison between PMSMs with exterior and interior magnets

Exterior PMSMs	Interior PMSMs
Simple motor construction	Relatively complicated motor construction
Air gap magnetic flux density is smaller than B_r	Air gap magnetic flux density can be greater than B_r
Small armature reaction flux	Higher armature reaction flux
PMs not protected against armature field	PMs protected against armature field
Low PM flux leakage	Higher PM flux leakage
Poor flux-weakening capability	Large flux-weakening capability
Medium speed range	Wide speed range

1.5 Literature Review

1.5.1 Constant Power Operation of PMSM Drives

Most drives for electric automobiles, trains, buses and off-road vehicles are designed to provide a constant drive torque up to a base speed and then to provide torque which is inversely proportional to speed up to a maximum speed as shown in Fig. 1.5 [8]. This constant power range of operation is determined by the limitation of energy supply system and motor properties [9].

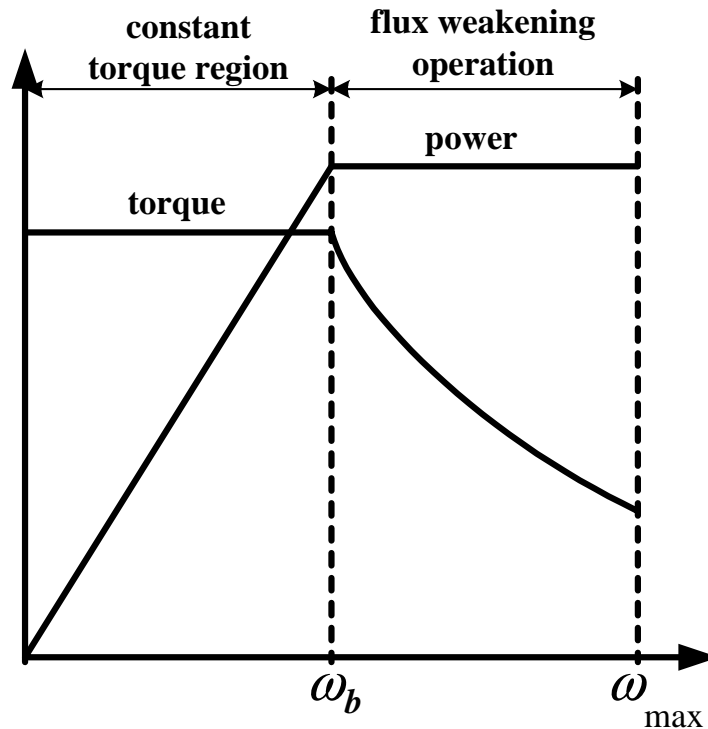


Figure 1.5: Ideal Torque vs. speed characteristics for variable speed AC drives

Commutator type DC motors have long been used for traction drives. Normally, full field current is used up to the base speed. Then, holding the armature current constant, the field is weakened in inverse proportion to speed to provide

the constant power range [10]. For a variable speed AC drive fed from a voltage source and PWM controlled inverter, a constant torque region occurs from zero to base speed ω_b as shown in Fig 1.5. The rated voltage limit is reached at base speed. In the subsequent region, the motor voltage has to be maintained at this rated voltage, hence the maximum torque capability of this drive decreases. Since the back EMF is proportional to speed, flux weakening needs to be carried out if the back EMF has to be maintained constant [11].

In recent years, there has been considerable interest in employing PMSMs for traction applications. Since most PMSMs tend to have essentially constant magnetic flux because of the properties of PM materials, the direct control of magnet flux is not possible. The air-gap flux, however, can be weakened by applying a large demagnetizing current in the d-axis of the permanent magnets [13, 12].

In Schiferl's work [14], the limiting torque-speed envelope that can be achieved with a given PMSM and a source voltage under optimum flux-weakening conditions is determined by the machine parameters. More specifically, the interrelationships between magnet flux λ_m and the machine inductance values and saliency ratio (L_q/L_d) are critical to determining the high-speed torque production capabilities. Achieving constant power operation may require machine design tradeoffs. A number of PM motor structures have been proposed to improve the flux-weakening capability and to extend the constant power speed range by Miller, Soong and Bianchi[15, 16, 17, 18].

1.5.2 The Design of PMSMs

Considerable work has been done in the past on the design of PMSMs with different rotor configurations. For exterior PMSMs, some basic design models for torque capability, loss calculation, thermal properties and magnet protection have been set up by Slemon [19, 20]. A detail design example of surface-mounted PMSM is given by Panigrahi [21]. The design procedure proposed in these papers developed approximate relations for determining the major motor dimensions to meet a design specification. These relations are useful in obtaining an estimation of what can be achieved before detailed motor design is carried out. However, most of the design relations are expressed in the form which are independent of the characteristics of the inverter supply to the motor. These PM motors are capable of very high torque and acceleration, particularly in the normal speed range, but they are not suitable for high speed operation because of poor magnet protection and flux-weakening capability.

In contrast, interior PMSMs with rotor saliency ($L_q/L_d > 1$) can offer appealing performance characteristics, providing flexibility for adopting a variety of rotor geometries including spoked or buried magnets as alternatives to exterior PMSMs [22]. Burying the magnets inside the rotor provides the basis for mechanically robust rotor construction capable of high speeds since the magnets are physically contained and protected inside rotor. In electromagnetic terms the introduction of steel pole pieces fundamentally alters the machine magnetic circuits changing the motor's torque production characteristics. The rotor saliency can be employed

to reduce the PM excitation flux requirements in the interior PMSMs in order to achieve extended-speed operating ranges [23, 24].

For conventional design of interior PMSMs (Fig. 1.4 b), the ratio of rotor saliency is as high as 2 to 3 [11]. The required motor parameters can be achieved through a number of unconventional rotor configurations [16, 17, 18, 25]. It is proven that a very high saliency ratio and a low PM excitation flux can be achieved by sandwiching flexible sheets of magnets between axial laminations as shown in Fig. 1.6 [16]. An advantage of this construction resides in its low PM flux and large constant power speed range.

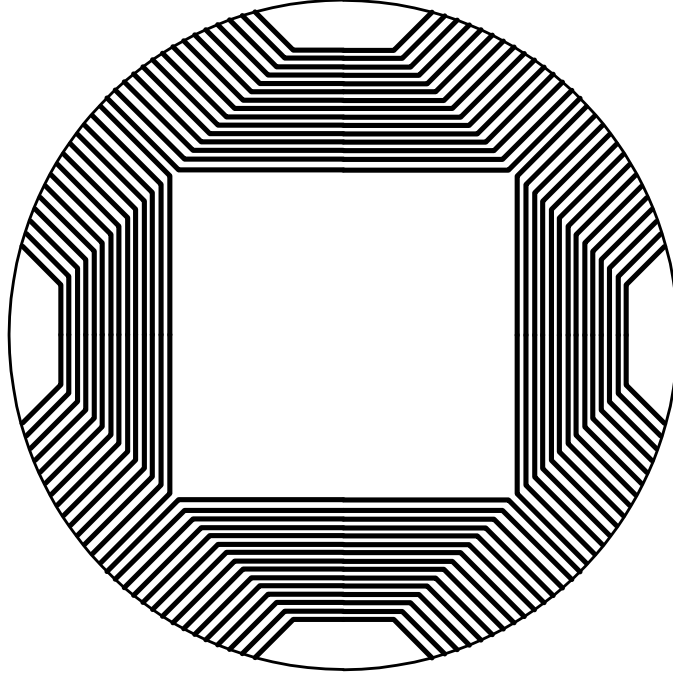


Figure 1.6: Cross section of axially laminated rotor for interior PMSM [16]

Previous design studies have considered only saliency ratios greater than unity. Nevertheless, constructions with $L_q/L_d < 1$ are possible either by employing single or multiple q -axis flux barriers [17] (Fig. 1.7) or by using a rotor

with two axial parts: one non-salient (exterior PMSM) and the other of the synchronous reluctance type [18] (Fig. 1.8). It is shown that this kind of motor allows a lower value of rated current and exhibits a larger speed range for flux-weakening operation. However, both the rotors with low and high saliency ratios have the specific disadvantages that the mechanical structure limits the maximum speed and requires unconventional manufacturing technology.

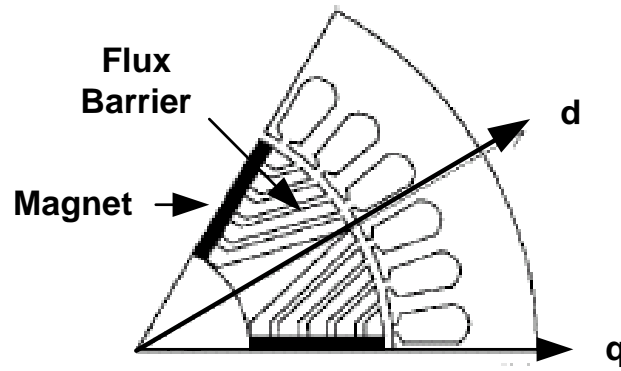


Figure 1.7: Cross section of rotor with $L_q/L_d < 1$ for interior PMSM [17]

1.5.3 Numerical Optimization

The design objective of an interior PMSM is to achieve constant power operation over an extended speed range by appropriate selection of design variables. Optimization methods can be used to find the optimal solution under constraints on the design variables.

In the optimization of electromagnetic devices the objective function can be computed using either the classical (equivalent circuit) approach or a numeri-

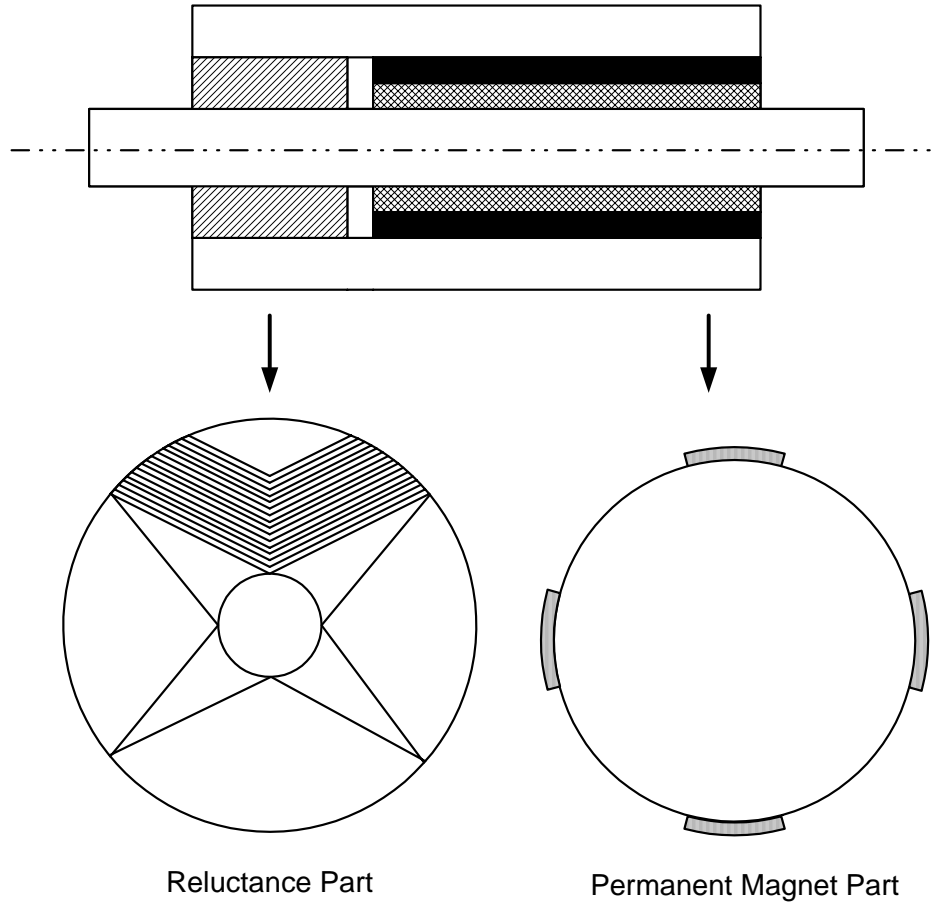


Figure 1.8: Two-part rotor with $L_q/L_d < 1$ for interior PMSM [18]

cal field computation approach, such as finite element method (FEM). The FEM is more accurate than the classical approach but it requires substantially more sophisticated software and computational time. In numerical field computations the standard prerequisites of local optimization, such as convexity, differentiability and accuracy of the objective function, are usually not guaranteed [28]. Deterministic optimization tools for solving local optimization, such as steepest-descent, conjugate gradient and quasi-Newton methods, are not ideally suited to numeric electromagnetic problems [29]. Recently, stochastic methods of optimization have become more popular due to their simplicity and high probability of finding global

minima and their simplicity [30]. Stochastic methods such as genetic algorithms (GA) [31, 32], simulated annealing [33] and evolution strategies [34] have been successfully used for different aspects of electrical machine design.

Optimization techniques have been applied to the design work of PMSMs in order to meet particular performance requirements. An optimization method for exterior PMSMs design has been presented by Higuchi [35]. The procedure integrates analytical method and finite element method (FEM) to refine the design specifications. In reference [36], a PMSM is optimized with respect to maximum power output and minimum magnet volume. The problem is treated as a vector optimization problem and is solved directly without any scalar transformation by a stochastic search algorithm. A new approach to the design optimization of exterior PMSMs is presented in [32]. The novelty lies in combining a motor analysis procedure with GA to optimize an objective function such as the motor torque, the efficiency, the material cost or other motor figures or a combination of these. It has been observed that the GA generally requires a higher number of iterations with respect to other conventional techniques. However, the GA method of optimization is able to find the global optimum avoiding the local ones. In Lahteenmaki's work [37], GA method is chosen to optimize the high-speed PMSM motors with the modelling of FEM and thermal network analysis. The main drawback with the present optimization method is that the FEM has to be applied to the numeric field computation at each stage of the optimization, which requires a lengthy computation time.

In order to overcome the problem of time-consuming computation with GA method, response surface methodology (RSM) was introduced to the numerical optimization of exterior PMSMs. The response surface methodology (RSM) is a collection of mathematical and statistical techniques that are useful for evaluating response, i.e., the objective physical quantities (motor parameters), which are influenced by several design variables [38, 39]. By careful design of the FEM experiments, RSM can be used to build the empirical model that is finally employed as an objective function or constraints in an optimization process. As the response surface is often described by polynomial representations (determinative equations), we can save computational time for optimization process by evaluating the objective physical quantities by the response surface instead of by the FEM analysis [38, 39]. RSM has been successfully applied to the design optimization of electromagnetic devices [40, 41, 42, 43].

Although numerical optimization is currently considered indispensable for PMSMs design, it is, however, difficult to design the interior PMSMs because of the complicated rotor configurations and the complex influence of magnetic saturation [44]. Till now, there is not much work that has been done on the optimization of rotor geometric parameters for interior PMSMs which require a wide constant power speed range.

1.5.4 The Control of PMSMs

Control techniques are critical to exploit the power capability of PMSMs over the entire speed range. The torque is usually controlled by controlling the phase current based on the fact that the electromagnetic torque is proportional to the motor current [45]. The current control is normally executed in the rotor oriented system, where the d-axis is along the permanent magnet. A rotor position sensor is required to achieve high-performance current control with the PMSMs. The rotor position feedback is needed to continuously perform the self-synchronization function, which is significantly more demanding than other AC machines [47]. Hence, an absolute or incremental encoder providing high resolution is typically required with PMSMs.

High-quality current vector control was first proposed by Jahns [7] and Rahman [49] for achieving high-performance motion control with PMSMs. By mapping the torque command into values for the d-q axis current component commands, then controlling the d-q axis current to follow the commands using field-oriented current controller, we can obtain the maximum torque for a given motor phase current, which is generally named as maximum-torque-per-amp (MTPA) control. By using MTPA control we can ensure maximizing operating efficiency [7]. In order to apply the MTPA control in PMSM drives, the d-axis and q-axis current commands have to be accurately calculated based on the motor parameters [49]. Separate current trajectories are identified for the exterior and interior PMSMs [50, 51, 52]. However, these methods are extremely sensitive to the accuracy of the motor parameters used in the controllers [53, 55]. Mademlis investigated the

influence of L_q variation on maximum torque to current controlled interior PMSM drives and it is shown, for a given load torque, that the stator current requirement of a saturated motor is around 15 percent higher [56]. Therefore, the respective efficiency is lower compared to an unsaturated motor. Bodson proposed modified maximum torque to current control that takes into account magnetic saturation, however the air-gap flux linkage variation effect is not considered [59]. Zhu described an enhanced online optimal control strategy which enables the maximum power capability of an interior PMSM to be achieved independent of any variation in its parameters [61], but the control performance was degraded at fast dynamic conditions.

The problem of flux-weakening using current control was first highlighted by Jahns. He proposed a corrective method of control to the standard vector control architecture [13]. A feedback of current controller error in the synchronous coordinates was regulated to zero through a PI-controller by reducing the d-axis current I_d and subsequently obtaining the q-axis current I_q . Another method presented by Sul using a PI control of the voltage error between the saturated voltage and the output voltage command of PI current controller to adjust d -axis current command [52, 64]. On the other hand, the scheme presented by Morimoto looks at voltage reference to determine the control modes between constant torque and flux-weakening [51]. These templates are generated from motor's steady state characteristics, while the dynamic characteristics are either taken into account merely by the constant voltage margin or they are implicitly solved by the current

controller. These schemes based on the static approach have at least two more drawbacks: deviations from the prescribed control trajectories occur during the transients, whereas in the steady state the available voltage of the voltage source inverter is not completely exploited [67, 68].

In order to overcome these problems, direct torque control (DTC) has been applied to PMSMs in the last decade [69, 70, 71]. DTC was first used in induction motor drives [72, 73]. The basic principle of DTC is to directly select stator voltage vectors according to the differences between the reference and actual torque and stator flux linkage. Unlike current control, DTC does not require any current regulator, coordinate transformation or PWM signal generator. In spite of its simplicity, DTC allows a fast torque response in steady-state and transient operating condition to be obtained. In addition, this controller is less influenced by the parameter detuning in comparison with current control [74]. Although DTC has many advantages over current control, it still has some disadvantages, such as high current ripples, variable switching frequency and difficulty in controlling torque and flux at very low speed.

In recent years, many researchers have tried to reduce the torque ripple and fix the switching frequency of the DTC scheme. With multi-level inverter proposed by Vas and Martins, there will be more voltage space vectors available to control the flux and torque. Therefore, a smoother torque can be expected [75, 76]. However, more power switches are needed to achieve a lower ripple and almost fixed switching frequency. Modified DTC schemes with constant switching frequency and

low torque ripple were reported by others [77, 78, 79], where space vector modulation (SVM) is incorporated with DTC for induction motor drives to provide a constant inverter switching frequency, and the torque ripple is significantly reduced for invoking zero inverter switching state within every switching period of inverter control. However, they are either motor parameter dependent or quite complicated with two PI controllers which need to be tuned properly [80, 81]. There are still drawbacks in present speed and torque control schemes that require corrections:

- DTC scheme does not include direct current control. The current protection is realized by precalculated torque profile, which is motor parameter dependent. The motor current may exceed the current constraints in the fast dynamics or flux-weakening speed range due to variation of motor parameters;
- The transition between constant torque control and flux-weakening control is determined by motor speed and constant inverter voltage, in which the inverter voltage capability is not properly exploited;
- There is no feedback flux-weakening control.

1.6 Research Goals and Methodology

Permanent magnet synchronous motors have many advantages as mentioned in the previous sections. These features permit this machine to be operated not only in the constant torque region but also in the constant power region up to a high speed by flux-weakening. However, considering the drawbacks listed in above

literature survey for PMSM drives, it is understood that further improvements in the design and control techniques of PMSMs for constant power operation are possible. Therefore, the objectives of this research are:

- Analysis of constant power speed range for IPMSM Drives;
- Design optimization of a prototype interior PMSM;
- Control of the prototype interior PMSM in wide speed operation.

1.6.1 Analysis of Constant Power Speed Range for IPMSM Drive

An accurate mathematical modelling of PMSMs provides a foundation for the design and control of PMSMs. The accuracy of the model directly affects the outcome of the design and control. A two-phase PMSM equivalent circuit model in the rotor d-q reference frame has been widely adopted by Pillay [2], Sebastian [82] and Rahman [83] due to its relatively simple composition and reasonable accuracy. The d-q model, also known as the analytical model, can be derived directly from d- and q-axis magnetic circuits or can be obtained from the three phase model of a PMSM by using Park's transformation [84].

One objective of this research is to determine the relationship between steady state equivalent circuit parameters of interior PMSMs and their power capability over a wide speed range. In all cases it will be assumed that the motor is supplied from a variable frequency inverter with current and rotor position feedback so that

both current magnitude and phase angle of current vector can be independently controlled. The system performance will be investigated primarily by the shape of the motor power capability curve which is a plot of the maximum power attainable versus motor speed subject to current and voltage magnitude constraints. A simple equivalent circuit model, which takes account of saturation effect in q-axis inductance, will be used in order to determine the best choice of motor parameters necessary for maximum power capability over a wide speed range.

1.6.2 Design Optimization of Interior PMSM

While the design process for conventional exterior PMSMs is well developed in Slemon and Panigrahi's works [19, 21], it is hard to borrow these experiences to the design of interior PMSMs because of their complicated rotor structures and complex influence of magnetic saturation. In the modelling and computing process, FEM can be used to accurately compute the air gap flux density and rotor magnetic saliency ratio that are nonlinear functions of the machine flux level. However, applying FEM in the every stage of design and optimization process is time-consuming, and sometimes not practical.

In this work, the design procedure combines the FEM and RSM for the magnetic analysis, and genetic algorithms (GA) are used as a search method in the optimization procedure. The effects of a wide range of geometric variables on the performance of PMSM are investigated and the optimum design is selected for further studies. Using the proposed design methodology, a 400 W prototype in-

terior PMSM with the optimum constant power speed range has been designed and manufactured. Various steady state tests are conducted to verify the design optimization method. Test results are compared with those from the numerical analysis. The close agreement validates the proposed RSM model for the accurate estimation of motor parameters. The tests also provided an understanding of the performance of the prototype PMSM and laid a foundation for the control of the PMSM drive system.

1.6.3 Control of IPMSM in Wide Speed Operation

For a PMSM drive the speed is determined by the frequency of its power supply and the torque is determined by both the magnitude of the stator current and the torque angle. The PMSMs can be controlled at constant torque below the base speed and at constant power above the base speed. However, without proper control strategy, the PMSM drives cannot exploit its potential power capability even with a well designed motor.

In this research, a conventional current vector control strategy is implemented. The performances on constant torque and constant power operations are investigated, and their advantages and disadvantages are examined. A novel modified DTC scheme based on stator flux control is also proposed. The experimental results confirm that the new control strategy not only improves the torque capability in the flux-weakening range, but also extends the speed range at constant power operation.

1.7 Outline of the Thesis

The contents of the thesis are organized as follows:

In Chapter 2, a constant parameter equivalent circuit model is used to determine the power capability of interior PMSMs in variable speed drive application, which is depend on the motor parameters, such as d-q axis inductances and stator PM flux linkage. A simple relationship between the power capability and motor parameters is derived in order to obtain the theoretical foundation for optimal motor designs that extend their constant power speed range.

In Chapter 3, the effect of geometric parameters on the motor parameters of interior PMSMs has been investigated using both analytical method and finite element method. In order to achieve a computationally simple and accurate motor parameters determination in the iterative process of numerical optimization, an effective computational approach which combines magnetic field analysis and analytical equations by response surface methodology (RSM) was proposed for the prediction of motor parameters in interior PMSMs. The polynomial representation of motor parameters (L_d , L_q and λ_{pm}) by RSM are derived and their accuracy in selected geometric space of rotor structure are validated by FEM.

In Chapter 4, the numerical optimization methodology is developed for interior PMSMs. The design criteria and optimization objective in this thesis are to extend the constant power speed range. The combination of FEM and RSM is used

for an investigation into the effect of a wide range of geometric variables, and GA is applied as the search method to look for the optimum rotor geometric design.

In Chapter 5, results of various steady-state tests on the prototype interior PMSM are presented, which include no-load and load test, torque-speed characteristics, and efficiency and power factor measurements. The test results are compared with those collected from the commercial interior PMSM with same power rating. The tests also provide accurate measurement of the values for motor parameters including magnet flux linkage and d-q axis inductances of prototype PMSM and hence laid a foundation for the control of the interior PMSM drive system.

In Chapter 6, various aspects of the PMSM control system are discussed. Hardware and software considerations and operations of the control system are presented. A conventional current vector control strategies is implemented and compared. Space vector modulation based modified DTC scheme is also proposed to eliminate the drawbacks of current vector control scheme. The experimental results confirm the advantages of new control method for the constant power operation over a wide speed range.

Chapter 2

Analysis of Interior Permanent Magnet Synchronous Motors for Wide-Speed Operation

2.1 Introduction

When permanent magnets are buried inside the rotor core, the motor not only provides mechanical ruggedness but also opens a possibility of increasing its power capability over a wide speed range. This class of interior PMSMs can be considered as reluctance synchronous motors and PM motors combined together. Conventionally, a two phase equivalent circuit model (d-q axis model) has been used to analyze reluctance synchronous machines and induction machines. This same technique is now applied in the analysis of interior PMSMs in this chapter.

The steady state performance of interior PMSMs can be modelled by circuit equations with stator PM flux linkage and d- and q-axis inductances that are non-linear functions of the machine flux level. However, it is critical to note important

assumptions that have been made in this analysis.

First, the simplification of the interior PMSM's equivalent circuits will include only three parameters hence that all electrical loss components are ignored. This includes both the stator copper loss, as well as hysteresis and eddy-current losses in the machine iron. Iron losses gradually increase as the speed increases because both of these iron loss components increase with frequency. Interior PMSMs are typically designed with small iron loss at rated frequency, so ignoring these losses is not expected to affect any of the major predicted trends.

Therefore, in this chapter lossless equivalent circuit model of the interior PMSMs is used to investigate the influence of machine parameters on motor performances. The purpose of this analysis is to determine the optimal set of equivalent circuit parameters to obtain output power at high speed. Steady state maximum output power versus speed curves can be derived for interior PMSMs over the whole speed range.

2.2 Mathematical Modelling

The d- and q-coordinate based equivalent circuit model is used for the modelling of PMSMs. Fig. 2.1 illustrates a conceptual cross-sectional view of a 3-phase, 2-pole interior PMSM along with two reference frames. To show the inductance difference ($L_q > L_d$), rotor is drawn with saliency.

The electrical dynamic equation in terms of phase variables can be written

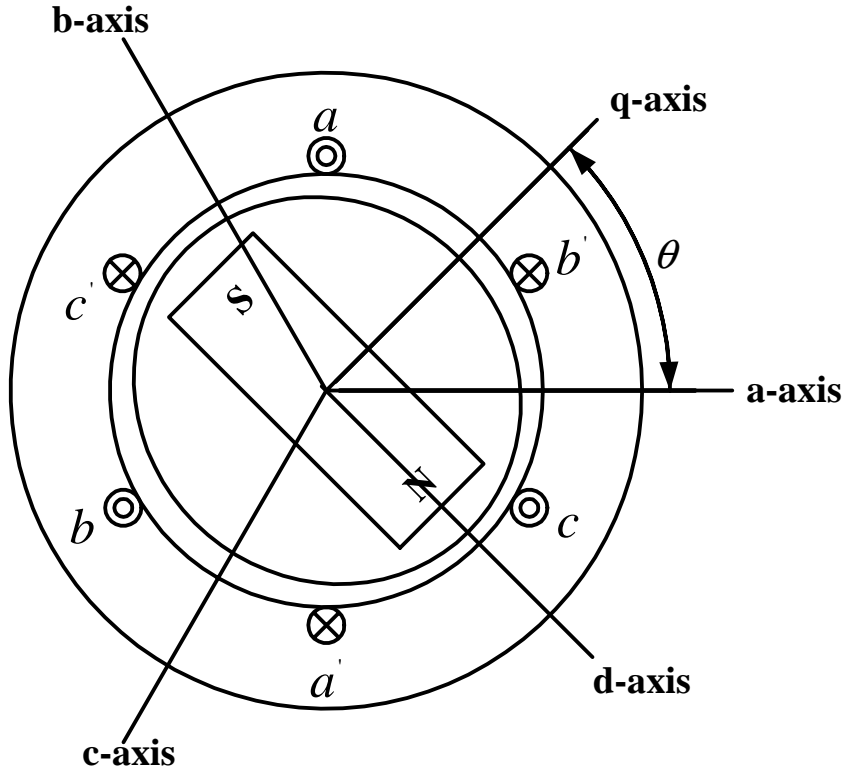


Figure 2.1: Permanent magnet synchronous motor

as:

$$V_a = R_s I_a + \frac{d\lambda_a}{dt} \quad (2.1)$$

$$V_b = R_s I_b + \frac{d\lambda_b}{dt} \quad (2.2)$$

$$V_c = R_s I_c + \frac{d\lambda_c}{dt} \quad (2.3)$$

where (V_a, V_b, V_c) , (I_a, I_b, I_c) and R_s refer to phase voltage, current and resistance, respectively. The phase flux linkage $(\lambda_a, \lambda_b, \lambda_c)$ equations are [81]:

$$\lambda_a = L_{aa} I_a + L_{ab} I_b + L_{ac} I_c + \lambda_{ma} \quad (2.4)$$

$$\lambda_b = L_{ab} I_a + L_{bb} I_b + L_{bc} I_c + \lambda_{mb} \quad (2.5)$$

$$\lambda_c = L_{ac} I_a + L_{bc} I_b + L_{cc} I_c + \lambda_{mc} \quad (2.6)$$

where $(\lambda_{ma}, \lambda_{mb}, \lambda_{mc})$ refer to the component of phase flux linkage provided by permanent magnets. In these equations, inductances are functions of the angle θ . Since stator self inductances are maximum when the rotor q-axis is aligned with the phase axis, while mutual inductances are maximum when the rotor q-axis is in the midway between two phases. Also, the effects of saliency appeared in stator self and mutual inductances are indicated by the term 2θ . Meanwhile, flux linkage at the stator windings due to the permanent magnet are:

$$\lambda_{ma} = \lambda_m \cos \theta \quad (2.7)$$

$$\lambda_{mb} = \lambda_m \cos(\theta - 2\pi/3) \quad (2.8)$$

$$\lambda_{mc} = \lambda_m \cos(\theta + 2\pi/3) \quad (2.9)$$

For this model, input power P_{in} can be represented as

$$P_{in} = \vec{V}_a \vec{I}_a + \vec{V}_b \vec{I}_b + \vec{V}_c \vec{I}_c \quad (2.10)$$

Let S represent any of the variables (current, voltage, and flux linkage) to be transformed from the $a - b - c$ frame to $d - q$ frame through the Park's transformation:

$$\begin{bmatrix} S_q \\ S_d \\ S_0 \end{bmatrix} = 2/3 \begin{bmatrix} \cos(\theta) & \cos(\theta - 2\pi/3) & \cos(\theta + 2\pi/3) \\ \sin(\theta) & \sin(\theta - 2\pi/3) & \sin(\theta + 2\pi/3) \\ 1/2 & 1/2 & 1/2 \end{bmatrix} \begin{bmatrix} S_a \\ S_b \\ S_c \end{bmatrix} \quad (2.11)$$

With these transformations the stator voltage equations in $d - q$ frame of PMSM are [84]:

$$\begin{aligned} v_d &= Ri_d + \frac{d\lambda_d}{dt} - \omega_s \lambda_q \\ v_q &= Ri_q + \frac{d\lambda_q}{dt} + \omega_s \lambda_d \end{aligned} \quad (2.12)$$

where

$$\begin{aligned}\lambda_q &= \lambda_{aq} = L_q i_q \\ \lambda_d &= \lambda_{ad} + \lambda_m = L_d i_d + \lambda_m\end{aligned}\quad (2.13)$$

λ_m is the permanent magnet flux linkage. Fig. 2.2 shows a dynamic equivalent circuit of an interior PMSM in $d-q$ frame.

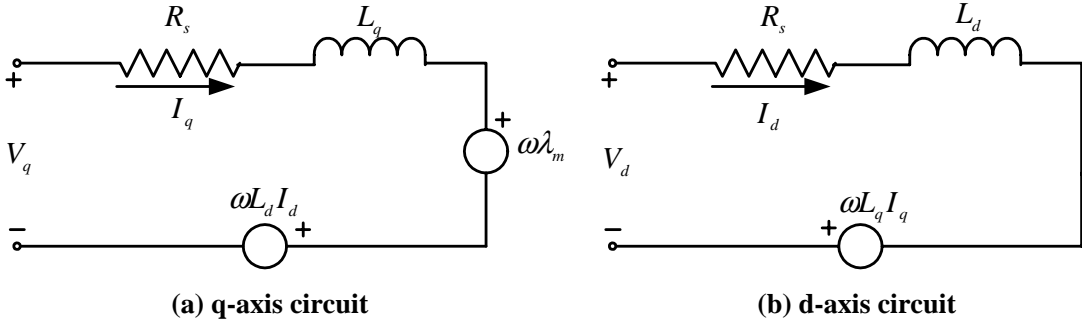


Figure 2.2: Equivalent Circuit of an interior PMSM

According to the equivalent circuit, the phasor diagram of an interior PMSM can be drawn in Fig. 2.3. For this model, input power can be derived from (2.12) via Park transformation (2.11) as:

$$\begin{aligned}P_{in} &= [V_a \ V_b \ V_c] \begin{bmatrix} I_a \\ I_b \\ I_c \end{bmatrix} = \frac{3}{2} [V_q \ V_d] \begin{bmatrix} I_q \\ I_d \end{bmatrix} \\ &= \frac{3}{2} (V_q I_q + V_d I_d)\end{aligned}\quad (2.14)$$

Neglecting the zero sequence quantities, the output power can be obtained by replacing V_q and V_d (2.12) by the associated speed excited back EMF $\omega_s \lambda_d$ and $-\omega_s \lambda_q$ as:

$$P_o = \frac{3}{2} (-\omega_s \lambda_q I_d + \omega_s \lambda_d I_q) \quad (2.15)$$

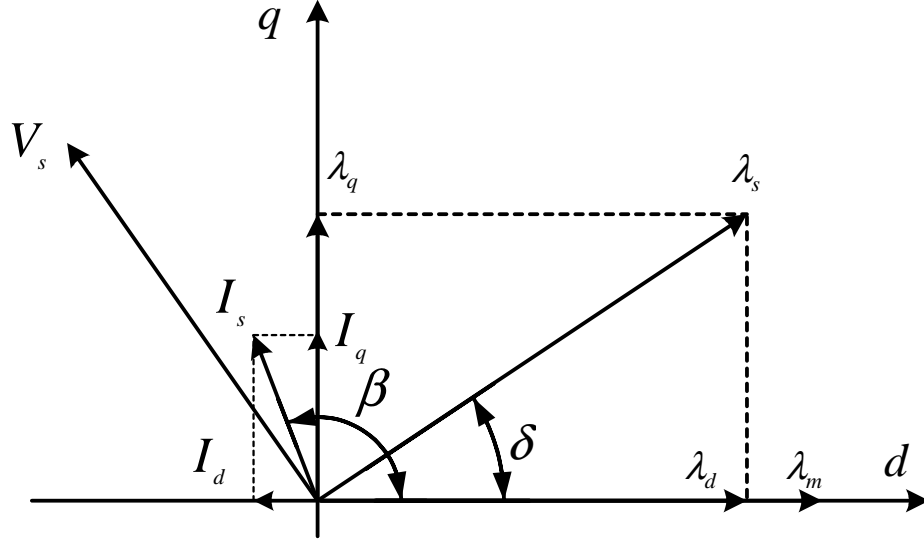


Figure 2.3: The stator flux linkage in the dq reference frame

The electromagnetic torque, which is power divided by mechanical speed can be represented as:

$$T_e = \frac{3}{2} \cdot \frac{P}{2} [\lambda_m I_q + (L_d - L_q) I_d I_q] \quad (2.16)$$

It is apparent from the above equation that the torque is composed of two distinct mechanisms. The first term corresponds to "the magnet excitation torque" or "synchronous torque" occurring between I_q and the permanent magnet, while the second term corresponds to "the reluctance torque" due to the difference in d-axis and q-axis reluctance (or inductance). Thus the torque equation suggests that the interior PMSMs can be interpreted as hybrid combination of the conventional synchronous-reluctance motors and exterior permanent magnet motors.

The equation for the motor dynamic is

$$T_e = T_l + J \frac{d\omega_r}{dt} + B\omega_r \quad (2.17)$$

where J is the inertia of the rotor and the connected load. Because we are concerned primarily with motor action, the torque T_1 is positive for a torque load. The constant B is a damping coefficient associated with the rotational system of the machine and the mechanical load.

2.3 Theoretical Analysis of Steady-State Operation

In variable speed drives, PMSMs are fed from inverters. The power rating of inverter is usually matching the power rating of motor in order to save the cost. Considering this voltage and current constraints due to power rating limitation, the armature current I_s and the terminal voltage V_s (neglecting winding resistance) are limited as follows:

$$I_s = \sqrt{I_d^2 + I_q^2} \leq I_{sm} \quad (2.18)$$

$$V_s = \omega_s \cdot \sqrt{\lambda_d^2 + \lambda_q^2} \leq V_{sm} \quad (2.19)$$

From (2.19), we have the voltage limitation related to the I_d and I_q :

$$\sqrt{(L_d I_d + \lambda_m)^2 + (L_q I_q)^2} \leq \frac{V_{sm}}{\omega_s} \quad (2.20)$$

The maximum current I_{sm} is the continuous armature current rating in steady state operation of motor. The maximum voltage V_{sm} is the maximum available output voltage from the inverter depending on the dc-link voltage. The critical condition of (2.18) and (2.31) is shown in $I_d - I_q$ plane, Fig. 2.4.

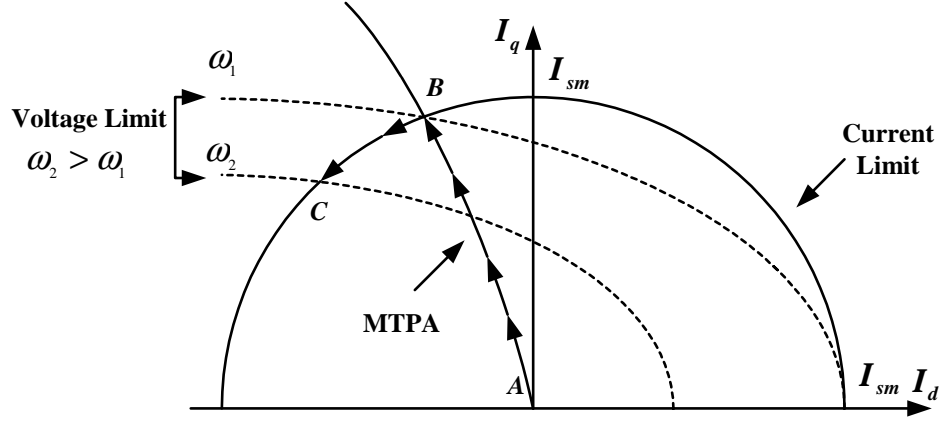


Figure 2.4: The current limit circle and voltage limit ellipse for interior PMSMs

2.3.1 Current limited maximum torque operation

In surface mounted PMSMs, because of the non-saliency ($L_d = L_q$), the maximum torque per ampere armature current (MTPA) is provided by keeping I_d equal to zero. As the interior PMSMs have a saliency ($L_d < L_q$) and, as a result, the reluctance torque is available. The armature current vector is controlled in order to produce MTPA [51]. From Fig. 2.3, we can rewrite (2.18) as:

$$\begin{aligned} I_d &= I_s \cos \beta \\ I_q &= I_s \sin \beta \end{aligned} \tag{2.21}$$

By substituting (2.21) into (2.16), we obtain:

$$T_e = \frac{3}{2} \frac{P}{2} [\lambda_m I_s \sin \beta + \frac{1}{2} (L_d - L_q) I_s^2 \cos 2\beta] \tag{2.22}$$

The relationship between the amplitude of the stator current and the current angle β can be derived by setting the derivative of (2.22) with respect to β to zero:

$$\frac{dT_e}{d\beta} = \frac{3}{2} \frac{P}{2} [\lambda_m I_s \cos \beta + (L_d - L_q) I_s^2 \cos 2\beta] = 0 \quad (2.23)$$

By substituting (2.21) into (2.23), we obtain

$$(L_d - L_q) I_d^2 + \lambda_m I_d - (L_d - L_q) I_q^2 = 0 \quad (2.24)$$

From (2.24), we can get

$$I_d = \frac{\lambda_m}{2(L_q - L_d)} - \sqrt{\frac{\lambda_m^2}{4(L_q - L_d)^2} + I_q^2} \quad (2.25)$$

This relationship is shown as the MTPA trajectory in Fig.2.4. The peak torque T_m is produced when $I_s = \sqrt{I_d^2 + I_q^2} = I_{sm}$ considering the continuous current rating. The current vector (I_d, I_q) producing this peak torque T_m is the intersection point of the MTPA trajectory and the current-limit circle, which corresponds to point B in Fig. 2.4. The d- and q-axis currents I_{dm} and I_{qm} are derived from (2.25) and $\sqrt{I_d^2 + I_q^2} = I_{sm}$:

$$\begin{aligned} I_{dm} &= \frac{\lambda_m}{4(L_q - L_d)} - \sqrt{\frac{\lambda_m^2}{16(L_q - L_d)^2} + \frac{I_{sm}^2}{2}} \\ I_{qm} &= \sqrt{I_{sm}^2 - I_{dm}^2} \end{aligned} \quad (2.26)$$

Thus, the current angle β for this peak torque is obtained as:

$$\beta_b = \arctan\left(\frac{I_{qm}}{I_{dm}}\right) \quad (2.27)$$

Therefore, the peak torque T_m can be written as:

$$T_m = \frac{3}{2} \cdot \frac{P}{2} [\lambda_m I_{qm} + (L_d - L_q) I_{dm} I_{qm}] \quad (2.28)$$

Until the terminal voltage V_s reaches its limited value V_{sm} at $\omega_s = \omega_b$, which is defined as the base speed, the motor can be accelerated by this peak torque T_m .

The highest speed (base speed) under this constant torque is given by:

$$\omega_b = \frac{V_{sm}}{\sqrt{(L_d I_{dm} + \lambda_m)^2 + (L_q I_{qm})^2}} \quad (2.29)$$

2.3.2 Current and voltage limited maximum power operation

Inverter fed PMSM drives exhibit a constant torque region, from zero to the base speed with increasing voltage. Then a decreasing torque region follows with a constant voltage which extends up to the maximum operational speed. The high-speed constant voltage operation is accomplished by reducing the stator flux linkage through an appropriate stator current distribution and thus it is generally called “flux-weakening region”.

The critical condition of (2.18) and (2.19) under flux-weakening operation is given by the voltage-limit ellipse in the $I_d - I_q$ plane as shown in Fig. 2.4 by the dashed lines. The voltage-limit ellipse becomes smaller as the speed increases and, as a result, the current vector producing peak torque T_m cannot satisfy the voltage constraint above the base speed. The d- and q-axis components of the armature current are controlled in order to keep V_s equal to V_{sm} in the flux-weakening region as shown in (2.30):

$$\sqrt{\lambda_d^2 + \lambda_q^2} = \sqrt{(L_d I_d + \lambda_m)^2 + (L_q I_q)^2} = \frac{V_{sm}}{\omega_s} \quad (2.30)$$

Substitute (2.13) into (2.30), we get the relationship between I_d and I_q for voltage constraint:

$$I_d = -\frac{\lambda_m}{L_d} + \frac{1}{L_d} \sqrt{\left(\frac{V_{sm}}{\omega_s}\right)^2 - (L_q I_q)^2} \quad (2.31)$$

Substituting (2.18) into (2.31), we can get the equation for I_d with respect to motor speed ω_s for current and voltage limited maximum power operation (above the base speed):

$$(L_d^2 - L_q^2)I_d^2 + 2L_d\lambda_m I_d + \lambda_m^2 + L_q^2 I_{sm}^2 - \left(\frac{V_{sm}}{\omega_s}\right)^2 = 0 \quad (2.32)$$

Assuming

$$\begin{aligned} a &= L_d^2 - L_q^2 \\ b &= 2L_d\lambda_m \\ c &= \lambda_m^2 + L_q^2 I_{sm}^2 - \left(\frac{V_{sm}}{\omega_s}\right)^2 \end{aligned} \quad (2.33)$$

then (2.32) can be rewritten as:

$$aI_d^2 + bI_d + c = 0 \quad (2.34)$$

Therefore, the solution for (2.34) is

$$\begin{aligned} I_{dn} &= \frac{-b + \sqrt{b^2 - 4ac}}{2a} \\ &= \frac{-2L_d\lambda_m + \sqrt{(2L_d\lambda_m)^2 - 4(L_d^2 - L_q^2)(\lambda_m^2 + L_q^2 I_{sm}^2 - (\frac{V_{sm}}{\omega_s})^2)}}{2(L_d^2 - L_q^2)} \end{aligned} \quad (2.35)$$

Finally, I_q can be solved as:

$$I_{qn} = \sqrt{I_{sm}^2 - I_{dn}^2} \quad (2.36)$$

Substitute (2.35) and (2.36) into (2.16), we can get the maximum torque with respect to motor speed ω_s under current and voltage constraints, which is shown

is (2.37).

$$\begin{aligned} T_n &= \frac{3}{2} \cdot \frac{P}{2} [\lambda_m I_{qn} + (L_d - L_q) I_{dn} I_{qn}] \\ &= \frac{3}{2} \cdot \frac{P}{2} \left[\lambda_m + \frac{-2L_d \lambda_m + \sqrt{(2L_d \lambda_m)^2 - 4(L_d^2 - L_q^2)(\lambda_m^2 + L_q^2 I_{sm}^2 - (\frac{V_{sm}}{\omega_s})^2)}}{2(L_d + L_q)} \right] I_{qn} \end{aligned} \quad (2.37)$$

and motor speed ω_s satisfies the following voltage equation:

$$\omega_s = \frac{V_{sm}}{\sqrt{(L_d I_{dn} + \lambda_m)^2 + (L_q I_{qn})^2}} \quad (2.38)$$

2.3.3 Voltage limited maximum power operation

From (2.22), (2.18) and (2.19), the armature current vector (I_d, I_q) producing maximum output torque under the voltage-limit condition is derived as follows where the current-limit condition is not considered.

The voltage equation for interior PMSMs above the base speed is derived as:

$$(\lambda_m + L_d I_d)^2 + (L_q I_q)^2 = \left(\frac{V_{sm}}{\omega_s} \right)^2 \quad (2.39)$$

and the torque equation is:

$$T_e = \frac{3}{2} \cdot \frac{P}{2} [\lambda_m I_q + (L_d - L_q) I_d I_q] \quad (2.40)$$

Rewriting (2.39) as:

$$\begin{aligned} \lambda_m + L_d I_d &= \frac{V_{sm}}{\omega_s} \cos \alpha \\ L_q I_q &= \frac{V_{sm}}{\omega_s} \sin \alpha \end{aligned} \quad (2.41)$$

Subsequently, we get:

$$\begin{aligned} I_d &= \frac{V_{sm}}{\omega_s L_d} \cos \alpha - \frac{\lambda_m}{L_d} \\ I_q &= \frac{V_{sm}}{\omega_s L_q} \sin \alpha \end{aligned} \quad (2.42)$$

where α is an interim variable. Thus, with

$$\begin{aligned} \frac{dT_e}{d\alpha} &= \lambda_m \frac{V_{sm}}{\omega_s L_q} \cos \alpha + (L_d - L_q) \cdot \frac{V_{sm}}{\omega_s L_d} \cdot (-\sin \alpha) \cdot \frac{V_{sm}}{\omega_s L_q} \sin \alpha \\ &+ (L_d - L_q) \cdot \frac{V_{sm}}{\omega_s L_d} \cdot (\cos \alpha) \cdot \frac{V_{sm}}{\omega_s L_q} \cos \alpha = 0 \end{aligned} \quad (2.43)$$

we can get

$$2(L_d - L_q) \cdot \frac{V_{sm}}{\omega_s L_d} \cdot \frac{V_{sm}}{\omega_s L_q} \cos^2 \alpha + \frac{L_q}{L_d} \cdot \frac{\lambda_m V_{sm}}{\omega_s L_q} \cos \alpha - (L_d - L_q) \cdot \frac{V_{sm}}{\omega_s L_d} \cdot \frac{V_{sm}}{\omega_s L_q} = 0 \quad (2.44)$$

Assuming

$$\begin{aligned} A &= (L_d - L_q) \cdot \frac{V_{sm}}{\omega_s L_d} \cdot \frac{V_{sm}}{\omega_s L_q} \\ B &= \frac{L_q}{L_d} \frac{\lambda_m V_{sm}}{\omega_s L_q} \end{aligned} \quad (2.45)$$

then (2.44) can be rewritten as:

$$2A \cos^2 \alpha + B \cos \alpha - A = 0 \quad (2.46)$$

Therefore,

$$\cos \alpha = \frac{-B - \sqrt{B^2 + 8A^2}}{4A} \quad (2.47)$$

Substituting (2.45) into (2.47) with simplifications, we can obtain:

$$\cos \alpha = \frac{-\rho \lambda_m + \sqrt{(\rho \lambda_m)^2 + 8(1 - \rho)^2 (V_{sm}/\omega_s)^2}}{4(1 - \rho)(V_{sm}/\omega_s)} \quad (2.48)$$

and

$$\rho = L_q/L_d > 1 \quad (2.49)$$

By substituting (2.48) into (2.42), we can get the solution of I_d which produce maximum power under voltage limit:

$$I_{dp} = -\frac{\lambda_m}{L_d} - \frac{-\rho \lambda_m + \sqrt{(\rho \lambda_m)^2 + 8(\rho - 1)^2 (V_{sm}/\omega_s)^2}}{4(\rho - 1)L_d} \quad (2.50)$$

If we define

$$\Delta I_d = \frac{-\rho\lambda_m + \sqrt{(\rho\lambda_m)^2 + 8(\rho-1)^2(V_{sm}/\omega_s)^2}}{4(\rho-1)L_d} \quad (2.51)$$

then I_d can be rewritten as:

$$I_{dp} = -\frac{\lambda_m}{L_d} - \Delta I_d \quad (2.52)$$

and by substituting (2.52) into (2.39) we get the solution of I_q as:

$$\Delta I_d^2 + (\rho I_{qp})^2 = \left(\frac{V_{sm}}{\omega_s L_d}\right)^2 \quad (2.53)$$

Finally, I_{qp} can be rewritten as:

$$I_{qp} = \frac{\sqrt{(V_{sm}/\omega_s)^2 - (\Delta I_d L_d)^2}}{\rho L_d} \quad (2.54)$$

Substitute (2.52) and (2.54) into (2.16), we can get the maximum torque with respect to motor speed ω_s under voltage constraints:

$$T_p = \frac{3}{2} \cdot \frac{P}{2} [\lambda_m I_{qp} + (L_d - L_q) I_{dp} I_{qp}] \quad (2.55)$$

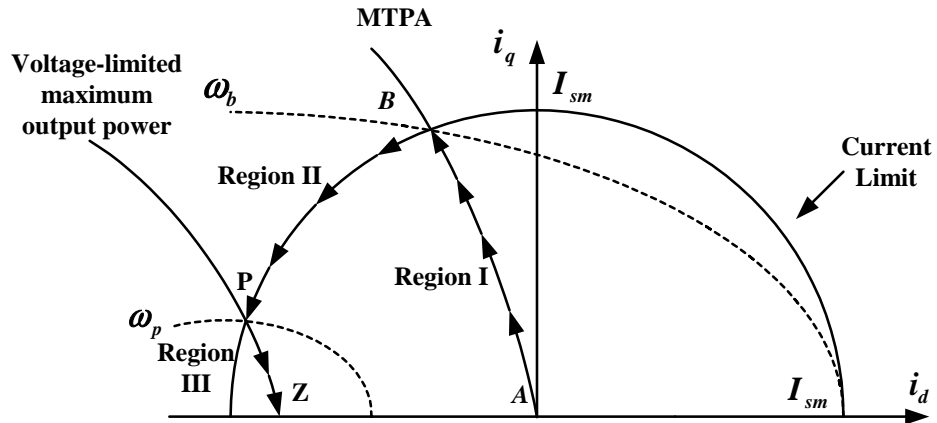


Figure 2.5: The optimum current vector trajectory in the d-q coordinate plane for $\lambda_m < L_d I_{sm}$

The current vector trajectory of the voltage-limited maximum output power is shown in Fig. 2.5. This current vector approaches the point P as the rotor speed increases and reaches the current-limit circle at $\omega_s = \omega_p$. The rotor speed ω_p is the minimum speed for the voltage-limited maximum output power operation. Below this speed, the voltage-limited maximum output power trajectory intersects the voltage-limit ellipse outside the current limit circle. The direct solution of ω_p from (2.52), (2.54) and (2.18) is difficult. Alternatively, numerical computation can be used to obtain ω_p by solving the following equations:

$$\begin{aligned} I_{dp} &= -\frac{\lambda_m}{L_d} - \frac{-\rho\lambda_m + \sqrt{(\rho\lambda_m)^2 + 8(\rho-1)^2(V_{sm}/\omega_s)^2}}{4(\rho-1)L_d} \\ I_{qp} &= \frac{\sqrt{(V_{sm}/\omega_s)^2 - (\Delta I_d L_d)^2}}{\rho L_d} \\ I_{sm} &= \sqrt{I_{dp}^2 + I_{qp}^2} \end{aligned} \quad (2.56)$$

Therefore, ω_p is derived as:

$$\omega_p = \frac{V_{sm}}{\sqrt{(L_d I_{dp} + \lambda_m)^2 + (L_q I_{qp})^2}} \quad (2.57)$$

2.3.4 Optimum current vector trajectory

To produce the maximum output power in all speed ranges considering the conditions of both the current and the voltage limits, the optimum current vector is chosen as follows:

Region I ($\omega_s \leq \omega_b$): I_d and I_q are constant values given by (2.26). The current vector is fixed at point B in Fig. 2.5.

Region II ($\omega_b < \omega_s \leq \omega_p$): I_d and I_q are chosen as the cross point of the current-limit circle and the voltage-limit ellipse. The current vector moves from point B to P along the current-limit circle as the rotor speed increases.

Region III ($\omega_s > \omega_p$): I_d and I_q are given by (2.52) and (2.54). The current vector moves from point P to Z along the voltage-limited maximum output trajectory.

Region I corresponds to $I_s = I_{sm}, V_s < V_{sm}$. Region II corresponds to $I_s = I_{sm}, V_s = V_{sm}$. Region III corresponds to $I_s < I_{sm}, V_s = V_{sm}$. If $\lambda_m > L_d I_{sm}$, which means that the permanent magnet flux is too strong to be cancelled by armature reaction with phase current, the voltage-limited maximum output power trajectory is outside the current limit circle (see Fig. 2.6). Therefore, Region III can not exist, and the output power becomes zero at $\omega_s = \omega_m$ (point M in Fig. 2.6), where all the phase current is used to demagnetize the permanent magnet flux:

$$\omega_m = \frac{V_{sm}}{\lambda_m - L_d I_{sm}} \quad (2.58)$$

With the optimum current vector trajectory in Regions I, II and III, we can obtain the maximum output torque profiles in all speed range as shown in Fig. 2.7. While Fig. 2.8 (a) shows the typical torque vs. speed curve with $\lambda_m < L_d I_{sm}$, and Fig. 2.8 (b) shows the typical torque vs. speed curve with $\lambda_m > L_d I_{sm}$. It is noted that the torque capability in flux-weakening ($\omega_s > \omega_b$) can be extended if the motor parameters satisfy the following condition:

$$\lambda_m < L_d I_{sm} \quad (2.59)$$

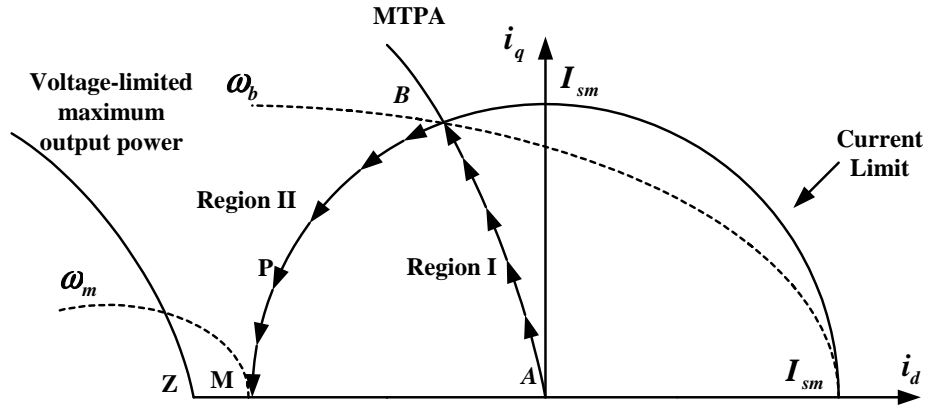


Figure 2.6: The optimum current vector trajectory in the d - q coordinate plane for $\lambda_m > L_d I_{sm}$

However, in most of design cases, we have only $\lambda_m > L_d I_{sm}$, which means the permanent magnet flux is too strong to be fully cancelled by the armature reaction of stator windings.

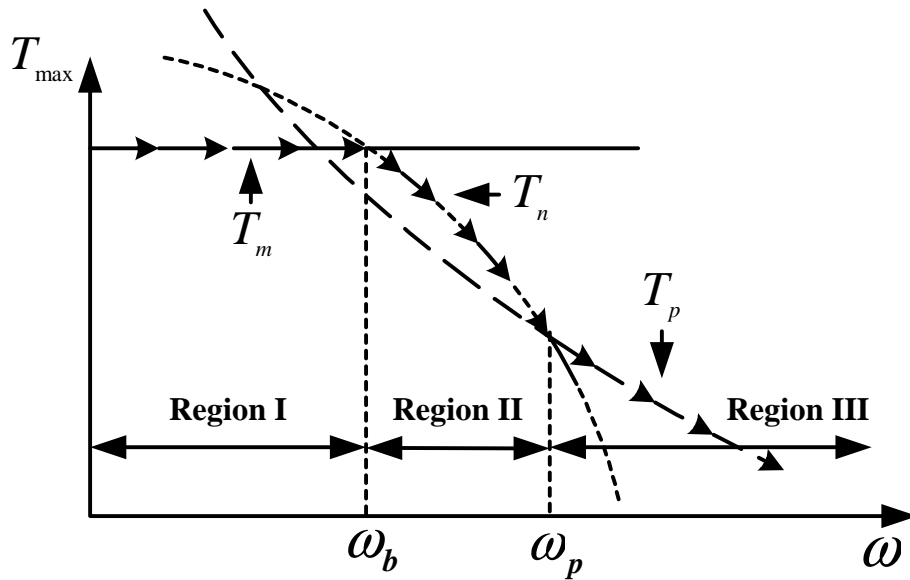


Figure 2.7: The maximum obtainable torque vs. speed profile

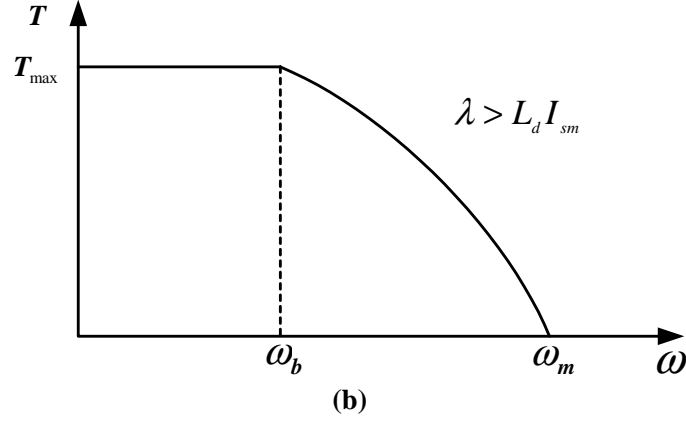
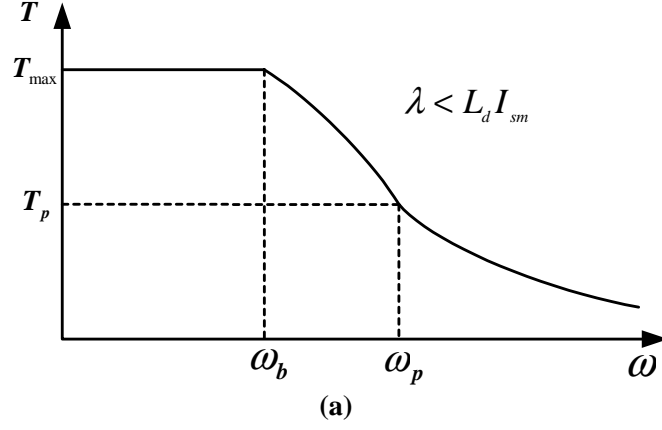


Figure 2.8: Torque vs. speed characteristics with optimum current vector trajectory

2.4 Effects of Motor Parameters on Torque-Speed Characteristics

In Fig. 2.8 (a) and (b), with the same current and voltage limits, it shows that torque vs. speed characteristics are different for $\lambda_m < L_d I_{sm}$ and $\lambda_m > L_d I_{sm}$. This fact suggests that the detail investigation needs to be conducted in order to analyze the effects of motor parameters on the performance of machine torque-speed characteristics.

With voltage and current constraints (2.18) and (2.19) we obtain the torque

vs. speed curves for a 400W interior PMSM (see Appendix A for motor specifications) with the $V_{sm} = 163V$ and $I_{sm} = 2.0A$ but with different combinations of motor parameters. Fig. 2.9 illustrates the wide-speed operation with the constant d- and q-axis inductances but different flux linkages. It suggests that the speed range is related to the magnitude of magnet flux linkage, since small magnet flux in the air gap means there is some larger flux-weakening capability. However, extending speed range is achieved at the cost of lower torque in the constant torque region.

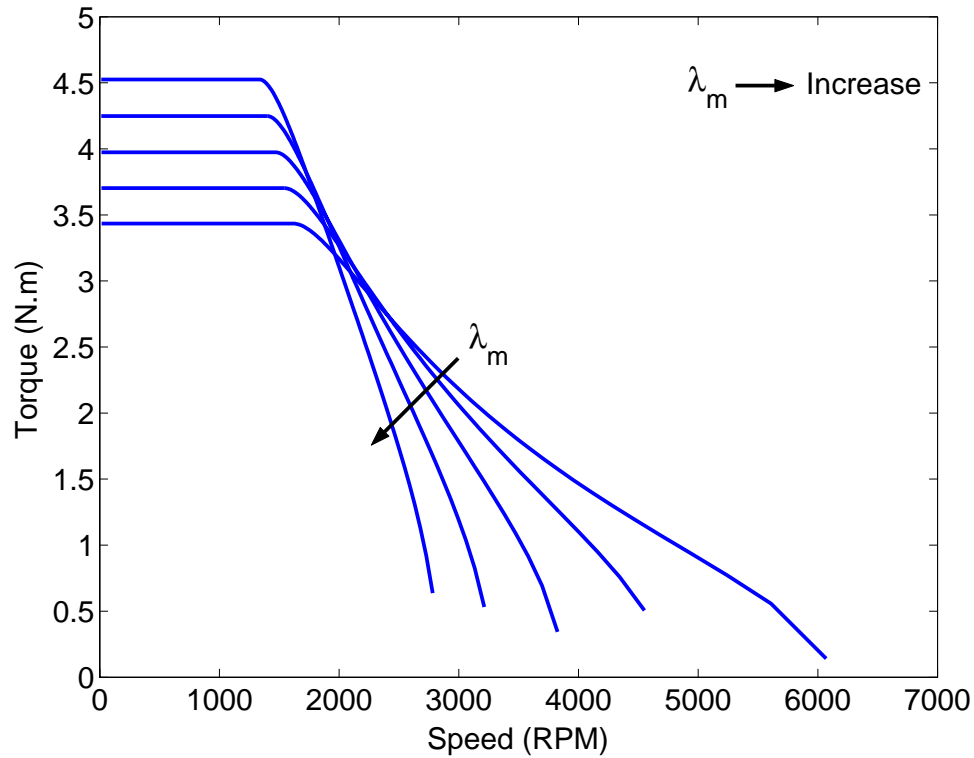


Figure 2.9: Torque-speed characteristics with different magnet flux linkages

Fig. 2.10 shows the effect of different q-axis inductance on the torque-speed characteristics. It is clear that the higher q-axis inductance only increases the torque below the base speed, but has no effect on the extending of flux-weakening

speed range.

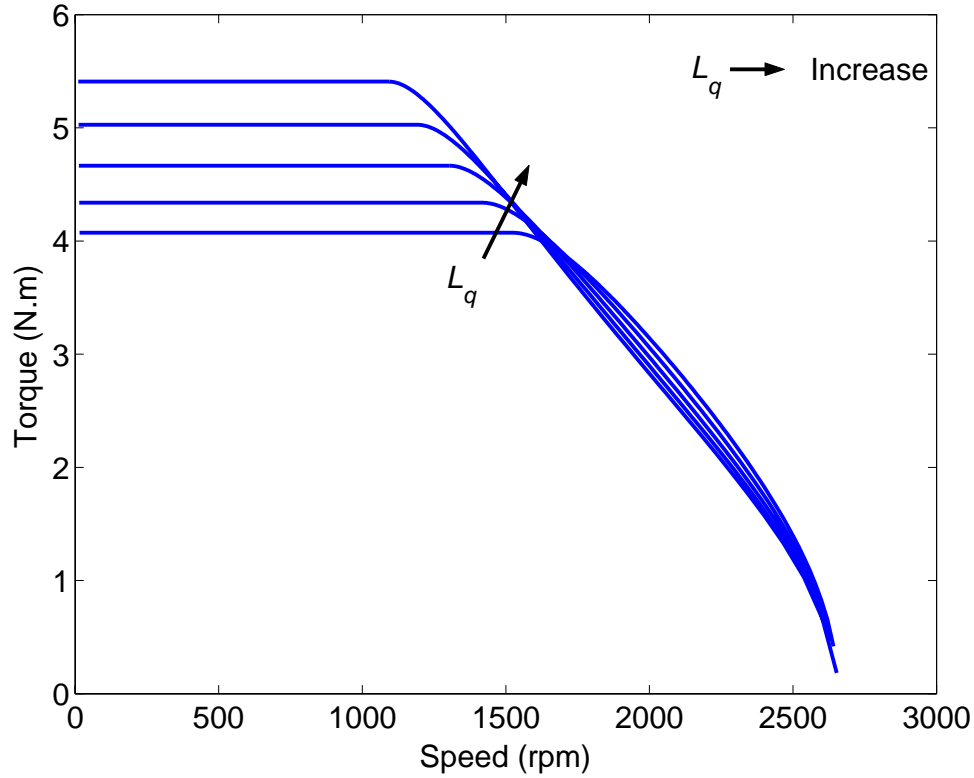


Figure 2.10: Torque-speed characteristics with different q-axis inductance

Fig. 2.11 describes the effect of different d-axis inductances on the wide-speed operation. It has the similar effect as the flux linkage on the constant torque region, but higher d-axis inductance value extends the flux weakening speed range significantly.

2.5 Design Considerations on Constant Power Speed Range

A constant power speed range (CPSR) is defined as the speed range at which the motor drive can maintain rated power with voltage and current constraints, which

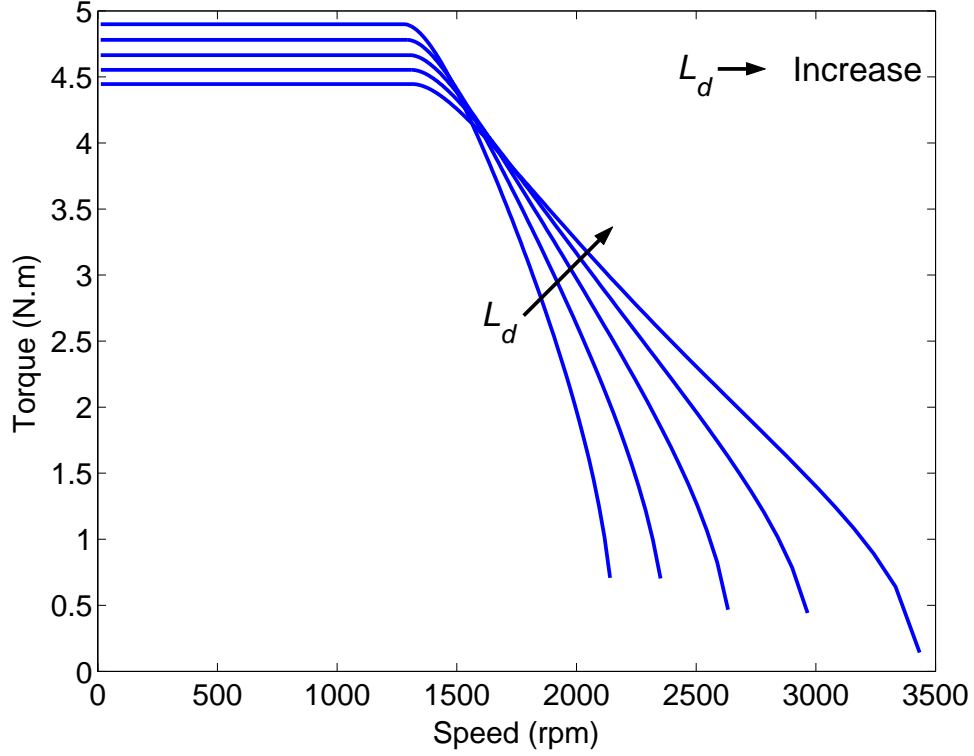


Figure 2.11: Torque-speed characteristics with different d-axis inductances

can be formulated as:

$$CPSR = \frac{\omega_{\max}}{\omega_{\text{rated}}} = f(L_d, L_q, \lambda_m) \quad (2.60)$$

where ω_{rated} is the motor rated speed and ω_{\max} is the maximum speed at which the rated power can be maintained. From these observations on torque-speed characteristics of interior PMSMs, we can conclude that if a large constant power speed range is required, the low flux linkage and high d-axis inductance are preferred. However, all motor parameters have certain suitable ranges because of the mechanical design constraints. Fig. 2.12 shows the constant power speed range for 5 different motor designs, which have the same stator frame and winding design but have different rotor structures. The CPSRs and motor parameters for 5 designs are listed in Table. 2.1.

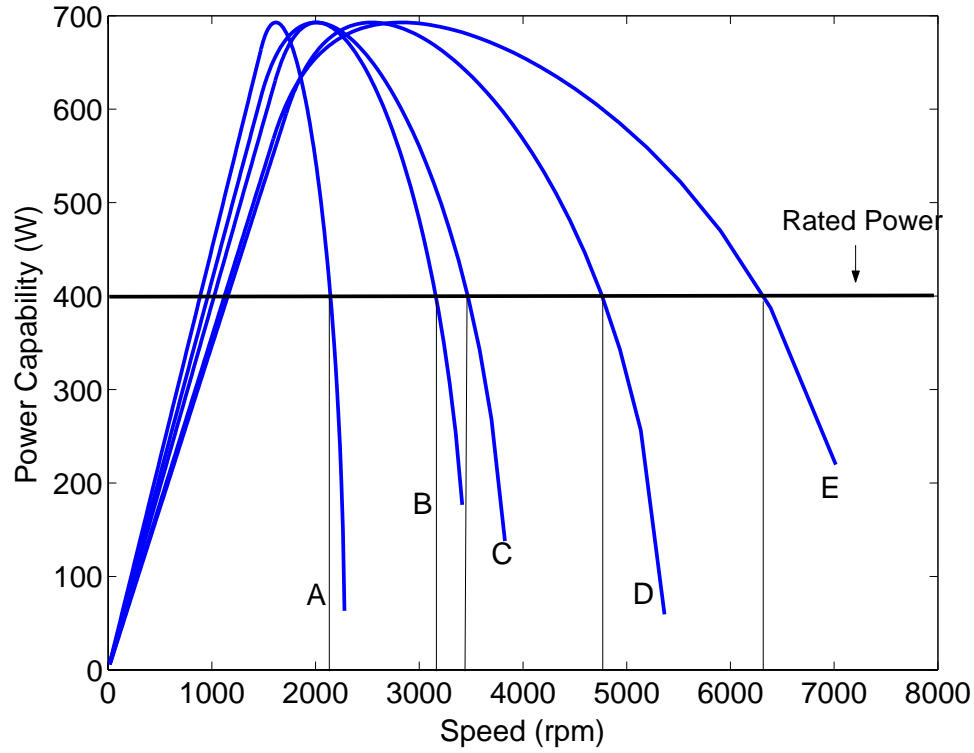


Figure 2.12: Comparison of power vs. speed characteristics for 5 designs

Table 2.1: Motor parameters for 5 Interior PMSMs

parameters	A	B	C	D	E
$L_d(H)$	0.044	0.050	0.059	0.070	0.081
$L_q(H)$	0.12	0.142	0.181	0.143	0.156
$\lambda_m(Wb)$	0.466	0.390	0.369	0.343	0.296
CPSR	1.23	1.69	1.84	2.85	3.45

2.6 Conclusions

The steady state equivalent circuit model of interior PMSMs was used in this chapter to investigate the influence of motor parameters on the power capability of permanent magnet synchronous motors driven by voltage source inverters. It was shown that the voltage constraint at the motor terminals limits the torque

output at high speed. For most designs this constraint causes the torque to drop to zero and limit the speed range. This constant power speed range can be theoretically extended if the motor is designed with optimum combination of L_d , L_q and λ_m . All of the above conclusions address the theoretical limits of operation of lossless, linear model of interior type PMSMs. The practical interior PMSMs have complicated rotor structures and complex influence of magnetic saturation. Calculation and selection of optimum motor parameters require effective computation and optimization approach which is discussed in the following chapter.

Chapter 3

Determination of Motor Parameters in Interior PMSMs

3.1 Introduction

In order to extend the constant power speed range whilst keeping an economic inverter rating for PMSM drives, the optimum combination of motor parameters (L_d , L_q and λ_m) in an interior PMSM is necessary as discussed in Chapter 2. This chapter discusses the determination of motor parameters in the machine design stage.

The parameters in equivalent circuit model of an interior PMSM with fixed stator windings are dependent on the configurations of the permanent magnets in the rotor and the geometrical profile of the air gap. The design objective is to select the appropriate geometry for the machine to obtain the optimum combination of motor parameters to achieve a larger constant power speed range. The additional design goals are high efficiency and power factor.

The motor parameters can be calculated by analytical equations derived from generalized electrical machine theory, which is computationally simple and quick, and it allows a wide range of design variables to be evaluated. However, it is difficult to use this method to calculate the performance of the machine taking into account the effect of magnetic saturation and complex rotor configurations. Numerical techniques have been recognized as practical and accurate methods of field computation to aid in the electrical design. Finite element method has emerged as a suitable technique for computation of motor parameters and performance evaluation. But design optimization based on finite element solutions is time-consuming process. In order to achieve a computationally simple and accurate prediction, an effective computational approach which combines magnetic field analysis and analytical equations by response surface methodology (RSM) is proposed for the determination of motor parameters in interior PMSMs.

3.2 Design of The Stator Winding

The motor parameters (L_d , L_q and λ_m) in an interior PMSM depend on the detail of stator winding and rotor structure. The stator of an existing 400W induction motor is used in this work, which is shown in Fig. 3.1, and the geometry of stator structure is listed in Table 3.1.

The design procedure of winding distribution for the prototype interior PMSM is similar as the induction motor. Therefore, a simplified design example of phase winding is listed as follows:

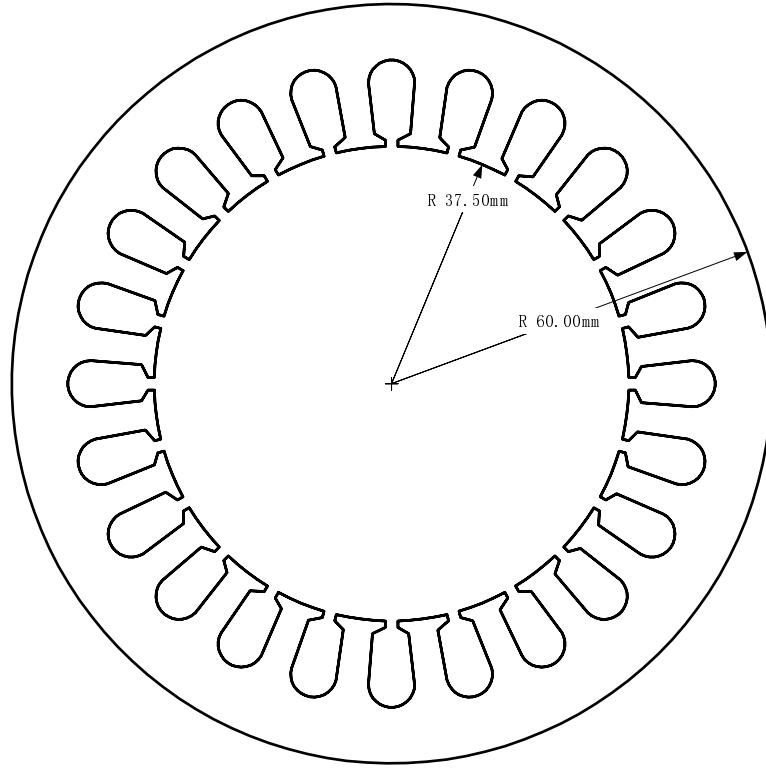


Figure 3.1: Stator frame structure

- If the required output power $P_{\text{out}} = 400 \text{ W}$, the rms value of linear current density:

$$K_{1s} = \frac{P_{\text{out}} \cdot 2p}{\pi B_{1g} D^2 L \omega_s} = 13.206 (\text{kA/m}) \quad (3.1)$$

where, $\omega_s = 2\pi f = 100\pi \text{ rad/s}$ and B_{1g} is selected as 0.4 Tesla .

- Ampere turns per phase:

$$N_{\text{ph}} I_{\text{ph}} = (K_{1s} / k_w) \pi D / 6 = 557.6 (\text{AT}) \quad (3.2)$$

where, k_w is the winding factor, N_{ph} is the stator turns per phase and I_{ph} is the phase current.

- Current density in conductor:

$$J_c = \frac{K_s}{f_s \cdot SWF \cdot SD} = 4.618 (\text{A/mm}^2) \quad (3.3)$$

Table 3.1: Stator frame data for the prototype interior PMSM

Diameter of stator bore D	75 mm
Stator length L	52 mm
Number of slots in stator S	24
Slot area S_a	67.5 mm^2
Slot depth SD	12.3 mm
Slot width factor SWF	0.5
Slot space factor f_s	0.5
Air gap length g	0.5 mm

Table 3.2: Specifications of the Interior PMSM

Rated power	400 W
Line voltage	200 V
Line current	1.9 A
Rated torque	2.55 $N.m$
Number of phases	3
Number of poles	4
Number of stator slots	24
Winding layout	double layer
Winding pitch	5/6
Base speed	1500 rpm
Residual flux density B_r	1.145 T
Coercive force H_c	881 kA/m

- Back EMF and number of turns per phase

$$E_{\text{ph}}(\text{rms}) = \epsilon \cdot V = (\pi/p) \cdot (4/\pi) \cdot (k_w N_{\text{ph}} B_{1g} DL \cdot \omega_s/2) = 72(V) \quad (3.4)$$

$$N_{\text{ph}} = \frac{2E_{\text{ph}}}{(k_w B_{1g} DL \omega_s)} = 312 \quad (3.5)$$

where, $\epsilon = 0.62$ for under excited motors.

- Revised number of turns per phase:

$$N_{\text{ph}} = \frac{6N_{\text{ph}}}{S} \cdot 4 = 312 \quad (3.6)$$

- Phase *rms* current:

$$I_{\text{ph}} = \frac{N_{\text{ph}} I_{\text{ph}}}{N_{\text{ph}}} = 1.92(A) \quad (3.7)$$

- Cross-sectional area of each conductor:

$$A_z = I_{\text{ph}}/J_c = 0.416(\text{mm}^2) \quad (3.8)$$

- Bare diameter of conductor:

$$d_c = \sqrt{4A_z/\pi} = 0.65(\text{mm}) \quad (3.9)$$

- Actual slot space factor:

$$f_s = \frac{6N_{\text{ph}}}{S} \cdot \frac{A_z}{S_a} = 0.48 \quad (3.10)$$

Stator winding details are listed in Table 3.3 and the graph for the winding distribution is shown in Fig. A.2 (Appendix A).

Table 3.3: Winding specifications for the prototype interior PMSM

Slots per phase	8
Phase spread	60° elec.
Coils per phase	8
Turns per coil	39
Turns per phase	312
Conductors per slot	78
Winding factor	0.933
Wire diameter	0.65 <i>mm</i>
Slot space factor	0.48

3.3 Selection of The Rotor Design Variables

As discussed in Chapter 1, the PMSM configuration chosen for this research have a structure with NdFeB permanent magnets, as shown in Fig. 3.2.

The stator frame of a standard induction machine has been used in interior PMSMs. The stator windings layout and ratings designed in previous section remain unchanged for different sample rotors. The design specifications of the interior PMSM stator and permanent magnet material are listed in Table. 3.2.

Once the stator geometry and winding layout are determined, the motor parameters are determined by the design variables in the rotor geometry. By FEM computation, the flux plot for one pole produced by permanent magnet is shown in Fig. 3.3 and flux density in the air gap for one pole pair is plotted in Fig.

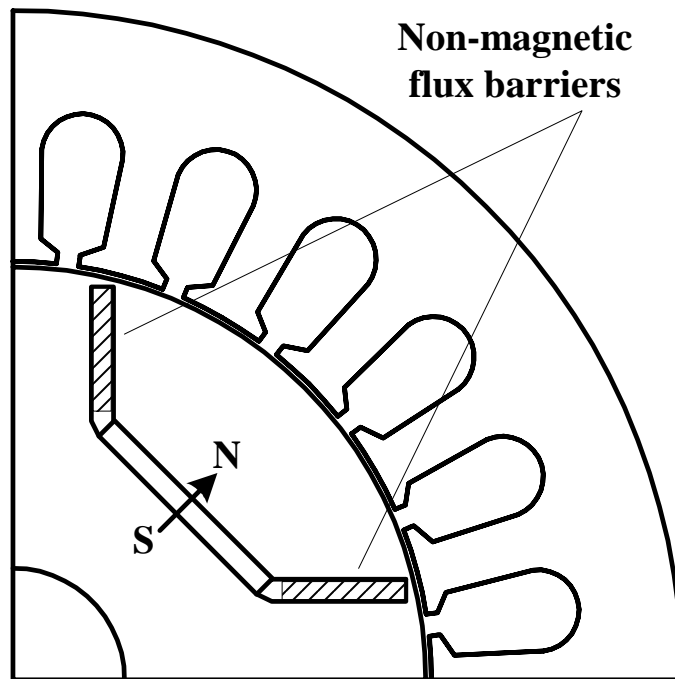


Figure 3.2: Stator and rotor structure for interior PMSMs

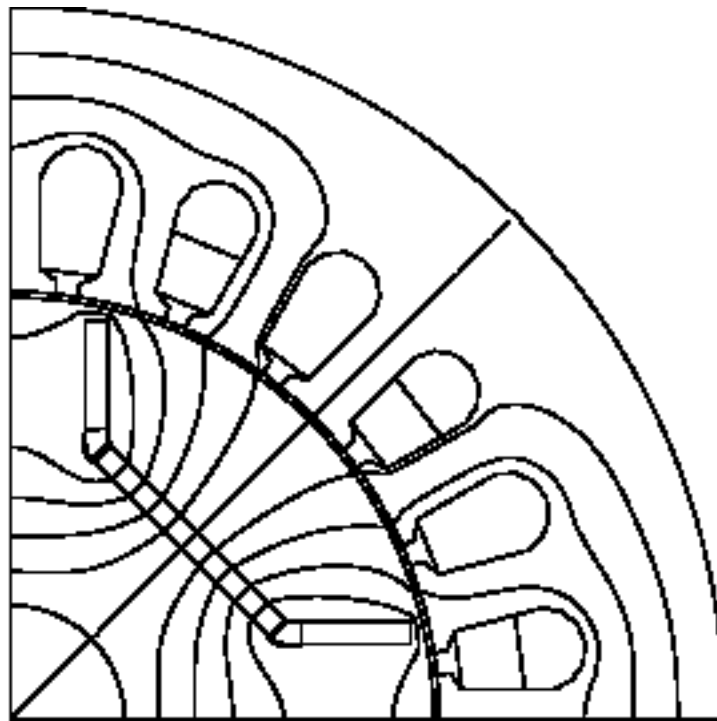


Figure 3.3: Permanent magnet excitation flux plot

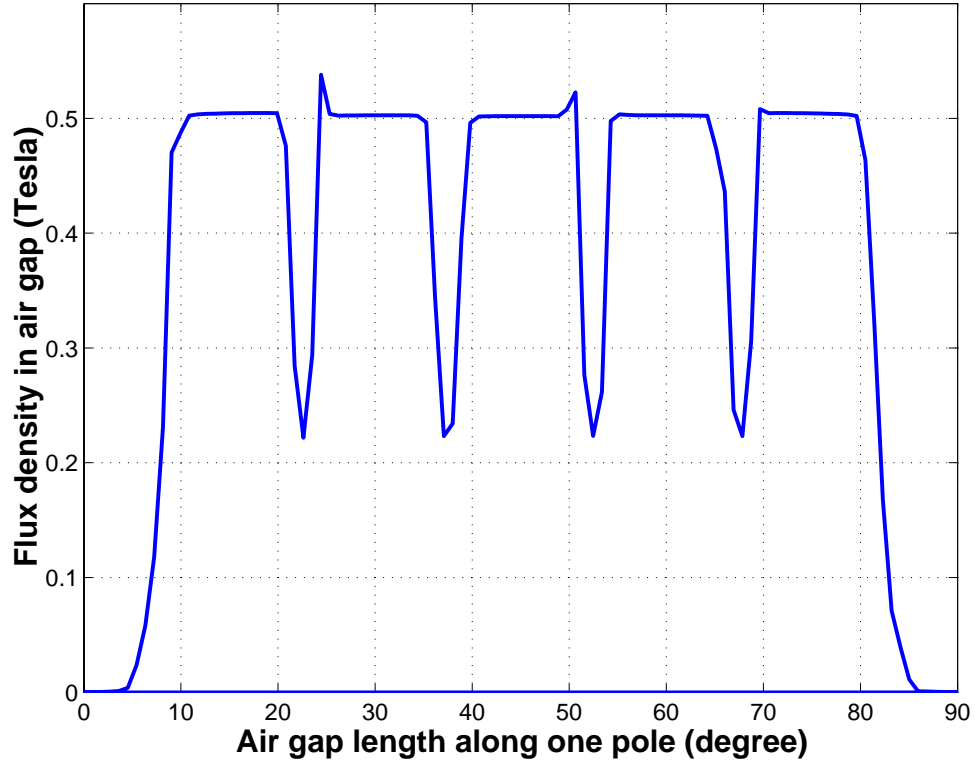


Figure 3.4: Permanent magnet excited flux distribution in the air gap

3.4. There are many design variables in the rotor structure which can affect the flux distribution in the air gap. Rather than complicating the design work with the optimization of all design variables in the rotor, we select only three design variables which mostly determined the magnet flux distribution in the air gap, while keep other design values unchanged. Three design variables are listed below and as shown in Fig. 3.5.

- Magnet thickness (l_m)
- Magnet position (γ)
- Magnet pole angle (α)

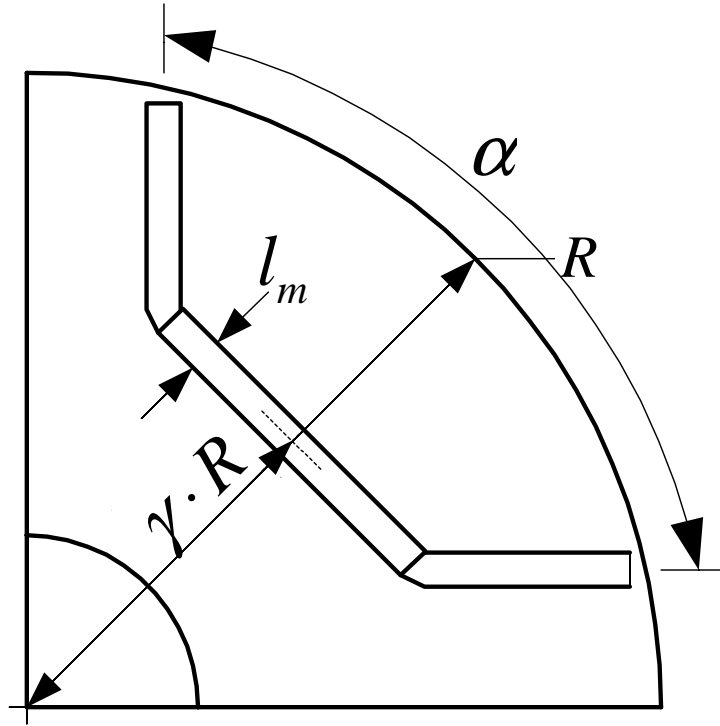


Figure 3.5: Rotor configuration of the interior PMSM

Theoretically, different combination of these variables that can be used to obtain different motor parameters. The design optimization is to choose the optimal combination of these design values to obtain the largest constant power speed range as discussed in Chapter 2.

In addition to achieving maximum constant power speed range, high efficiency and power factor are considered to be design constraints. High efficiency and high power factor are also desirable for any motor drive, but this is particularly critical for the drive system for wide-speed operation in order to minimize the loss and improve the torque capability in the high speed operation.

The NdFeB magnets are the most expensive material in the PMSM. In order to reduce the overall cost of the interior PMSM, it is important to minimize the volume of the permanent magnets, and also to use commercially available permanent magnet blocks. The short time overload capacity of the interior PMSM is constrained by the maximum current that can be carried by the stator winding without permanently demagnetizing the magnets in the rotor.

3.4 Determination of Motor Parameters

3.4.1 Analytical Method

The analytical model of an interior PMSM is derived from generalized electrical machine theory [84]. The magnetomotive force due to a stator winding excitation is expressed in terms of the space distribution and current excitation of the winding. Then the flux of one pole pitch, as a function of stator angle, is calculated by the integral of flux density around the air gap. Finally, the flux linkages of the stator windings are obtained by an integral of the flux multiplied by winding density. Self-inductances and mutual inductances are given by the flux linkage divided by the corresponding current excitation.

3.4.1.1 Stator permanent magnet flux linkage

The chosen magnet material is NdFeB which has a demagnetization characteristics of the form shown in Fig. 1.2. The air gap flux density B_g above the magnets can

be related to magnet's residual flux density B_r , the relative magnet permeability μ_r and the dimension of the magnets by [85].

$$B_g = \frac{l'_m}{g_e} B_r \quad (3.11)$$

where

$$\begin{aligned} l'_m &= l_m / \mu_r \\ g_e &= k_c g + l'_m \end{aligned} \quad (3.12)$$

where k_c is the Carter's effect coefficient, and g_e is the effective air gap length in the d-axis considering the the existence of permanent magnet, and μ_r is the relative permeability of permanent magnets. The air gap flux density profile shown in Fig. 3.4 can be simplified as shown in Fig. 3.6.

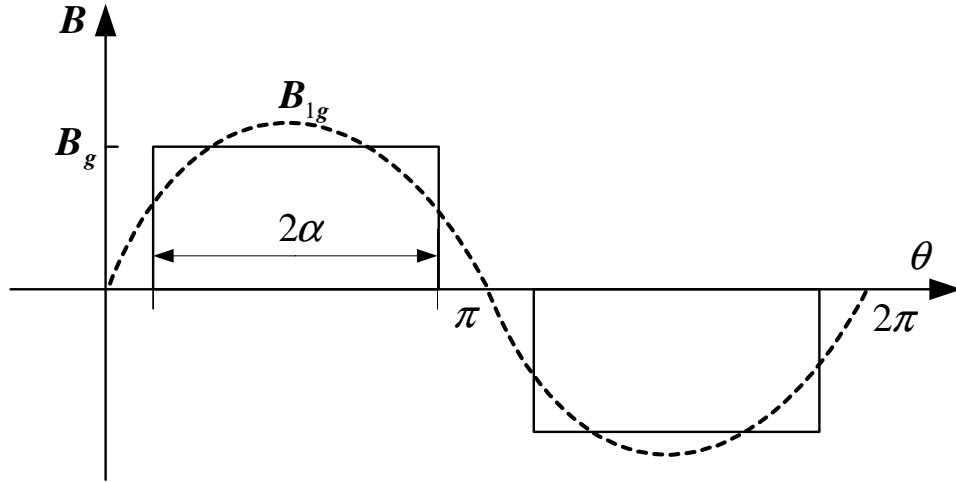


Figure 3.6: Actual and effective air gap flux density

Fig. 3.6 demonstrates the fundamental component of flux density. The rms value of fundamental component of gap flux density is then given by

$$B_{1g} = \frac{2\sqrt{2}}{\pi} B_g \sin \alpha \quad (3.13)$$

The fundamental flux density B_{1g} considering the time component is written as:

$$B_{1g}(t, \theta) = \widehat{B}_{1g} \cos(\omega_s t + \theta) \quad (3.14)$$

As shown in Fig. 3.7, $t = 0$ is the instant as the rotor field axis or d-axis coincides with the phase A axis. θ is defined as the electrical angle in the stator from A-axis. \widehat{B}_{1g} is the peak value of fundamental flux density in the air gap. ω_s is the electrical velocity of rotating flux. The flux in one full pitch coil can be expressed as:

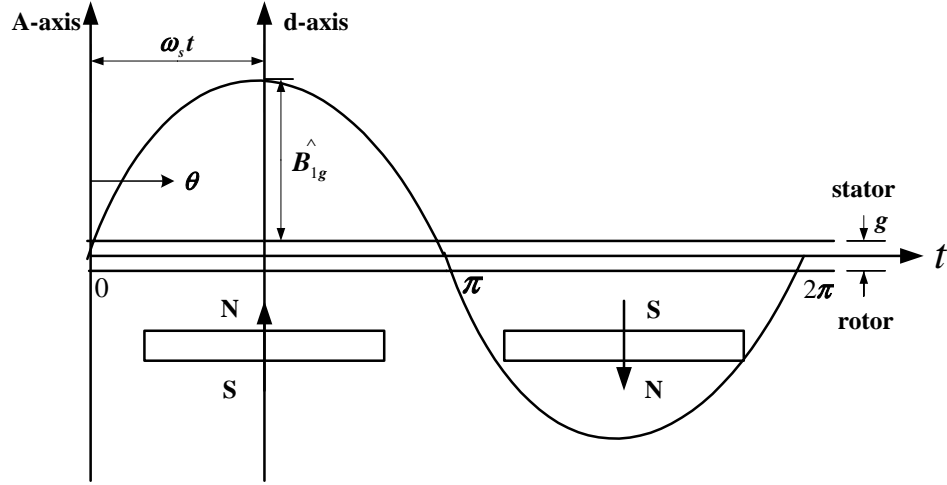


Figure 3.7: Air gap flux distribution due to permanent magnet

$$\phi = \int_0^\pi \frac{\widehat{B}_{1g} \cos(\omega_s t + \theta)}{P} \cdot DL d\theta \quad (3.15)$$

where D is the inner diameter of stator frame, L is the stator stack length and P is the number of poles. Therefore,

$$\phi = \frac{2DL}{P} \widehat{B}_{1g} \sin \omega_s t \quad (3.16)$$

Back EMF in one coil can be written as:

$$e_{\text{coil}} = \frac{d\phi}{dt} = \frac{2DL}{P} \widehat{B}_{1g} \omega_s \cos \omega_s t \quad (3.17)$$

The *RMS* value of total induced voltage per phase for rotating flux is derived from (3.17):

$$E = N_c \cdot \frac{\sqrt{2}DL}{P} \widehat{B_{1g}} \omega_s = 4.44f N_c \Phi \quad (3.18)$$

where

$$\begin{aligned} N_c &= k_\omega N_{ph} \\ \omega_s &= 2\pi f \\ \Phi &= \frac{2DL}{P} \widehat{B_{1g}} \end{aligned} \quad (3.19)$$

N_c is defined as the number of turns per phase in equivalent full pitch winding, and N_{ph} is the number of turns per phase in actual winding. k_ω is the winding factor and Φ is the peak flux passing through one full pitch coil. The stator PM flux linkage λ_m can be derived from (3.18):

$$\lambda_m = \frac{\sqrt{2}E}{\omega_s} = \frac{2DL}{P} \widehat{B_{1g}} \cdot k_\omega N_{ph} \quad (3.20)$$

3.4.1.2 Calculation of inductances

Fig. 3.8 shows a full-pitch armature winding coil in a P-pole machine which has one such coil for each pair of poles.

If the coil has N_c turns and θ is the space angle in electrical degree measured from a coil side, the MMF wave form can be represented by the Fourier series:

$$F_a(\theta) = \frac{N_c I_a}{P} \cdot \frac{4}{\pi} [\sin \theta + \frac{1}{3} \sin 3\theta + \dots + \frac{1}{(2n-1)} \sin (2n-1)\theta] \quad (3.21)$$

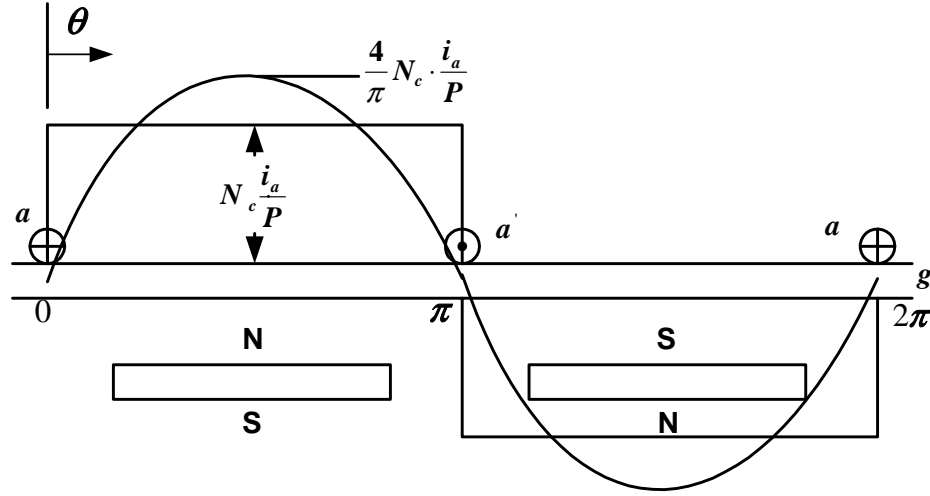


Figure 3.8: MMF distribution of an interior PMSM over 180°

If the phase current I_a lags that phase voltage by θ_i , then

$$I_a = \sqrt{2}I \sin(\omega_s t - \theta_i) \quad (3.22)$$

and the instantaneous value of the fundamental MMF in the air gap at the space angle θ is:

$$F_{a1}(\theta) = \frac{\sqrt{2}N_c I}{P} \cdot \frac{4}{\pi} \sin \theta \sin(\omega_s t - \theta_i) \quad (3.23)$$

The winding detail and MMFs of phase B and phase C can be found by symmetry, i.e. replacing θ_i with $(\theta_i + 2\pi/3)$ and $(\theta_i - 2\pi/3)$ respectively. The total instant value of fundamental MMF is expressed as:

$$F(\theta) = F_{a1}(\theta) + F_{b1}(\theta) + F_{c1}(\theta) = \frac{3}{2} \frac{\sqrt{2}N_c I}{P} \cdot \frac{4}{\pi} \cos(\theta - \omega_s t + \theta_i) \quad (3.24)$$

The flux density in the air gap due to total MMF are written as:

$$B_s(t, \theta) = \frac{F(\theta)\mu_0}{g'} = \frac{3}{2} \frac{\sqrt{2}N_c I \mu_0}{P g'} \cdot \frac{4}{\pi} \cos(\theta - \omega_s t + \theta_i) \quad (3.25)$$

where g' is the air gap length at any position. The peak flux density and the flux

passing through one full pitch coil due to armature reaction can be written as:

$$\begin{aligned}\widehat{B}_s &= \frac{3}{2} \frac{\sqrt{2} N_c I \mu_0}{P g'} \cdot \frac{4}{\pi} \\ \Phi &= \frac{2DL}{P} \widehat{B}_s\end{aligned}\quad (3.26)$$

The back EMF induced in one phase due to rotating flux can be expressed as:

$$E = 4.44 f N_c \Phi = \frac{3\mu_0 \cdot 2\pi f \cdot N_c^2 \cdot DL}{\pi g' (P/2)^2} \cdot I \quad (3.27)$$

Therefore, the synchronous reactance and inductance can be written as:

$$X_s = \frac{E}{I} = \frac{3\mu_0 \cdot 2\pi f \cdot N_c^2 \cdot DL}{\pi g' (P/2)^2} \quad (3.28)$$

$$L_s = \frac{3\mu_0 \cdot (k_\omega N_{ph})^2 \cdot DL}{\pi g' (P/2)^2} \quad (3.29)$$

In order to obtain the d- and q-axis inductances for required interior PMSM from (3.28), we can derive the air gap length g' for d-axis and q-axis from the following Fig. 3.9, where φ is the electrical angle measured from the d-axis. For

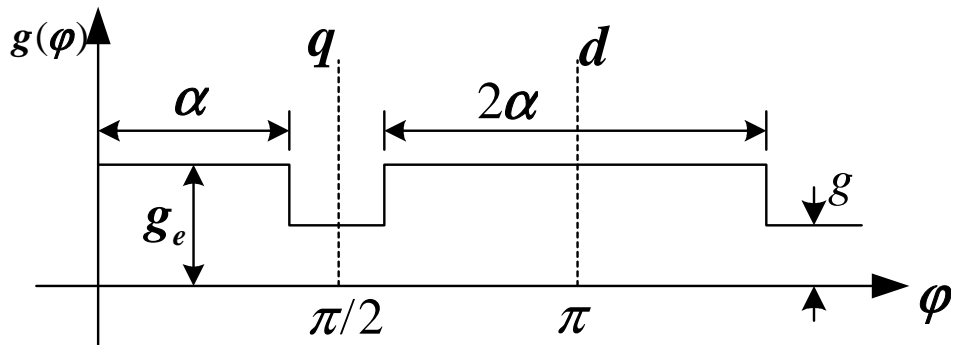


Figure 3.9: Air gap profile along the rotor surface

d-axis armature MMF, we have

$$F_{ad}(\varphi) = \widehat{F}_{ad} \cos(\varphi) \quad (3.30)$$

Therefore, the flux density in the air gap is written as:

$$B_{\text{ad}}(\varphi) = \mu_0 \frac{\widehat{F_{\text{ad}}} \cos(\varphi)}{g(\varphi)} \quad (3.31)$$

Using Fourier analysis, the fundamental peak value of d-axis flux density due to d-axis MMF can be derived as:

$$\widehat{B_{1\text{ad}}} = \frac{2}{\pi} \mu_0 \widehat{F_{\text{ad}}} \int_0^\pi \frac{\cos^2 \varphi}{g(\varphi)} d\varphi \quad (3.32)$$

Since,

$$\begin{cases} g(\varphi) = g_e & 0 < \varphi < \alpha \\ g(\varphi) = k_c g & \alpha < \varphi < \pi - \alpha \\ g(\varphi) = g_e & \pi - \alpha < \varphi < \pi \end{cases} \quad (3.33)$$

Therefore, $\widehat{B_{1\text{ad}}}$ can be derived from (3.32) as:

$$\begin{aligned} \widehat{B_{1\text{ad}}} &= \frac{2}{\pi} \mu_0 \widehat{F_{\text{ad}}} \left[\int_0^\alpha \frac{\cos^2 \varphi}{g_e} d\varphi + \int_\alpha^{\pi-\alpha} \frac{\cos^2 \varphi}{k_c g} d\varphi + \int_{\pi-\alpha}^\pi \frac{\cos^2 \varphi}{g_e} d\varphi \right] \\ \widehat{B_{1\text{ad}}} &= \mu_0 \frac{\widehat{F_{\text{ad}}}}{k_c g} \left[(\pi - 2\alpha - \sin 2\alpha) + \frac{k_c g}{g_e} (2\alpha + \sin 2\alpha) \right] \frac{1}{\pi} \end{aligned} \quad (3.34)$$

If we define k_d as:

$$k_d = \left[(\pi - 2\alpha - \sin 2\alpha) + \frac{k_c g}{g_e} (2\alpha + \sin 2\alpha) \right] \frac{1}{\pi} \quad (3.35)$$

Therefore, (3.34) can be rewritten as:

$$\widehat{B_{1\text{ad}}} = \mu_0 \frac{\widehat{F_{\text{ad}}}}{k_c g} \cdot k_d \quad (3.36)$$

Assuming that the total MMF axis is coincident with the d-axis, we can get:

$$F_{\text{ad}}(\varphi) = F(\theta) \quad (3.37)$$

Thus d-axis magnetizing inductance can be expressed using (3.19), (3.28) and (3.34) as:

$$L_d = \frac{3\pi}{4} \mu_0 \left(\frac{4/\pi k_\omega N_{ph}}{P} \right)^2 \frac{DL}{k_c g} k_d \quad (3.38)$$

Similarly, q-axis magnetizing inductance can be expressed as:

$$L_q = \frac{3\pi}{4} \mu_0 \left(\frac{4/\pi k_\omega N_{ph}}{P} \right)^2 \frac{DL}{k_c g} k_q \quad (3.39)$$

where,

$$\begin{aligned} \widehat{B_{1aq}} &= \mu_0 \frac{\widehat{F_{aq}}}{k_c g} \cdot k_q \\ k_q &= [(\pi - 2\alpha + \sin 2\alpha) + \frac{k_c g}{g_e} [2\alpha - \sin 2\alpha]] \frac{1}{\pi} \end{aligned} \quad (3.40)$$

3.4.2 Finite Element Method

A two dimensional finite element analysis software package (Flux2D, Magsoft) was used to obtain a complete solution of the field in a cross-section of the interior PMSM. However, Flux2D cannot provide direct solution for d- and q-axis inductances, but we can derive them from field computation results of three phase flux linkages ($\lambda_a, \lambda_b, \lambda_c$) by using Park's transformation defined in (2.11).

For three-phase PMSMs, the stator PM flux linkage can be evaluated by setting the magnets to normal magnetization but setting the winding current to zero. Three phases winding flux linkage due to permanent magnet excitation can be computed by Flux2D as ($\lambda_{a0}, \lambda_{b0}, \lambda_{c0}$), which can be transformed to d-axis and q-axis flux linkage (λ_{d0} and λ_{q0}) as shown in:

$$\begin{bmatrix} \lambda_{q0} \\ \lambda_{d0} \\ \lambda_0 \end{bmatrix} = 2/3 \begin{bmatrix} \cos(\theta) & \cos(\theta - 2\pi/3) & \cos(\theta + 2\pi/3) \\ \sin(\theta) & \sin(\theta - 2\pi/3) & \sin(\theta + 2\pi/3) \\ 1/2 & 1/2 & 1/2 \end{bmatrix} \begin{bmatrix} \lambda_{a0} \\ \lambda_{b0} \\ \lambda_{c0} \end{bmatrix} \quad (3.41)$$

where θ is the known rotor position. Therefore, the stator PM flux linkage can be obtained by equating ($\lambda_m = \lambda_{d0}$).

For the evaluation of phase winding flux linkage by armature reaction, the three phase currents are inserted into three phase windings and the permanent magnets have to be set to zero magnetization, then the phase flux linkage ($\lambda_a, \lambda_b, \lambda_c$) is computed individually by Flux2D. By Park's transformation, λ_{ad} and λ_{aq} can be obtained as:

$$\begin{bmatrix} \lambda_{aq} \\ \lambda_{ad} \\ \lambda_0 \end{bmatrix} = 2/3 \begin{bmatrix} \cos(\theta) & \cos(\theta - 2\pi/3) & \cos(\theta + 2\pi/3) \\ \sin(\theta) & \sin(\theta - 2\pi/3) & \sin(\theta + 2\pi/3) \\ 1/2 & 1/2 & 1/2 \end{bmatrix} \begin{bmatrix} \lambda_a \\ \lambda_b \\ \lambda_c \end{bmatrix} \quad (3.42)$$

Similarly, I_d and I_q can be obtained as:

$$\begin{bmatrix} I_q \\ I_d \\ I_0 \end{bmatrix} = 2/3 \begin{bmatrix} \cos(\theta) & \cos(\theta - 2\pi/3) & \cos(\theta + 2\pi/3) \\ \sin(\theta) & \sin(\theta - 2\pi/3) & \sin(\theta + 2\pi/3) \\ 1/2 & 1/2 & 1/2 \end{bmatrix} \begin{bmatrix} I_a \\ I_b \\ I_c \end{bmatrix} \quad (3.43)$$

Therefore, d-axis inductance L_d and q-axis inductance L_q can be calculated by following equations:

$$\begin{bmatrix} \lambda_{ad} \\ \lambda_{aq} \end{bmatrix} = \begin{bmatrix} L_d & 0 \\ 0 & L_q \end{bmatrix} \begin{bmatrix} I_d \\ I_q \end{bmatrix} \quad (3.44)$$

It has to be noted that, in above computation of motor parameters by FEM, the stator PM flux linkage and d-q axis inductances are calculated separately. In above

analysis, the effects of stator and rotor flux saturation are considered negligible. In practice, the stator and rotor flux include both of armature reaction flux and magnet flux, hence the saturation effect is more serious. Therefore, the calculated motor parameters by above FEM method may not accurate enough in heavy loading condition.

3.4.3 Response Surface Method

The response surface methodology (RSM) is a collection of mathematical and statistical techniques that are useful for evaluating responses, i.e., the objective physical quantities (motor parameters), which are influenced by several design variables. As the response surface is often described by polynomial representations (determinative equations), we can save computational time for optimization process by evaluating the objective physical quantities by the response surface instead of by the FEM analysis.

3.4.3.1 Building empirical models

In the practical application of RSM in the design optimization of interior PMSM, it is necessary to develop an approximating model to evaluate the motor parameters (λ_m , L_d , L_q) based on design variables (l_m , γ , α). Since the true response function between the motor parameters and the input design variables is unknown, we can develop an approximation of it. Usually, a lower-order polynomial in some relatively small region of the independent variable space is appropriate. In many cases, either

a **first-order** or a **second-order** model is used. In this work, the second-order model is used for several reasons:

- The second order model is very flexible. It can take on a wide variety of function forms, so it will often work well as an approximation to the true response surface.
- It is not too difficult to estimate the parameters in the second-order model. The method of least squares can be used for this purpose.
- There is considerable practical experience indicating that second-order models work well in solving real response surface problems.

A typical second-order response model with three design variables is listed as follows:

$$y = \beta_0 + \beta_1 x_1 + \beta_2 x_2 + \beta_3 x_3 + \beta_{11} x_1^2 + \beta_{22} x_2^2 + \beta_{33} x_3^2 + \beta_{12} x_1 x_2 + \beta_{13} x_1 x_3 + \beta_{23} x_2 x_3 + \varepsilon \quad (3.45)$$

where y is the response which can be stator PM flux linkage (λ_m) or d- or q-axis inductances (L_d , L_q); the β values are the regression coefficients; (x_1, x_2, x_3) are coded design variables for (l_m, γ, α) ; ε is the estimation error. In RSM work it is convenient to transform the natural design variables to coded variables, which are usually defined to be dimensionless with mean zero and the same spread or standard deviation. The coding rule is explained as follows:

$$x_1 = \frac{l_m - [\max(l_m) + \min(l_m)]/2}{[\max(l_m) - \min(l_m)]/2} \quad (3.46)$$

$$x_2 = \frac{\gamma - [\max(\gamma) + \min(\gamma)]/2}{[\max(\gamma) - \min(\gamma)]/2} \quad (3.47)$$

$$x_3 = \frac{\alpha - [\max(\alpha) + \min(\alpha)]/2}{[\max(\alpha) - \min(\alpha)]/2} \quad (3.48)$$

where $\max(x)$ and $\min(x)$ refer to the upper and lower limits for the design variables.

3.4.3.2 Estimation of the regression coefficients

If we let $x_4 = x_1^2$, $x_5 = x_2^2$, $x_6 = x_3^2$, $x_7 = x_1x_2$, $x_8 = x_1x_3$, $x_9 = x_2x_3$ and $\beta_4 = \beta_{11}$, $\beta_5 = \beta_{22}$, $\beta_6 = \beta_{33}$, $\beta_7 = \beta_{12}$, $\beta_8 = \beta_{13}$, $\beta_9 = \beta_{23}$, then (3.45) can be rewritten as:

$$y = \beta_0 + \beta_1x_1 + \beta_2x_2 + \beta_3x_3 + \beta_4x_4 + \beta_5x_5 + \beta_6x_6 + \beta_7x_7 + \beta_8x_8 + \beta_9x_9 + \varepsilon \quad (3.49)$$

which is a linear regression model. The method of least squares is used to estimate the regression coefficients in a multiple linear regression model. Suppose that n observations on the k design variables ($n > k$) are available. Along with each observed response y_i , there is an observation on each regressor variable, and let x_{ij} denote the i th observation of design variable x_j . The data is shown in Table 3.4.

The model equation (3.49) is written in terms of the observations in Table 3.4 as

$$\begin{aligned} y_i &= \beta_0 + \beta_1x_{i1} + \beta_2x_{i2} + \cdots + \beta_kx_{ik} + \varepsilon_i \\ &= \beta_0 + \sum_{j=1}^k \beta_jx_{ij} + \varepsilon_i, \quad i = 1, 2, \dots, n \end{aligned} \quad (3.50)$$

Table 3.4: Data for multiple linear regression

y	x_1	x_2	\cdots	x_k
y_1	x_{11}	x_{12}	\cdots	x_{1k}
y_2	x_{21}	x_{22}	\cdots	x_{2k}
\vdots	\vdots	\vdots	\vdots	\vdots
y_n	x_{n1}	x_{n2}	\cdots	x_{nk}

The method of least squares chooses the β_j ($j = 0$ to k) in (3.50) so that the sum of the squares of the errors, ε_i , are minimized. The error least square function is:

$$L = \sum_{i=1}^n \varepsilon_i^2 = \sum_{i=1}^n (y_i - \beta_0 - \sum_{j=1}^k \beta_j x_{ij})^2 \quad (3.51)$$

The model in terms of the observations (3.50) can be written in matrix notation as:

$$\mathbf{y} = \mathbf{X}\boldsymbol{\beta} + \boldsymbol{\varepsilon} \quad (3.52)$$

where

$$\mathbf{y} = \begin{bmatrix} y_1 \\ y_2 \\ \vdots \\ y_n \end{bmatrix}, \mathbf{X} = \begin{bmatrix} 1 & x_{11} & x_{12} & \cdots & x_{1k} \\ 1 & x_{21} & x_{22} & \cdots & x_{2k} \\ \vdots & \vdots & \vdots & \vdots & \vdots \\ 1 & x_{n1} & x_{n2} & \cdots & x_{nk} \end{bmatrix}, \boldsymbol{\beta} = \begin{bmatrix} \beta_0 \\ \beta_1 \\ \vdots \\ \beta_k \end{bmatrix}, \text{ and } \boldsymbol{\varepsilon} = \begin{bmatrix} \varepsilon_0 \\ \varepsilon_1 \\ \vdots \\ \varepsilon_k \end{bmatrix}$$

In general, \mathbf{y} is an $n \times 1$ vector of the observations, \mathbf{X} is an $n \times (k + 1)$ matrix of the levels of the independent variables, $\boldsymbol{\beta}$ is a $(k + 1) \times 1$ vector of the regression coefficients, and $\boldsymbol{\varepsilon}$ is an $n \times 1$ vector of random errors. In order to find the vector of least squares estimators that minimizes

$$L = \sum_{i=1}^n \varepsilon_i^2 = \boldsymbol{\varepsilon}'\boldsymbol{\varepsilon} = (\mathbf{y} - \mathbf{X}\boldsymbol{\beta})'(\mathbf{y} - \mathbf{X}\boldsymbol{\beta})$$

$$\begin{aligned}
&= \mathbf{y}'\mathbf{y} - \boldsymbol{\beta}'\mathbf{X}'\mathbf{y} - \mathbf{y}'\mathbf{X}\boldsymbol{\beta} + \boldsymbol{\beta}'\mathbf{X}'\mathbf{X}\boldsymbol{\beta} \\
&= \mathbf{y}'\mathbf{y} - 2\boldsymbol{\beta}'\mathbf{X}'\mathbf{y} + \boldsymbol{\beta}'\mathbf{X}'\mathbf{X}\boldsymbol{\beta}
\end{aligned} \tag{3.53}$$

where $\boldsymbol{\beta}'$, $\boldsymbol{\varepsilon}'$ and \mathbf{X}' are transpose of $(\boldsymbol{\beta}, \boldsymbol{\varepsilon}$ and $\mathbf{X})$. Since $\boldsymbol{\beta}'\mathbf{X}'\mathbf{y}$ is a 1×1 matrix, or scalar, and its transpose $(\boldsymbol{\beta}'\mathbf{X}'\mathbf{y})' = \mathbf{y}'\mathbf{X}\boldsymbol{\beta}$ is the same scalar. The least squares estimators must satisfy:

$$\frac{\partial L}{\partial \boldsymbol{\beta}}|_{\mathbf{b}} = -2\mathbf{X}'\mathbf{y} + 2\mathbf{X}'\mathbf{X}\mathbf{b} = 0 \tag{3.54}$$

which simplifies to

$$\mathbf{X}'\mathbf{X}\mathbf{b} = \mathbf{X}'\mathbf{y} \tag{3.55}$$

where \mathbf{b} is the solution of $\boldsymbol{\beta}$. Therefore, the least squares estimator of $\boldsymbol{\beta}$ is

$$\mathbf{b} = (\mathbf{X}'\mathbf{X})^{-1}\mathbf{X}'\mathbf{y} \tag{3.56}$$

The fitted regression model is

$$\hat{\mathbf{y}} = \mathbf{X}\mathbf{b} \tag{3.57}$$

In scalar notation, the fitted model is

$$\hat{y}_i = b_0 + \sum_{j=1}^k b_j x_{ij}, \quad i = 1, 2, \dots, n \tag{3.58}$$

The difference between the observation y_i and the fitted value \hat{y}_i is a residual, say

$e_i = y_i - \hat{y}_i$. The $n \times 1$ vector of residuals is denoted by

$$\mathbf{e} = \mathbf{y} - \hat{\mathbf{y}} \tag{3.59}$$

3.4.3.3 Fitting the second-order model

The regression coefficients are dependent on observations. It is desirable to make the number of experiments carried out by the FEM analysis as small as possible.

The appropriate selection of the points for experiments can reduce the variance of the coefficients, which make the resulting response surface more reliable. The central composite design (CCD) has been widely used for fitting a second-order response surface. The design consists of eight runs at the corner of a cubic, plus six runs at the center of its six faces, plus one run at the cubic center. In terms of the coded variables the corners of the cubic are $(x_1, x_2, x_3) = (-1, -1, -1), (1, -1, -1), (-1, 1, -1), (-1, -1, 1), (1, 1, -1), (1, -1, 1), (-1, 1, 1), (1, 1, 1)$; the six face center points are at $(x_1, x_2, x_3) = (-1, 0, 0), (1, 0, 0), (0, -1, 0), (0, 1, 0), (0, 0, -1), (0, 0, 1)$; and the cubic center point is at $(x_1, x_2, x_3) = (0, 0, 0)$ as shown in Fig. 3.10.

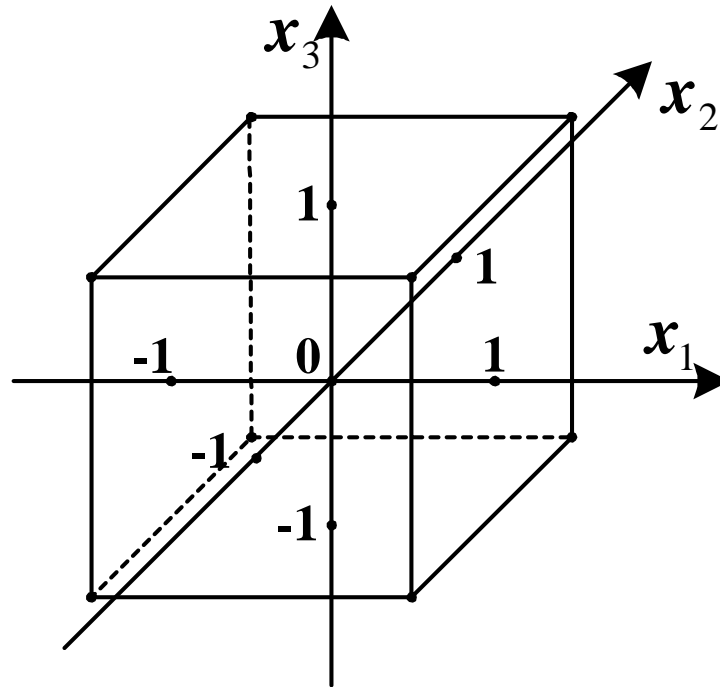


Figure 3.10: Central composite design for second-order model

3.4.3.4 Model adequacy checking

It is necessary to examine the fitted response surface model to ensure that it provides an adequate approximation to the true system. The residuals from the least squares fit, defined in (3.59), play an important role in judging model adequacy.

The sum of squares of the residuals is defined as:

$$SS_E = \sum_{i=1}^n (y_i - \hat{y}_i)^2 = \sum_{i=1}^n e_i^2 = \mathbf{e}'\mathbf{e} \quad (3.60)$$

Substituting $\mathbf{e} = \mathbf{y} - \hat{\mathbf{y}} = \mathbf{y} - \mathbf{X}\mathbf{b}$ and $\mathbf{X}'\mathbf{X}\mathbf{b} = \mathbf{X}'\mathbf{y}$, we can get

$$SS_E = \mathbf{y}'\mathbf{y} - \mathbf{b}'\mathbf{X}'\mathbf{y} \quad (3.61)$$

The total sum of squares is defined as:

$$SS_T = \sum_{i=1}^n (y_i - \bar{y})^2 = \sum_{i=1}^n y_i^2 - (\sum_{i=1}^n y_i)^2/n = \mathbf{y}'\mathbf{y} - (\sum_{i=1}^n y_i)^2/n \quad (3.62)$$

Equation (3.61) can be rewritten as:

$$SS_E = \mathbf{y}'\mathbf{y} - (\sum_{i=1}^n y_i)^2/n - [\mathbf{b}'\mathbf{X}'\mathbf{y} - (\sum_{i=1}^n y_i)^2/n] \quad (3.63)$$

or

$$SS_E = SS_T - SS_R \quad (3.64)$$

Therefore, the regression sum of squares is

$$SS_R = \mathbf{b}'\mathbf{X}'\mathbf{y} - (\sum_{i=1}^n y_i)^2/n \quad (3.65)$$

The coefficient of multiple determination R^2 is defined as:

$$R^2 = \frac{SS_R}{SS_T} = 1 - \frac{SS_E}{SS_T} \quad (3.66)$$

R^2 is a measure of the amount of reduction in the variability of response surface y obtained by using the design variables in the model. Because R^2 always increases as new design variables are added to the model, it is desirable to use an adjusted R^2 statistics defined as:

$$R_{\text{adj}}^2 = 1 - \frac{SS_E/(n-p)}{SS_T/(n-1)} = 1 - \frac{n-1}{n-p}(1-R^2) \quad (3.67)$$

In general, the adjusted R^2 statistics will not always increase as new design variables are added to the model. Therefore, it is more useful to evaluate the adequacy of the fitting model.

3.5 Design of The Rotor Structure

The effects of geometric variables on the motor parameters of a 400 W interior PMSM is assessed by using the proposed RSM model. The geometric specifications for the stator frame and the rotor structure are listed in Appendix A. Considering the rotor geometry and mechanical constraints, as well as the empirical knowledge of machine design with interior PMSMs, the domain of design variables are determined as listed in Table 3.5:

Table 3.5: The domain of design variables in the rotor structure

Design Variable	Min. value	Max. value
l_m (mm)	1.0	3.0
γ	0.5	0.75
α (degree)	50°	75°

Based on central composite design, 15 sets of design variables are selected. The natural design values (l_m , α and γ) and the coding values (x_1 , x_2 and x_3) are listed in Column A and Column B of Table 3.6, respectively. The resultant 15 set of motor parameters (λ_m , L_d and L_q) are computed using Flux2D and they are listed in Column C of Table 3.6.

Table 3.6: Central composite design for the design example of interior PMSM

NO	A			B			C		
	$l_m(mm)$	γ	$\alpha(degree)$	x_1	x_2	x_3	$\lambda_m(Wb)$	$L_d(H)$	$L_q(H)$
1	1	0.5	50	-1	-1	-1	0.001	0.085	0.144
2	3	0.5	50	1	-1	-1	0.001	0.061	0.144
3	1	0.75	50	-1	1	-1	0.196	0.080	0.159
4	1	0.5	75	-1	-1	1	0.199	0.076	0.131
5	3	0.75	50	1	1	-1	0.258	0.058	0.159
6	3	0.5	75	1	-1	1	0.264	0.052	0.131
7	1	0.75	75	-1	1	1	0.404	0.072	0.157
8	3	0.75	75	1	1	1	0.520	0.050	0.157
9	1	0.625	62.5	-1	0	0	0.198	0.076	0.152
10	3	0.625	62.5	1	0	0	0.262	0.051	0.152
11	2	0.5	62.5	0	-1	0	0.118	0.061	0.137
12	2	0.75	62.5	0	1	0	0.374	0.057	0.158
13	2	0.625	50	0	0	-1	0.106	0.066	0.154
14	2	0.625	75	0	0	1	0.363	0.058	0.150
15	2	0.625	62.5	0	0	0	0.244	0.059	0.152

These 15 sets of motor parameters computed by FEM are used to fit the second-order response surface models for λ_m , L_d and L_q . For simplicity, here we use λ_m as the example to explain the procedure of fitting the second-order response

surface model (3.45). The matrix \mathbf{X} and vector \mathbf{y} for this model are

$$\mathbf{X} = \begin{bmatrix} 1 & x_1 & x_2 & x_3 & x_4 & x_5 & x_6 & x_7 & x_8 & x_9 \\ 1 & -1 & -1 & -1 & 1 & 1 & 1 & 1 & 1 & 1 \\ 1 & 1 & -1 & -1 & 1 & 1 & 1 & -1 & -1 & 1 \\ 1 & -1 & 1 & -1 & 1 & 1 & 1 & -1 & 1 & -1 \\ 1 & -1 & -1 & 1 & 1 & 1 & 1 & 1 & -1 & -1 \\ 1 & 1 & 1 & -1 & 1 & 1 & 1 & 1 & -1 & -1 \\ 1 & 1 & -1 & 1 & 1 & 1 & 1 & -1 & 1 & -1 \\ 1 & -1 & 1 & 1 & 1 & 1 & 1 & -1 & -1 & 1 \\ 1 & 1 & 1 & 1 & 1 & 1 & 1 & 1 & 1 & 1 \\ 1 & -1 & 0 & 0 & 1 & 0 & 0 & 0 & 0 & 0 \\ 1 & 1 & 0 & 0 & 1 & 0 & 0 & 0 & 0 & 0 \\ 1 & 0 & -1 & 0 & 0 & 1 & 0 & 0 & 0 & 0 \\ 1 & 0 & 1 & 0 & 0 & 1 & 0 & 0 & 0 & 0 \\ 1 & 0 & 0 & -1 & 0 & 0 & 1 & 0 & 0 & 0 \\ 1 & 0 & 0 & 1 & 0 & 0 & 1 & 0 & 0 & 0 \\ 1 & 0 & 0 & 0 & 0 & 0 & 0 & 0 & 0 & 0 \end{bmatrix}, \mathbf{y} = \begin{bmatrix} 0.001 \\ 0.001 \\ 0.196 \\ 0.199 \\ 0.258 \\ 0.264 \\ 0.404 \\ 0.520 \\ 0.198 \\ 0.262 \\ 0.118 \\ 0.374 \\ 0.106 \\ 0.363 \\ 0.244 \end{bmatrix}$$

The matrix $\mathbf{X}'\mathbf{X}$ and vector $\mathbf{X}'\mathbf{y}$ are

$$\mathbf{X}'\mathbf{X} = \begin{bmatrix} 15 & 0 & 0 & 0 & 10 & 10 & 10 & 0 & 0 & 0 \\ 0 & 10 & 0 & 0 & 0 & 0 & 0 & 0 & 0 & 0 \\ 0 & 0 & 10 & 0 & 0 & 0 & 0 & 0 & 0 & 0 \\ 0 & 0 & 0 & 10 & 0 & 0 & 0 & 0 & 0 & 0 \\ 10 & 0 & 0 & 0 & 10 & 8 & 8 & 0 & 0 & 0 \\ 10 & 0 & 0 & 0 & 8 & 10 & 8 & 0 & 0 & 0 \\ 10 & 0 & 0 & 0 & 8 & 8 & 10 & 0 & 0 & 0 \\ 0 & 0 & 0 & 0 & 0 & 0 & 0 & 8 & 0 & 0 \\ 0 & 0 & 0 & 0 & 0 & 0 & 0 & 0 & 8 & 0 \\ 0 & 0 & 0 & 0 & 0 & 0 & 0 & 0 & 0 & 8 \end{bmatrix}, \mathbf{X}'\mathbf{y} = \begin{bmatrix} 3.507 \\ 0.308 \\ 1.168 \\ 1.188 \\ 2.303 \\ 2.334 \\ 2.311 \\ 0.113 \\ 0.120 \\ 0.010 \end{bmatrix}$$

and from $\mathbf{b} = (\mathbf{X}'\mathbf{X})^{-1}\mathbf{X}'\mathbf{y}$, we obtain

$$\mathbf{b} = \begin{bmatrix} 0.241 \\ 0.031 \\ 0.117 \\ 0.119 \\ -0.01 \\ 0.006 \\ -0.006 \\ 0.014 \\ 0.015 \\ 0.001 \end{bmatrix}$$

Therefore the fitted model for λ_m is

$$\hat{y} = 0.241 + 0.031x_1 + 0.117x_2 + 0.119x_3 - 0.01x_1^2 + 0.006x_2^2 - 0.006x_3^2$$

$$+ 0.014x_1x_2 + 0.015x_1x_3 + 0.001x_2x_3 \quad (3.68)$$

In terms of the natural design variables, the model is

$$\begin{aligned} \lambda_m = & 0.241 + 0.031(l_m - 1) + 0.117\left(\frac{\gamma - 0.625}{0.125}\right) + 0.119\left(\frac{\alpha - 62.5}{12.5}\right) - 0.01(l_m - 1)^2 \\ & + 0.006\left(\frac{\gamma - 0.625}{0.125}\right)^2 - 0.006\left(\frac{\alpha - 62.5}{12.5}\right)^2 + 0.014(l_m - 1)\left(\frac{\gamma - 0.625}{0.125}\right) \\ & + 0.015(l_m - 1)\left(\frac{\alpha - 62.5}{12.5}\right) + 0.001\left(\frac{\gamma - 0.625}{0.125}\right)\left(\frac{\alpha - 62.5}{12.5}\right) \end{aligned} \quad (3.69)$$

Similarly, we can fit the second-order response surface model for L_d and L_q

$$\begin{aligned} L_d = & 0.059 - 0.012(l_m - 1) - 0.002\left(\frac{\gamma - 0.625}{0.125}\right) - 0.004\left(\frac{\alpha - 62.5}{12.5}\right) - 0.005(l_m - 1)^2 \\ & - 0.0001\left(\frac{\gamma - 0.625}{0.125}\right)^2 + 0.004\left(\frac{\alpha - 62.5}{12.5}\right)^2 + 0.001(l_m - 1)\left(\frac{\gamma - 0.625}{0.125}\right) \\ & + 0.0001(l_m - 1)\left(\frac{\alpha - 62.5}{12.5}\right) + 0.0002\left(\frac{\gamma - 0.625}{0.125}\right)\left(\frac{\alpha - 62.5}{12.5}\right) \end{aligned} \quad (3.70)$$

$$\begin{aligned} L_q = & 0.152 + 0.001(l_m - 1) + 0.01\left(\frac{\gamma - 0.625}{0.125}\right) - 0.003\left(\frac{\alpha - 62.5}{12.5}\right) - 0.001(l_m - 1)^2 \\ & - 0.004\left(\frac{\gamma - 0.625}{0.125}\right)^2 - 0.001\left(\frac{\alpha - 62.5}{12.5}\right)^2 + 0.001(l_m - 1)\left(\frac{\gamma - 0.625}{0.125}\right) \\ & + 0.001(l_m - 1)\left(\frac{\alpha - 62.5}{12.5}\right) + 0.003\left(\frac{\gamma - 0.625}{0.125}\right)\left(\frac{\alpha - 62.5}{12.5}\right) \end{aligned} \quad (3.71)$$

The calculation of motor parameters using traditional analytical method and FEM method are also conducted to verify the accuracy of RSM model. Table 3.7 shows the observed values for (λ_m, L_d, L_q) by FEM, the fitted values by RSM and the derived values by Analytical Method (AM). The 15 examined points for design variables (l_m, γ, α) are the same points listed in Column A in Table 3.6.

From the comparison of results listed in Table 3.7 and the error or residual between RSM and FEM listed in Table 3.8, it is noted that fitted values by second-order RSM is much closer to the observed values by FEM.

Table 3.7: Comparison of results with AM, FEM and RSM

No.	AM			FEM			RSM		
	λ_m (Wb)	L_d (H)	L_q (H)	λ_m (Wb)	L_d (H)	L_q (H)	λ_m (Wb)	L_d (H)	L_q (H)
1	0.245	0.075	0.134	0.001	0.085	0.144	-0.006	0.085	0.143
2	0.272	0.046	0.126	0.001	0.061	0.144	-0.003	0.061	0.143
3	0.342	0.075	0.134	0.196	0.080	0.159	0.197	0.080	0.158
4	0.334	0.062	0.089	0.199	0.076	0.131	0.199	0.076	0.132
5	0.397	0.046	0.126	0.258	0.058	0.159	0.257	0.058	0.158
6	0.374	0.028	0.068	0.264	0.052	0.131	0.263	0.052	0.132
7	0.464	0.062	0.089	0.404	0.072	0.157	0.407	0.072	0.157
8	0.544	0.028	0.068	0.520	0.050	0.157	0.527	0.050	0.157
9	0.353	0.066	0.114	0.198	0.076	0.152	0.200	0.075	0.152
10	0.403	0.033	0.100	0.262	0.051	0.152	0.262	0.052	0.152
11	0.318	0.043	0.105	0.118	0.061	0.137	0.130	0.061	0.137
12	0.458	0.043	0.105	0.374	0.057	0.158	0.364	0.057	0.158
13	0.324	0.055	0.128	0.106	0.066	0.154	0.116	0.067	0.155
14	0.444	0.038	0.075	0.363	0.058	0.156	0.354	0.058	0.149
15	0.389	0.043	0.105	0.244	0.059	0.152	0.241	0.059	0.152

The residual analysis in Table 3.9 further confirms the adequacy of fitted second-order RSM model. From the equations (3.62), (3.65) and (3.63), the adjusted coefficients of multiple determination R_{adj}^2 for three responses (λ_m , L_d and L_q) are 0.9943, 0.9994 and 0.9915, respectively. Therefore we can expect the fitted second-order response surface model to explain about 99% of the variability observed in the responses. The overall adequacy of the model based on least squares fit is satisfactory.

The effects of rotor geometry on stator PM flux linkage (λ_m), d-axis induc-

Table 3.8: Residual for the fitted second-order RSM model

	$e(\lambda_m)$	$e(L_d)$	$e(L_q)$
No.	Wb	$\times 10^{-3}H$	$\times 10^{-3}H$
1	0.007	-0.063	0.030
2	0.004	0.086	0.030
3	-0.001	-0.108	0.030
4	-0.001	-0.123	-0.030
5	0.001	0.116	0.030
6	0.001	0.101	-0.030
7	-0.004	-0.09	-0.030
8	-0.007	0.056	-0.030
9	-0.002	0.338	0.000
10	0.001	-0.358	0.000
11	-0.012	0.000	0.000
12	0.011	0.030	0.000
13	-0.011	-0.030	-1.200
14	0.010	0.060	1.200
15	0.002	-0.060	0.000

Table 3.9: Test of adequacy for the fitted second-order RSM model

Response	SS_E	SS_R	SS_T	R_{adj}^2
λ_m	5.92×10^{-4}	0.2909	0.2915	0.9943
L_d	3.62×10^{-7}	0.0018	0.0018	0.9994
L_q	3.82×10^{-6}	0.0012	0.0013	0.9915

tance (L_d) and q-axis inductance (L_q) as calculated by the fitted second-order RSM model are shown in Fig. 3.11, Fig. 3.12 and Fig. 3.13. The following observations are made from these results.

- The stator PM flux linkage can be changed by changing the volume of permanent magnets. Modifying the magnet pole angle is more effective than

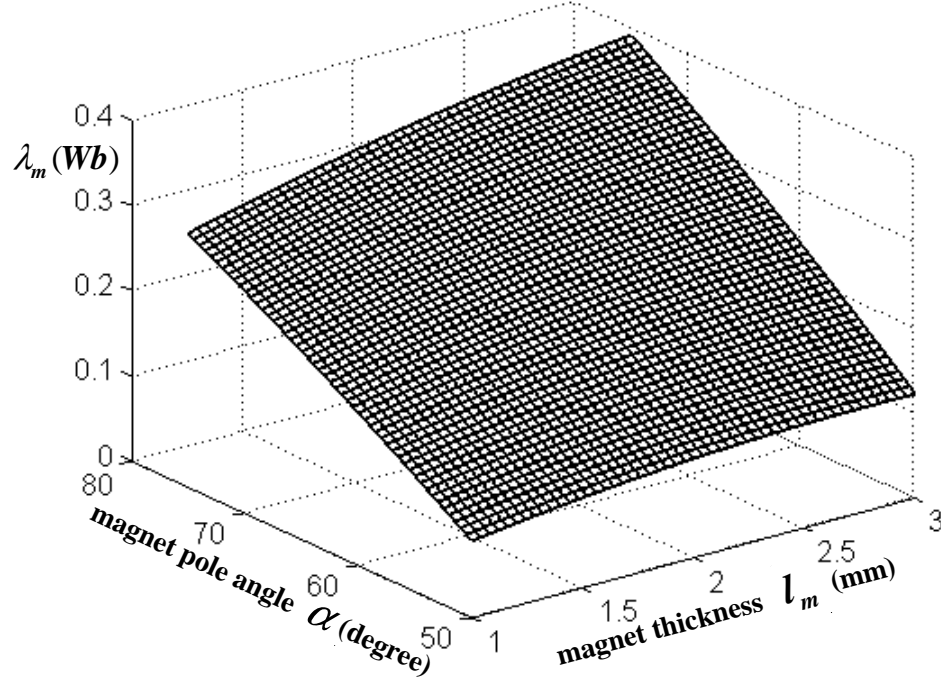


Figure 3.11: λ_m as a function of rotor geometry

changing the magnet thickness;

- The d-axis inductance can be increased by reducing the magnet thickness.

Changing l_m has little effects on the q-axis inductance;

- The q-axis inductance can be changed by changing the magnet position in the rotor. Higher magnet position provides larger q-axis inductance, but exposes permanent magnets to higher demagnetizing fields.

The fitted second-order model not only gives a clear representation of the motor parameters of the interior PMSM as a function of design variables, but also allows the optimization process to evaluate the objective physical quantity (constant power speed range) in a much shorter time. Based on the RSM models

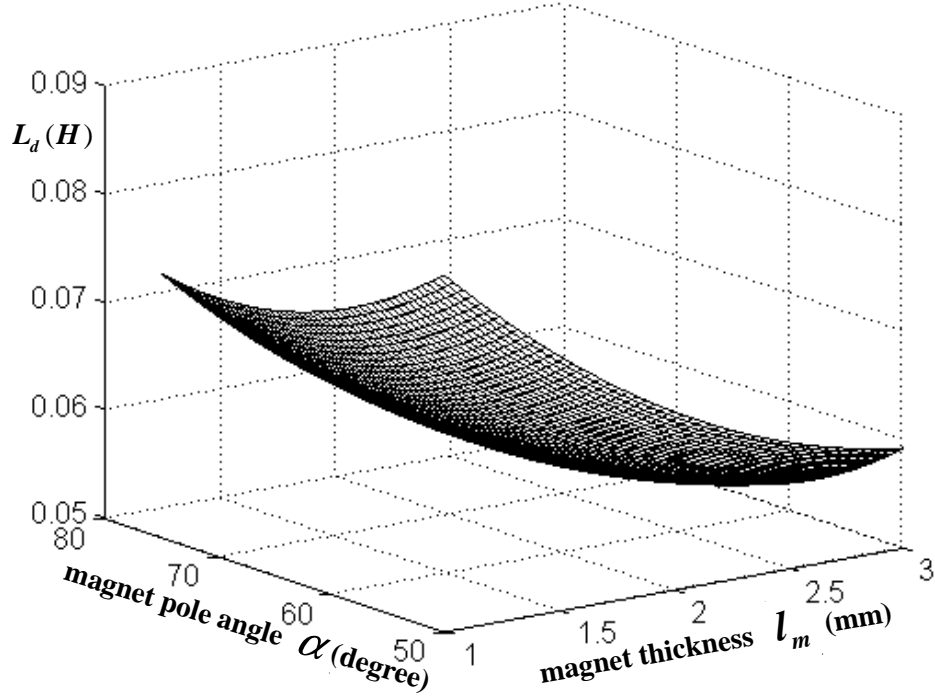


Figure 3.12: L_d as a function of rotor geometry

(3.69, 3.70 and 3.71) of motor parameters (λ_m , L_d and L_q) as well as the known constraints of voltage and current, we can obtain the maximum power capability over a wide speed range, which has been described in Chapter 2. Therefore, in the numerical optimization process, the objective quantity (constant power speed range) can be evaluated by the polynomial functions instead of the iterative field calculation. As a result, we can achieve an overall increase in the optimization speed. The detail optimization process based on RSM will be developed in Chapter 4.

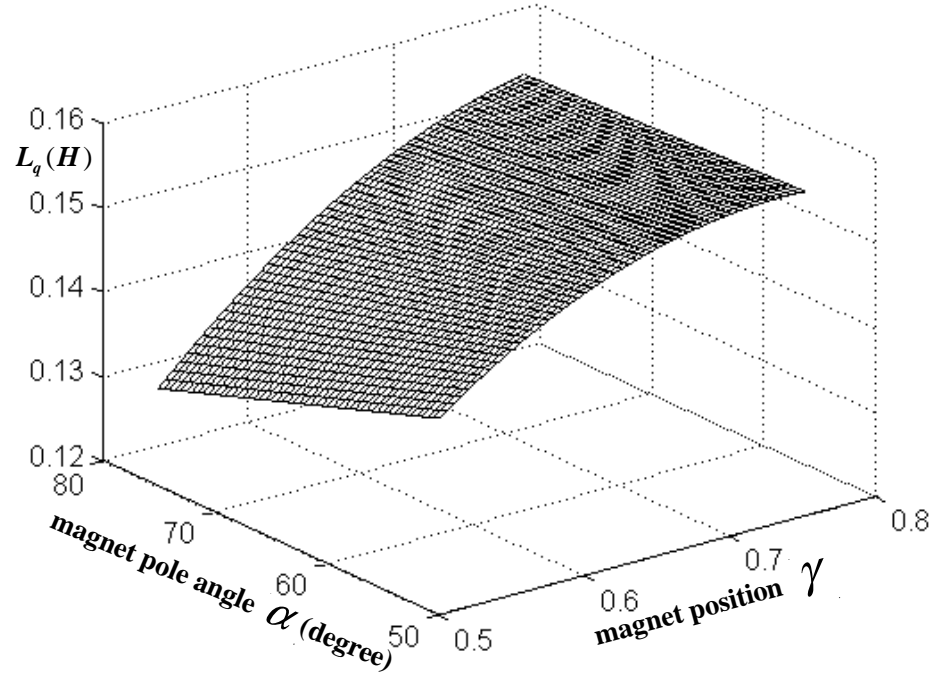


Figure 3.13: L_q as a function of rotor geometry

3.6 Conclusion

In this chapter, the effect of geometric parameters on the motor parameters of interior PMSMs has been investigated using both analytical method and finite element method. In order to achieve a computationally simple and accurate motor parameters determination in the iterative process of numerical optimization, an effective computational approach which combines magnetic field analysis and analytical equations by response surface methodology (RSM) was proposed for the prediction of motor parameters in interior PMSMs. The polynomial representation of motor parameters (L_d , L_q and λ_{pm}) by RSM are derived and their accuracy in selected geometric space of rotor structure are validated by FEM.

Chapter 4

Numerical Optimization of an Interior PMSM for Wide Constant Power Speed Range

4.1 Introduction

Numerical computation using finite element method (FEM) is considered indispensable for electrical machine design. However, it is difficult to carry out iterative field computation in every step of an optimization process. In order to save the computation time, an effective computational approach was developed in Chapter 3, which applies the response surface methodology (RSM) in stead of FEM to determine motor parameters (λ_m , L_d and L_q) in interior PMSMs. Based on the motor parameters using RSM, we can obtain the maximum power capability for a wide speed range as described in Chapter 2. In this chapter we develop an numerical optimization process using genetic algorithm (GA) to search for an optimum rotor structure (l_m , γ and α) for a 400 W interior PMSM, which has the largest constant power speed range (CPSR) under certain constraints.

4.2 Optimization Method

The design objective of an interior PMSM is to find the optimum rotor structure which can achieve the largest constant power speed range (CPSR) under certain constraints. Therefore, optimization technique has to be applied to look for the maximum of the objective function, which is also the global maximum of the function. The Genetic Algorithm (GA) technique has proved to be an effective tool for motor design optimization as it allows a search in a wide region and a global optimization to be performed [86]. However, GA requires the objective function to be computed several times (especially when FEM is adopted to improve the accuracy of the evaluation) and thus requires substantially more computational time than other optimization techniques. In this work, we adopt the fitted second-order model by RSM as the evaluation tool for the objective function and apply GA as the search method. This enables us to save the computational time in the design optimization process but without losing the accuracy in the evaluation of the objective function.

4.2.1 Formulation of the design optimization

The task of the design optimization of an interior PMSM is to find a vector of design variables $\mathbf{X} = (x_1, x_2, x_3)$, which represents the natural design variables (l_m, γ, α) , each of them bounded by $x_{\min} < x_i < x_{\max}$, $i = 1, 2, 3$, so that the

objective function $O(\mathbf{X})$ as:

$$CPSR = \frac{\omega_{\max}}{\omega_{\text{rated}}} = f(L_d, L_q, \lambda_m) \quad (4.1)$$

is maximized, where ω_{\max} is the maximum speed in which the interior PMSM can deliver rated output power and ω_{rated} is motor rated speed. The voltage and current constraints are:

$$\begin{aligned} V_s &= \sqrt{V_d^2 + V_q^2} < V_{\text{sm}} \\ I_s &= \sqrt{I_d^2 + I_q^2} < I_{\text{sm}} \end{aligned} \quad (4.2)$$

The solution for CPSR are described as follows:

Every vector of design variables $\mathbf{X} = (x_1, x_2, x_3)$ (l_m, γ, α) determines one set of motor parameters (λ_m, L_d and L_q) according to fitted second order RSM model developed in Chapter 3:

$$\begin{aligned} \lambda_m &= 0.241 + 0.031(l_m - 1) + 0.117\left(\frac{\gamma - 0.625}{0.125}\right) + 0.119\left(\frac{\alpha - 62.5}{12.5}\right) - 0.01(l_m - 1)^2 \\ &+ 0.006\left(\frac{\gamma - 0.625}{0.125}\right)^2 - 0.006\left(\frac{\alpha - 62.5}{12.5}\right)^2 + 0.014(l_m - 1)\left(\frac{\gamma - 0.625}{0.125}\right) \\ &+ 0.015(l_m - 1)\left(\frac{\alpha - 62.5}{12.5}\right) + 0.001\left(\frac{\gamma - 0.625}{0.125}\right)\left(\frac{\alpha - 62.5}{12.5}\right) \end{aligned} \quad (4.3)$$

$$\begin{aligned} L_d &= 0.059 - 0.012(l_m - 1) - 0.002\left(\frac{\gamma - 0.625}{0.125}\right) - 0.004\left(\frac{\alpha - 62.5}{12.5}\right) - 0.005(l_m - 1)^2 \\ &- 0.0001\left(\frac{\gamma - 0.625}{0.125}\right)^2 + 0.004\left(\frac{\alpha - 62.5}{12.5}\right)^2 + 0.001(l_m - 1)\left(\frac{\gamma - 0.625}{0.125}\right) \\ &+ 0.0001(l_m - 1)\left(\frac{\alpha - 62.5}{12.5}\right) + 0.0002\left(\frac{\gamma - 0.625}{0.125}\right)\left(\frac{\alpha - 62.5}{12.5}\right) \end{aligned} \quad (4.4)$$

$$\begin{aligned} L_q &= 0.152 + 0.001(l_m - 1) + 0.01\left(\frac{\gamma - 0.625}{0.125}\right) - 0.003\left(\frac{\alpha - 62.5}{12.5}\right) - 0.001(l_m - 1)^2 \\ &- 0.004\left(\frac{\gamma - 0.625}{0.125}\right)^2 - 0.001\left(\frac{\alpha - 62.5}{12.5}\right)^2 + 0.001(l_m - 1)\left(\frac{\gamma - 0.625}{0.125}\right) \\ &+ 0.001(l_m - 1)\left(\frac{\alpha - 62.5}{12.5}\right) + 0.003\left(\frac{\gamma - 0.625}{0.125}\right)\left(\frac{\alpha - 62.5}{12.5}\right) \end{aligned} \quad (4.5)$$

Every set of motor parameters (λ_m , L_d and L_q) determines maximum torque-speed profile as follows:

$$T_{\max} = \begin{cases} T_m & 0 < \omega_s < \omega_b \\ T_n & \omega_b < \omega_s < \omega_p \\ T_p & \omega_s > \omega_p \end{cases} \quad (4.6)$$

where T_m (2.28) is the peak torque produced by rated current; T_n (2.37) and T_p (2.55) are current and voltage limited maximum torque, respectively, which are the functions of motor parameters (λ_m , L_d and L_q) and motor speed ω_s as described in Chapter 2. Therefore, we can obtain the maximum power capability curve with respect to speed according to torque-speed profile using following equation:

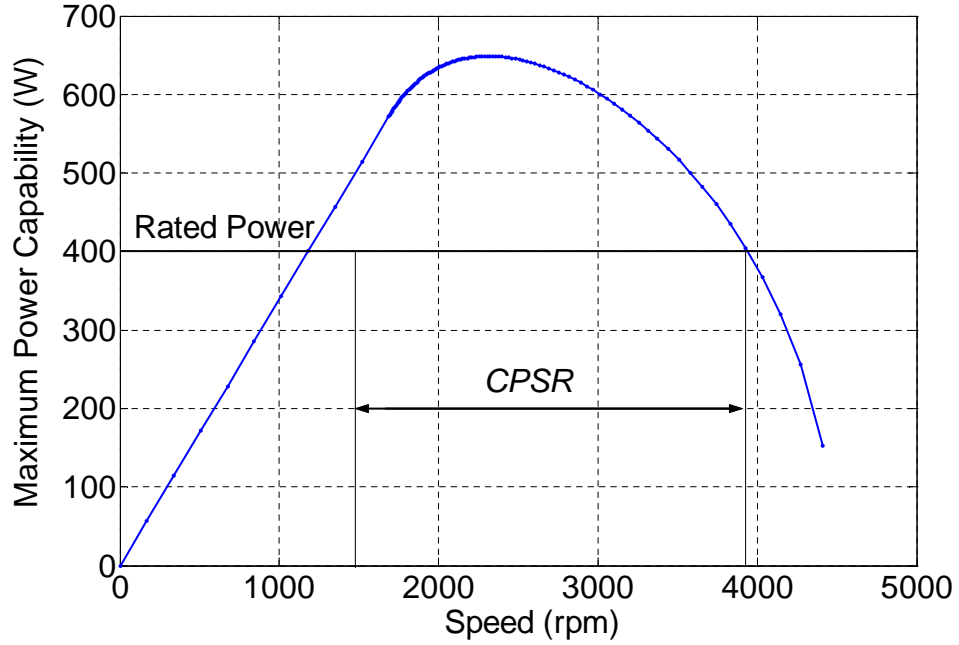


Figure 4.1: Determination of maximum power capability w.r.t to motor speed

$$Power = T_{\max} \cdot \omega_s \quad (4.7)$$

The maximum power capability profile (shown in Fig. 4.1) is a discrete curve with respect to motor speed (constant torque speed range and flux-weakening speed

range), which has no direct solution of constant power speed range (CPSR). Therefore, computer programming is used to obtain the CPSR by enumerative algorithm.

4.2.2 Description of genetic algorithms

The genetic algorithm is one of the most up-to-date artificial intelligence techniques. It is a search procedure emulating the mechanism of natural selection and natural genetics. When applied to motor design optimization, the GA explores the space of motor design variables and searches for the best motor design.

To apply the GA approach, a fitness function $F(\mathbf{X})$ has to be defined to evaluate how good each motor design is. This fitness function often coincides with the objective function. Strings of binary digits (representing sets of values of motor design variables) are manipulated by GA that measure the strength of each string by a fitness value given by the value of the fitness function. The fittest strings advance and mate with other strings to produce offsprings.

The main steps of GA optimization applied to the interior PMSM design are shown in Fig. 4.2 and are described as follow:

The first step is to define the fitness function or objective function as listed in (4.1). The maximum speed for rated power operation is derived from motor parameters and equations.

A population of N different motor designs is generated randomly. Each indi-

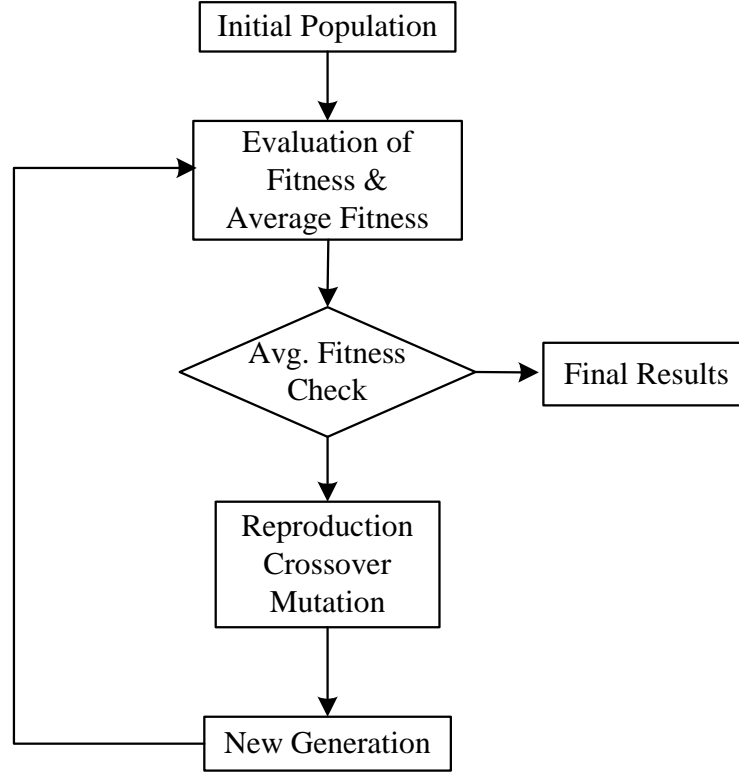


Figure 4.2: Main steps of genetic algorithms technique

vidual is characterized by a string of digits: zeros and ones. The string is composed of three substrings, each of them describing a design variable, which is coded in binary form using a binary substring $(a_{i,n-1}, a_{i,n-2}, \dots, a_{i,1}, a_{i,0})$, with $a_{i,j} \in \{0, 1\}$, related to the value of x_i by

$$x_i = x_{\text{imin}} + \frac{(x_{\text{imax}} - x_{\text{imin}})}{2^n - 1} \sum_{j=0}^{n-1} a_{i,j} 2^j \quad (4.8)$$

The length n of each substring depends on the desired resolution ν which results, $2^{-n} \leq \nu \leq 2^{-n+1}$.

As described in Chapter 3, the RSM model of motor parameters (λ_m , L_d and L_q) is validated in certain domain as listed in Table 4.1:

Table 4.1: The domain of design variables in the rotor structure

Design Variable	Min. value	Max. value
l_m (mm)	1.0	3.0
γ	0.5	0.75
α (degree)	50°	75°

There are many geometrical variables in the rotor design; optimization of all the variables is impractical and may not be necessary. In the Chapter 3, it has been shown through theoretical analysis that, if stator structure and winding are fixed, the motor parameters are determined only by the flux distribution in rotor core (3.18), (3.28). Using analytical model of electrical machines and finite element analysis, we have concluded that magnet thickness l_m , magnet angle α and magnet position in rotor γ are most significant factors, that affect the flux distribution in rotor core. Hence, only these three design parameters can be used for the optimization work.

The design space for design variables (l_m, γ, α) are limited by rotor geometry and mechanical constraints, which are determined by the power rating we choose to design; The modelling of motor parameters using RSM is based on such design constraints. When using GAs to search the optimal design, we have to make sure the search space does not exceed the design space. Therefore, the search domain using GA is kept same as the domain of design variables in Table. 4.1.

An example of an individual set of design variables is shown in Fig. 4.3, where the values of natural design variables (l_m, γ and α) are calculated by (4.8). Each

$x_1(l_m = 2.68mm)$						$x_2(\gamma = 0.64)$						$x_3(\alpha = 66.67^\circ)$					
1	1	0	1	1	0	1	0	0	1	0	0	1	0	1	0	1	0

Figure 4.3: Example of one individual of design variable

individual in the population is evaluated by (4.6) and (4.7). For this purpose, an analysis is carried out to predict their performance. The best fitness, $CPSR_{\max}$, is calculated. The average fitness $CPSR_{\text{avg}}$ of the population and the sum fitness of all individuals are found from:

$$\begin{aligned}
 CPSR_{\text{sum}} &= \sum_{i=1}^N CPSR(\mathbf{X}_i) \\
 CPSR_{\text{avg}} &= CPSR_{\text{sum}}/N
 \end{aligned} \tag{4.9}$$

At this stage, the rules of GA apply to reproduce a new population still of N individuals. The reproduction process is composed of the following three phases:

- **Selection:** Individuals of the old population (last population of motor designs) are selected and put in the new one, with preference given to the fittest. The selection is a stochastic sampling (by which the best individual is selected several times, while the worst one is excluded, according to a selection probability expressed as $p_i = CPSR(\mathbf{X}_i)/CPSR_{\text{sum}}$).
- **Crossover:** Two randomly selected strings, among those selected in the previous step, are mated. A position along one string is again randomly selected and all binary digits following this position are swapped with those of second string. The the two entirely new strings move on to the new generation. It is

worth noting that the crossover process elaborates the already existing values. This operation takes place with a defined probability p_c which statistically represents the number of individuals involved in the crossover process. Fig. 4.4a gives a schematic sample of crossover process.

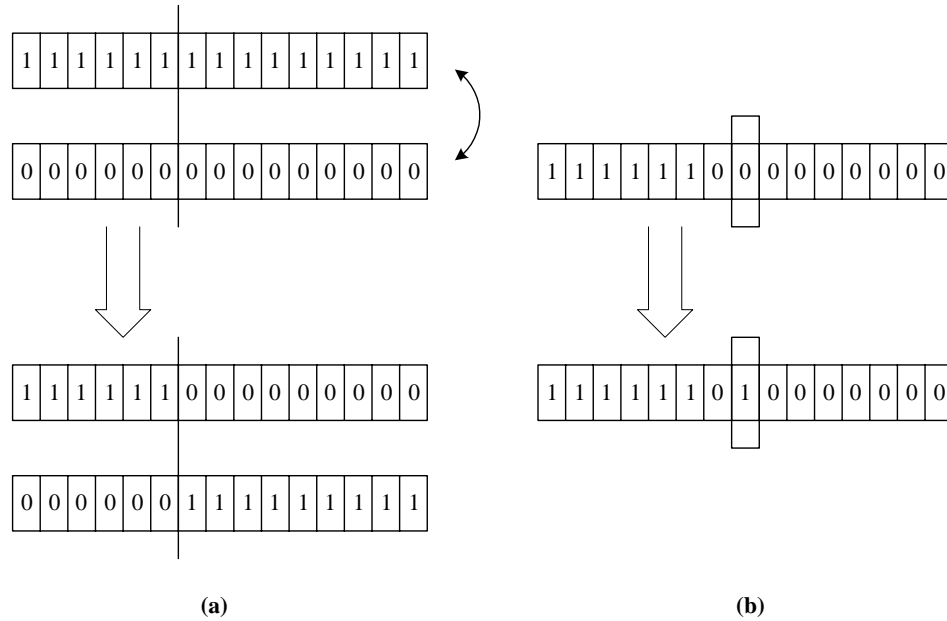


Figure 4.4: Schematic samples of crossover and mutation process

- **Mutation:** A bit of a string of the new population is randomly selected, according to a defined probability p_m , and its value is swapped from 1 to 0 or vice versa. This process explores new solution in the search space, to avoid any loss of useful genetic information. Fig. 4.4b shows a schematic sample of the mutation process.

At this point a new population is achieved; all individuals are evaluated, as described in step III, and the subsequent steps are repeated. The procedure is stopped after a prefixed number of generation N_g or when the best or the average

fitness values have reached a satisfied level.

4.3 Implementation of Proposed Design Optimization Procedure

To use the GA to search the optimal design of the rotor structure for the interior PMSM, each of the three design variables (l_m , γ , α) is coded into a 15 bit string segments using binary coding as described in (4.8). The first population is generated by selecting randomly each bit of the strings. The fitted second-order RSM models are used to determine the motor parameters (λ_m , L_d , L_q) according to the input design variables. These motor parameters together with the voltage and current constraints (4.2) are used to evaluate the final objective function $CPSR$ (4.1). The FEM is applied to verify the final design results. The whole flowchart for the proposed design optimization procedure is shown in Fig. 4.5.

4.4 Numerical Results and Discussions

The GA combined with RSM has been applied to the design optimization of an interior type PMSM with a rated power rating of 400 W. The GA technique has been tested by computer simulations. The size of the population greatly affects the quality of the result and the computation time. In addition, different choices of crossover probability p_c and mutation probability p_m have been compared. It is worth noting that the crossover operator searches in new parts of the variables domain, a low p_c causes a contracted search that can be ineffective. The mutation

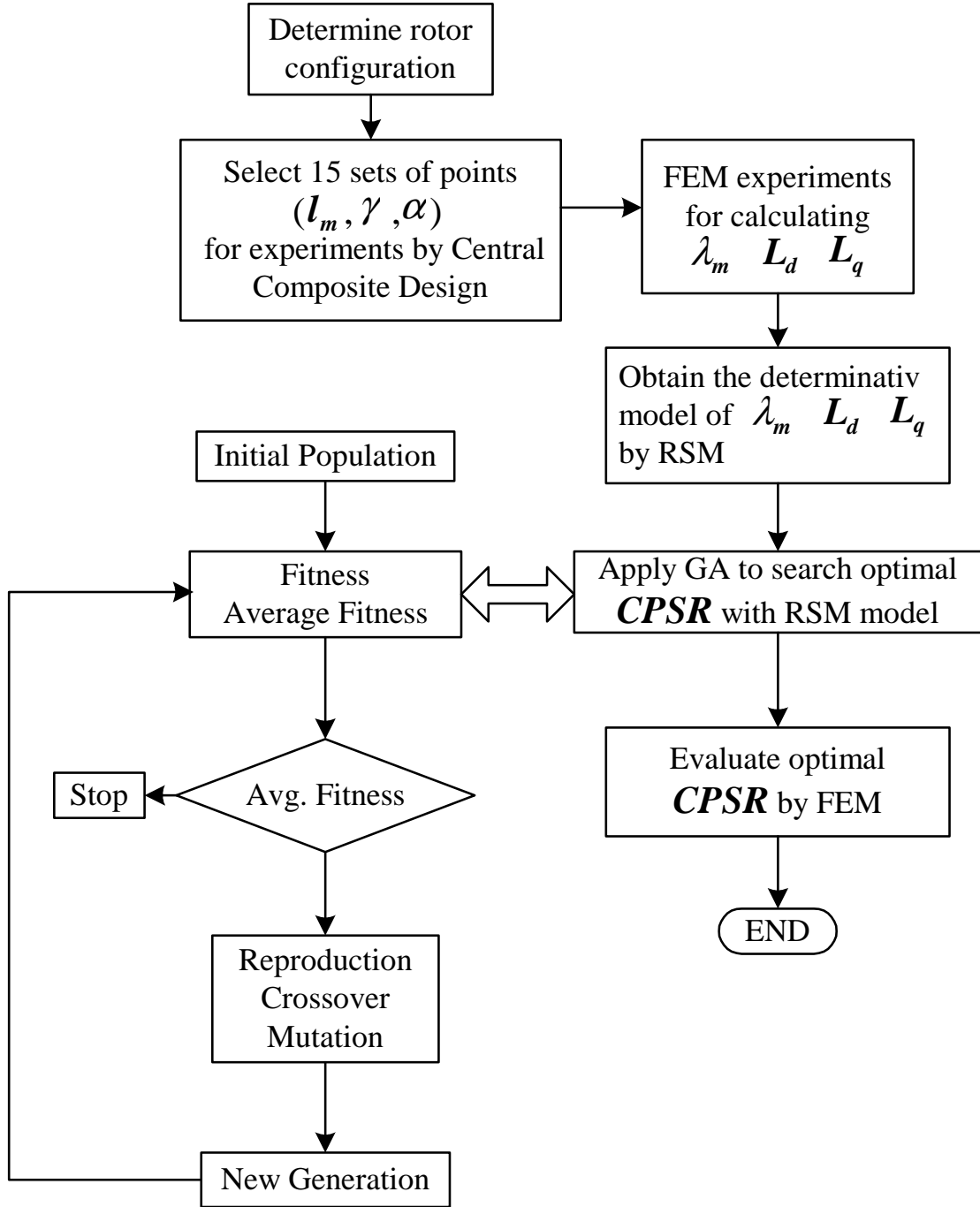


Figure 4.5: Flowchart for the proposed design optimization of the interior PMSM operator explores new points out the solution space and a high p_m produces many mutated strings in the new population which can alter the selection process of the algorithm. Therefore, good GA performance requires the choice of a high p_c , a low

p_m (inversely proportional to the population size), and a moderate population size. Following these instructions the following parameters have been adopted for the computer simulation.

$$\begin{aligned} p_m &= 0.02 \\ p_c &= 0.6 \\ \text{popsize} &= 60 \end{aligned} \tag{4.10}$$

For all the simulations, 30 generations have been considered. With this value a good convergence has been obtained. The values of the maximum and average CPSR for every generation are plotted in Fig. 4.6. The preferred solution is first achieved at the 25th generation. The data of the best observed motor design are reported in Table 4.2.

It has to be pointed out that this solution is near optimal but may not be the true optimal because not all domains of design variables have been explored. The fact is that GAs have no convergence guarantees in arbitrary problems. But they do sort out interesting areas of a space quickly and provide solution close to the global optimal.

The FEM is applied to verify the optimized results with the preferred design values of rotor geometry. Table 4.3 indicates the validity of the proposed approach: the motor parameters approximated by the RSM in the GA optimization process are in good agreement with those recalculated by the FEM with 5% error.

Fig. 4.7 illustrates the d- and q-axis inductance variations with the armature

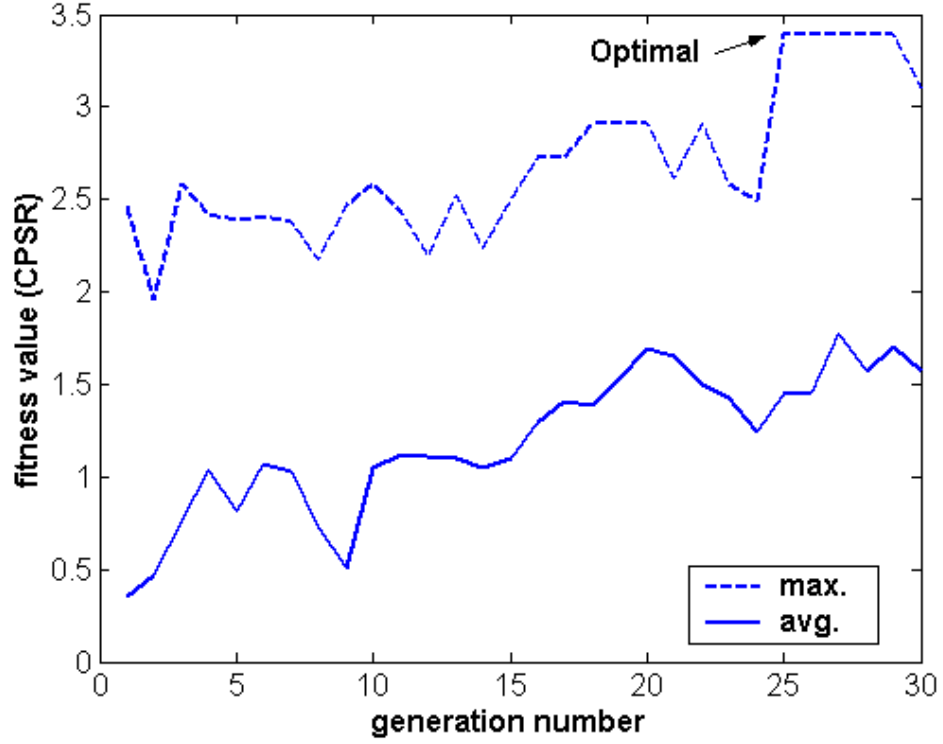


Figure 4.6: Average and maximum CPSR trend combining GA and RSM

Table 4.2: Optimized design values and motor parameters

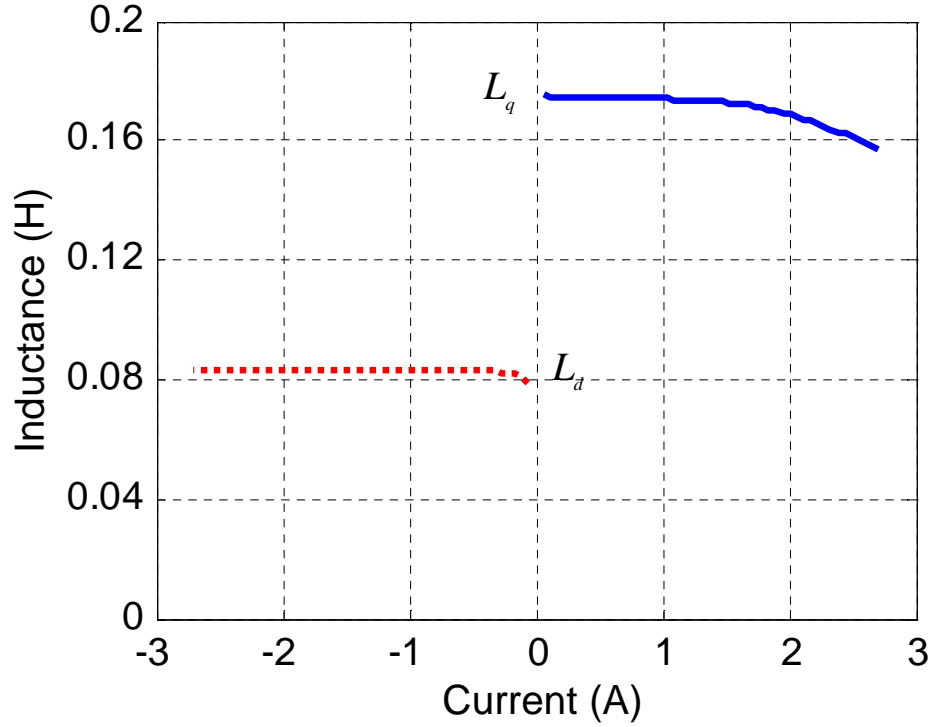
parameter	value
l_m	1.0(mm)
γ	0.67
α	75 degree
λ_m	0.323 Wb
L_d	0.081 H
L_q	0.170 H
$CPSR$	3.45

current by FEM computation. There is a fall in L_q with increasing q-axis current, as the q-axis magnetic circuit is saturated due to small air gap, while d-axis current has little effect on the L_d . It is noted that, during normal motoring operation, the

Table 4.3: Comparison of motor parameters with GA+RSM and FEM

parameter	GA+RSM	FEM
$\lambda_m(Wb)$	0.323	0.312
$L_d(H)$	0.081	0.085
$L_q(H)$	0.170	0.165

q-axis current is usually less or equal than the rated current (2A). Therefore, it is reasonable to use constant L_q to estimate the motor performance in the proposed approach.

Figure 4.7: Effects of magnetic saturation on L_d and L_q

The flux distributions in the stator and air gap for the final prototype machine design have been evaluated from the FEM analysis (Flux2D). Fig. 4.9 shows the flux density in the air gap at maximum flux-weakening condition. The corre-

sponding flux density in the air gap with open circuit condition is given in Fig. 4.8. From the numerical analysis listed in Table. 4.4, it is obvious that the flux in the air gap is seriously weakened by the armature reaction.

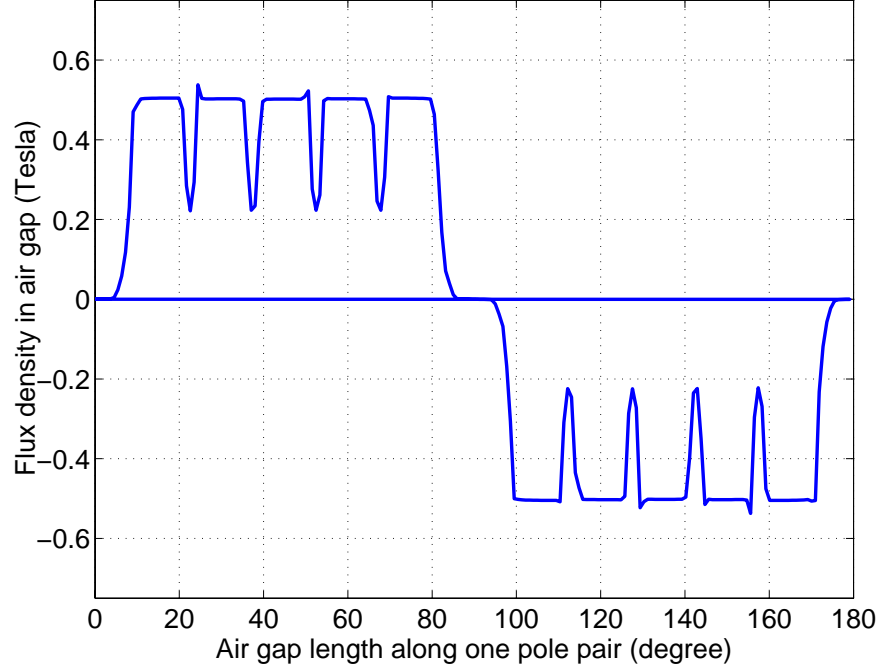


Figure 4.8: Permanent magnet excited flux distribution in the air gap

Table 4.4: Comparison of flux distribution for open circuit and flux-weakening condition

B_g	Open Circuit	Flux-weakening
Fundamental value	0.564 T	0.209 T
Total R.M.S value	0.632 T	0.298 T

It is difficult to verify the final objective quantity value of $CPSR$ directly by FEM because of the coupling of the motor and the inverter system. Alternatively, torque and stator flux linkage versus current angle β characteristics calculated by FEM can provide the information of power capability in a wide speed range, Fig. 4.12 and Fig. 4.13 . The current angle β is defined as the angle of stator current

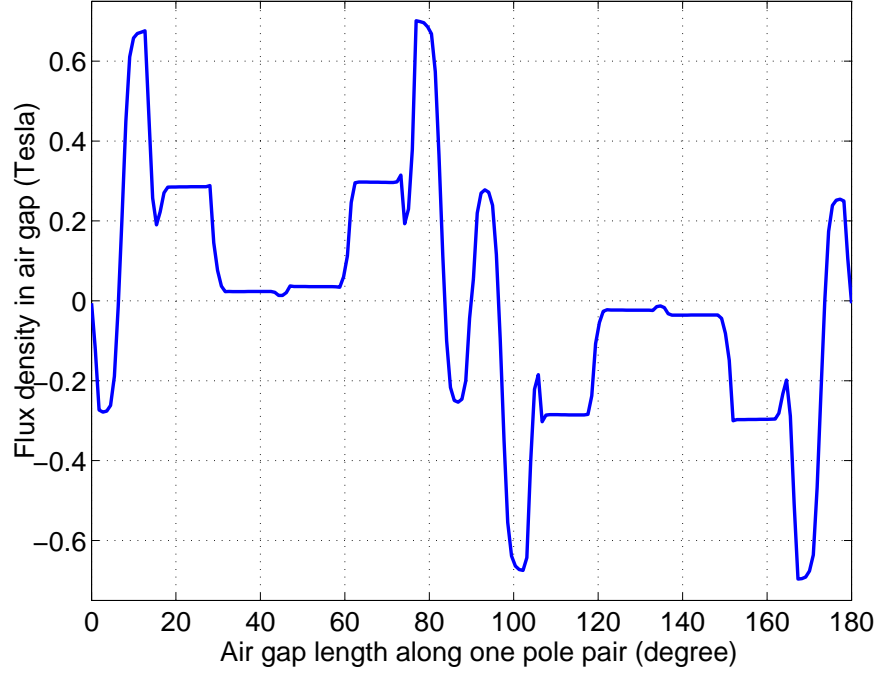


Figure 4.9: Air gap flux density curve with maximum flux-weakening condition $\beta = 180$ degree

vector and the d-axis, as shown in Fig. 4.10. Since $\lambda_m > L_d I_{sm}$ in the optimized design, as introduced in Fig. 4.11 in Chapter 2, the maximum output torque under different speed range is produced in Regions I and II only when current vector (I_d, I_q) is moving from point A ($\beta = \arctan(I_{dm}/I_{qm})$) to point M ($\beta = 180^\circ$).

With the computation results by FEM and equation (4.6), the steady state output power capability vs speed characteristics for the optimized rotor design are shown in Fig. 4.14. The power vs. speed characteristics as well as the torque vs. current angle characteristics further confirm that the estimated results by the proposed RSM+GA approach is close to the field computation results by FEM. The small discrepancy can be explained by the error of fitted RSM model and effects of magnetic saturation.

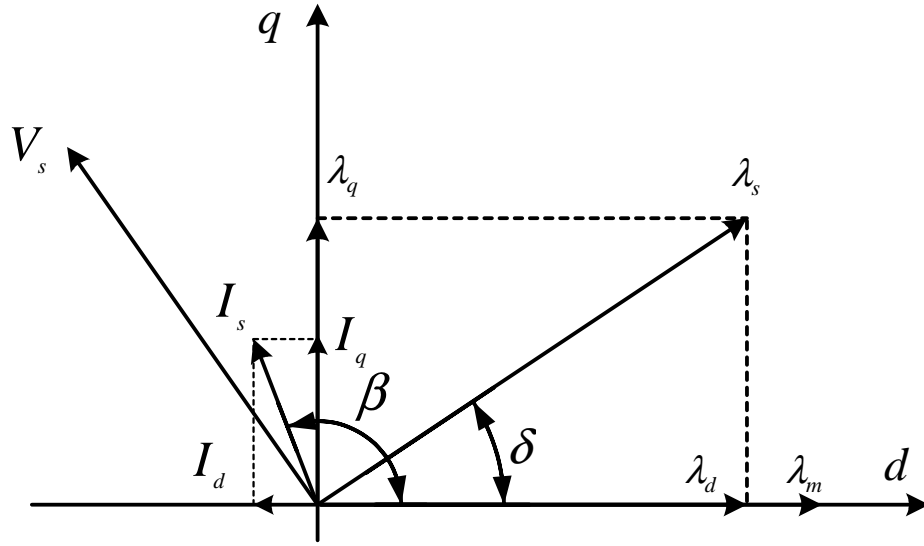


Figure 4.10: The stator flux linkage in the dq reference frame

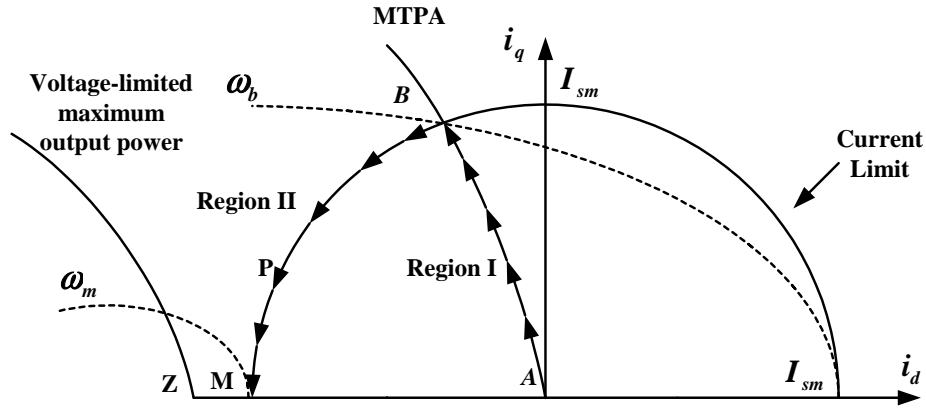


Figure 4.11: The optimum current vector trajectory in the d - q coordinate plane for $\lambda_m > L_d I_{sm}$

In order to verify the design solution by the proposed numerical optimization procedure is the optimal design in the available variable space. The constant power speed range for 9 design cases including the optimal solution are selected and compared by FEM computation.

The rotor design variables for the 9 design cases are evenly distributed in the available geometrical space. The calculated motor parameters (L_d , L_q and λ_{pm})

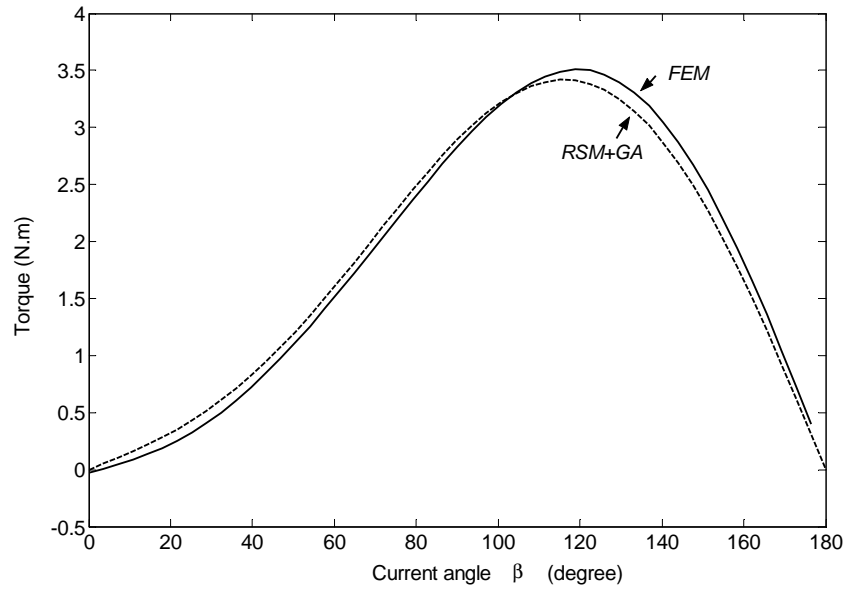


Figure 4.12: Torque vs. current angle β characteristics for FEM and RSM

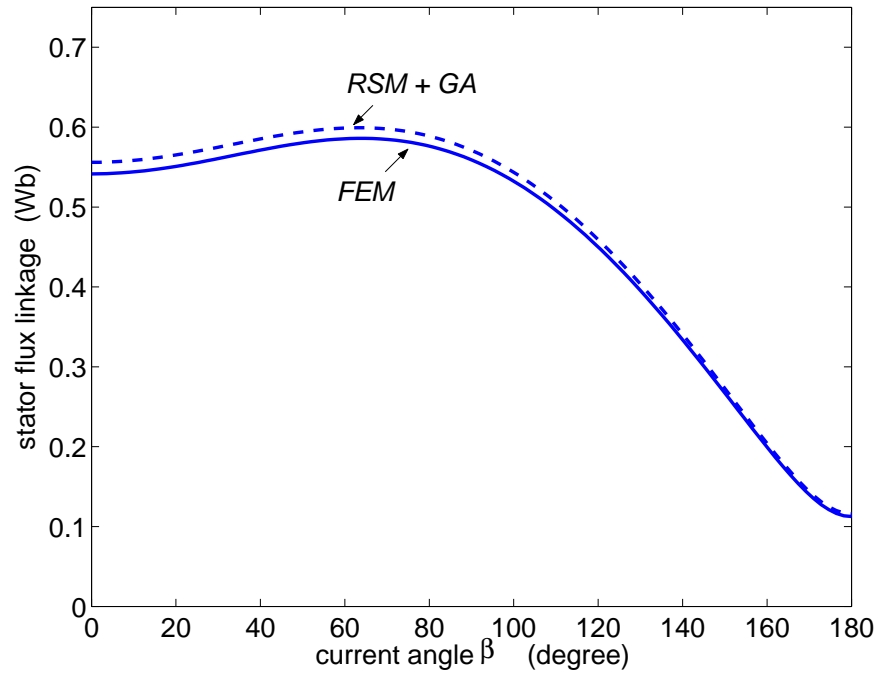


Figure 4.13: Stator flux vs. current angle β characteristics for FEM and RSM

for the selected 9 design cases are listed in Table 4.5.

Fig. 4.15 shows the maximum power capability for 9 selected design cases. It illustrates that the different design of rotor structures will produce different con-

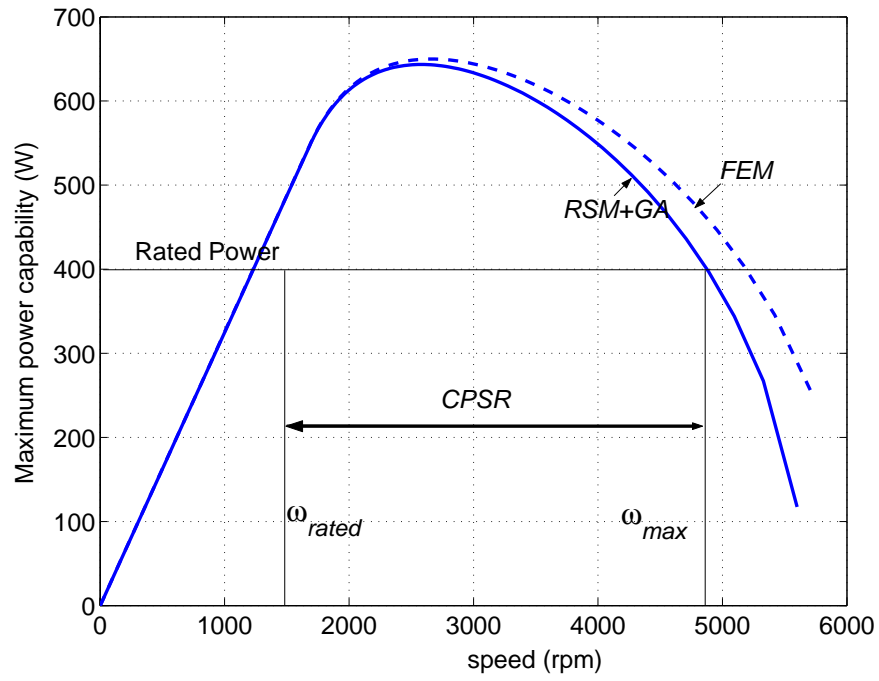


Figure 4.14: Power capability vs speed characteristics for the optimized design by FEM and RSM

Table 4.5: Comparison of 9 design cases

Case	l_m (mm)	γ	α (Degree)	L_d (H)	L_q (H)	λ_{pm} (Wb)	$CPSR$
A	1	0.67	75	0.081	0.170	0.323	3.45
B	2	0.67	75	0.065	0.158	0.394	1.81
C	3	0.67	75	0.054	0.149	0.426	1.43
D	1	0.75	75	0.081	0.158	0.407	1.96
E	2	0.75	75	0.057	0.142	0.453	1.34
F	3	0.75	75	0.045	0.126	0.473	1.20
G	2	0.75	60	0.065	0.159	0.339	2.73
H	3	0.75	60	0.057	0.158	0.371	1.98
J	2	0.70	70	0.063	0.158	0.383	1.96

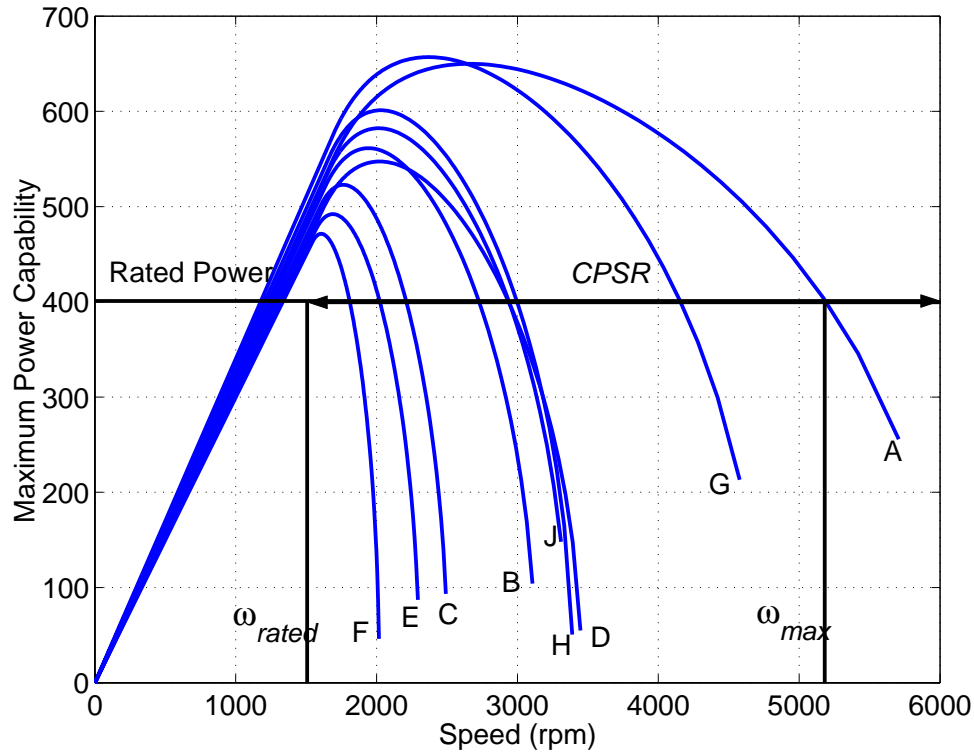


Figure 4.15: Comparison of optimal design with other design cases

stant speed range. The optimal solution (Case A) by RSM together GAs method has the largest *CPSR* (3.45), which validate the proposed numerical optimization approach.

4.5 Conclusion

In this chapter, the effect of geometric parameters on the constant power operation of interior PMSMs has been investigated using both analytical method and finite element method. In order to design an interior PMSM with an optimal constant power speed range, an efficient design optimization approach is proposed and implemented. The combination of Response Surface Methodology, Genetic Algorithm and Finite Element Analysis has proved an effective and practical tool for numer-

ical simulation and optimization process. This approach enables a fast design and an accurate performance prediction as demonstrated by comparing the numerical results obtained from this new method and conventional methods. The design optimization methodology was illustrated by a design example for the prototype interior PMSM.

Chapter 5

Tests and Performance of the Prototype Interior PMSM

5.1 Introduction

The prototype interior PMSM was tested using a motor-generator set. The test equipment included a 750W/5A/350V IGBT PWM voltage source inverter, the prototype interior PMSM, a torque transducer, a 1.1kW separately excited dc generator and a resistor bank to provide a load on the generator, as shown schematically in Fig. 5.1. The digital signal processor (DSP) control board and an integrated interface platform to provide interface between the digital and analog systems. The inverter and the control system adjusted the speed, current and torque angle of the drive system according to a command. The field excitation and load resistor of the dc generator were adjusted to vary the mechanical loading of the PMSM.

A range of tests were conducted on the prototype PMSM. These tests served three purposes:

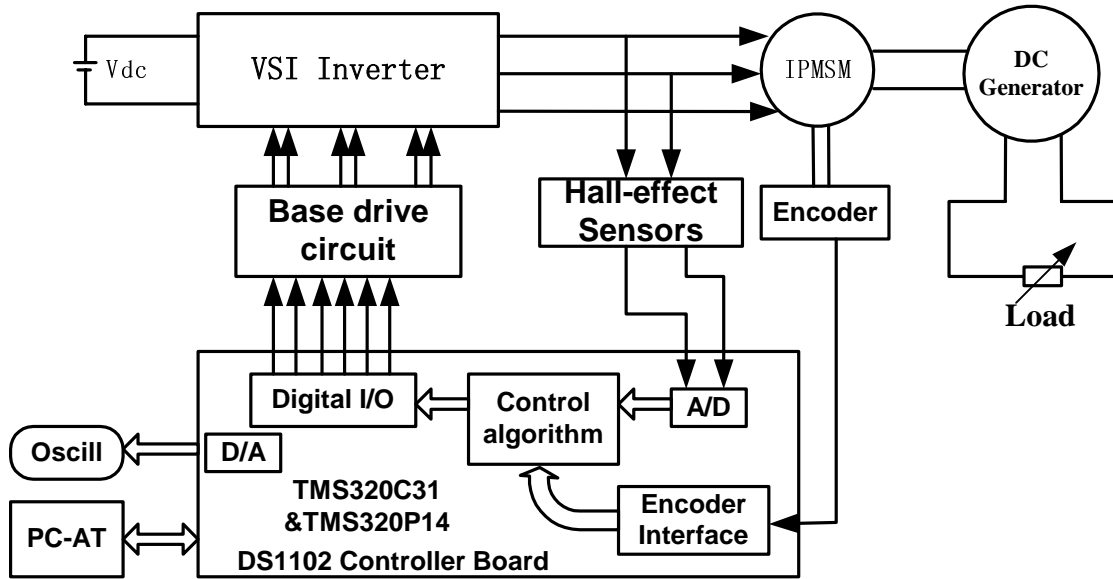


Figure 5.1: Hardware schematic of the interior PMSM drive system

- To determine the motor parameters for the prototype interior PMSM, including the stator PM flux linkage λ_m , d-axis inductance L_d and q-axis inductance L_q .
- To obtain the steady state performance of the interior PMSM, including the constant power speed range, the efficiency and power factor over the wide speed operation.
- To evaluate the performance of the prototype interior PMSM for different inverter DC link voltage level.

5.2 The Prototype Interior PMSM

Fig. 5.2 shows the drawing and dimensions of rotor structure for the 400 W interior PMSM based on the optimized design results. 4 NdFeB magnet blocks were inserted

in rotor slots. The stator frame is same with the standard induction motor and the winding is rewound according to the design specifications (see Appendix A for detail). The actual structures of the stator and rotor are shown in Fig. 5.3.

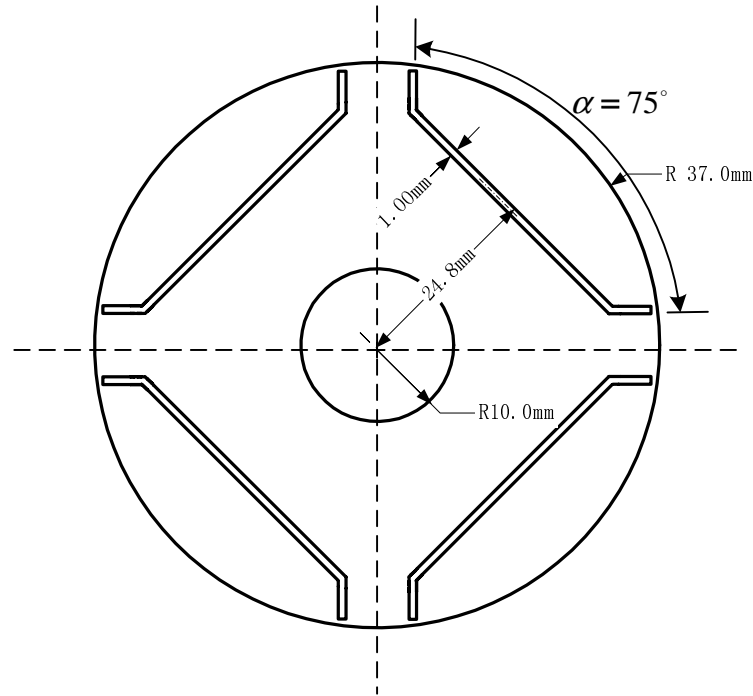


Figure 5.2: The optimized rotor structure for the prototype interior PMSM

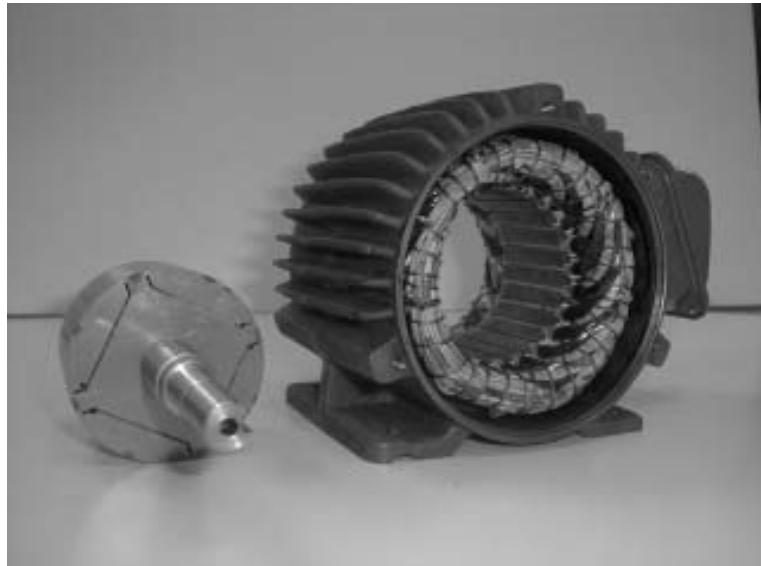


Figure 5.3: Standard stator and designed rotor for the prototype interior PMSM

Tests were conducted on the prototype interior PMSM in order to evaluate its performance, to verify the proposed optimization approach and to validate the design.

5.3 Experimental Interior PMSM Drive System

An experimental set-up for the interior PMSM drive system has been built with the dSPACE DS1102 controller board. An experimental set-up for the drive system is shown in Fig. 5.4 and Fig. 5.5.

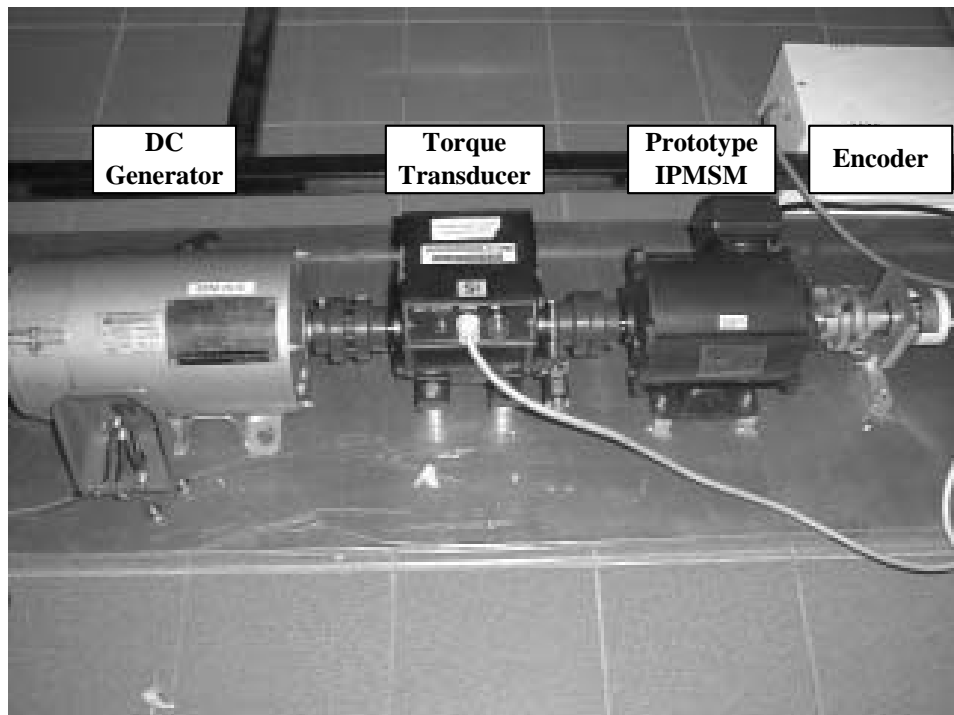


Figure 5.4: Experimental set-up for the interior PMSM drive system

As shown in these figures, the experimental system consists of the following units:

- A PC for software programming, debugging and real-time control.

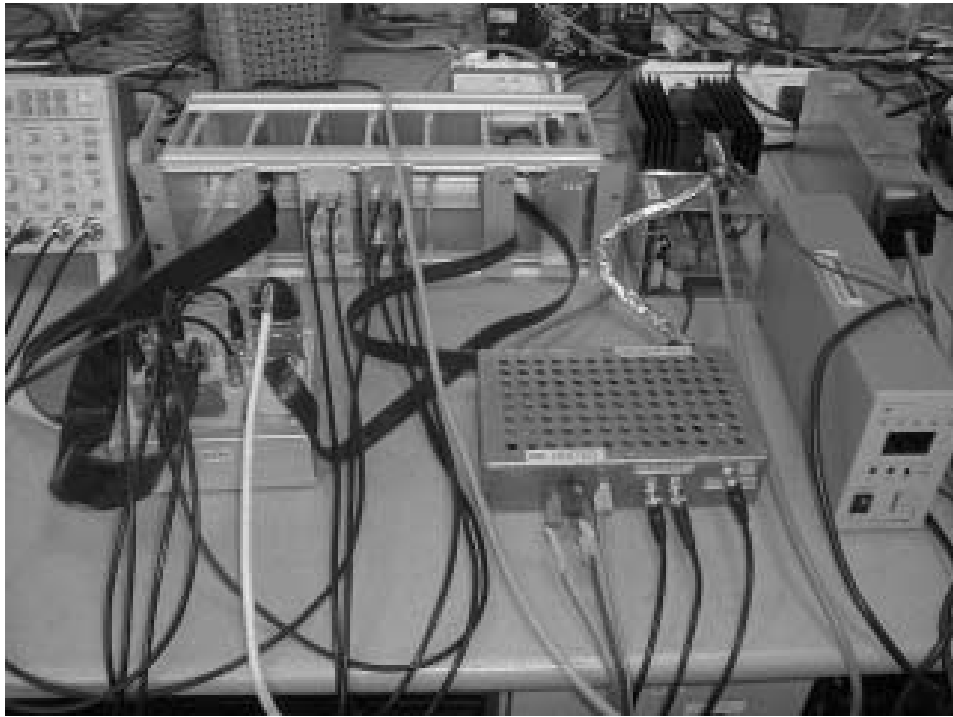


Figure 5.5: dSPACE DS1102 based integrated PMSM drive test platform

- A dSPACE DS1102 controller board for executing control programs, generating control signals, performing A/D and D/A conversions, and communicating with the PC.
- A PWM voltage-source inverter for driving the interior PMSM.
- An integrated interface platform for performing logic operations, inverter control, buffering, isolation, protection, etc.
- The prototype interior PMSM with exterior incremental encoder for position sensing.
- Two current sensors for measuring the phase currents in two motor phases and voltage sensor for measuring the DC link voltage.
- A loading system for producing load torque to the interior PMSM.

- A torque transducer for measuring the actual motor torque.

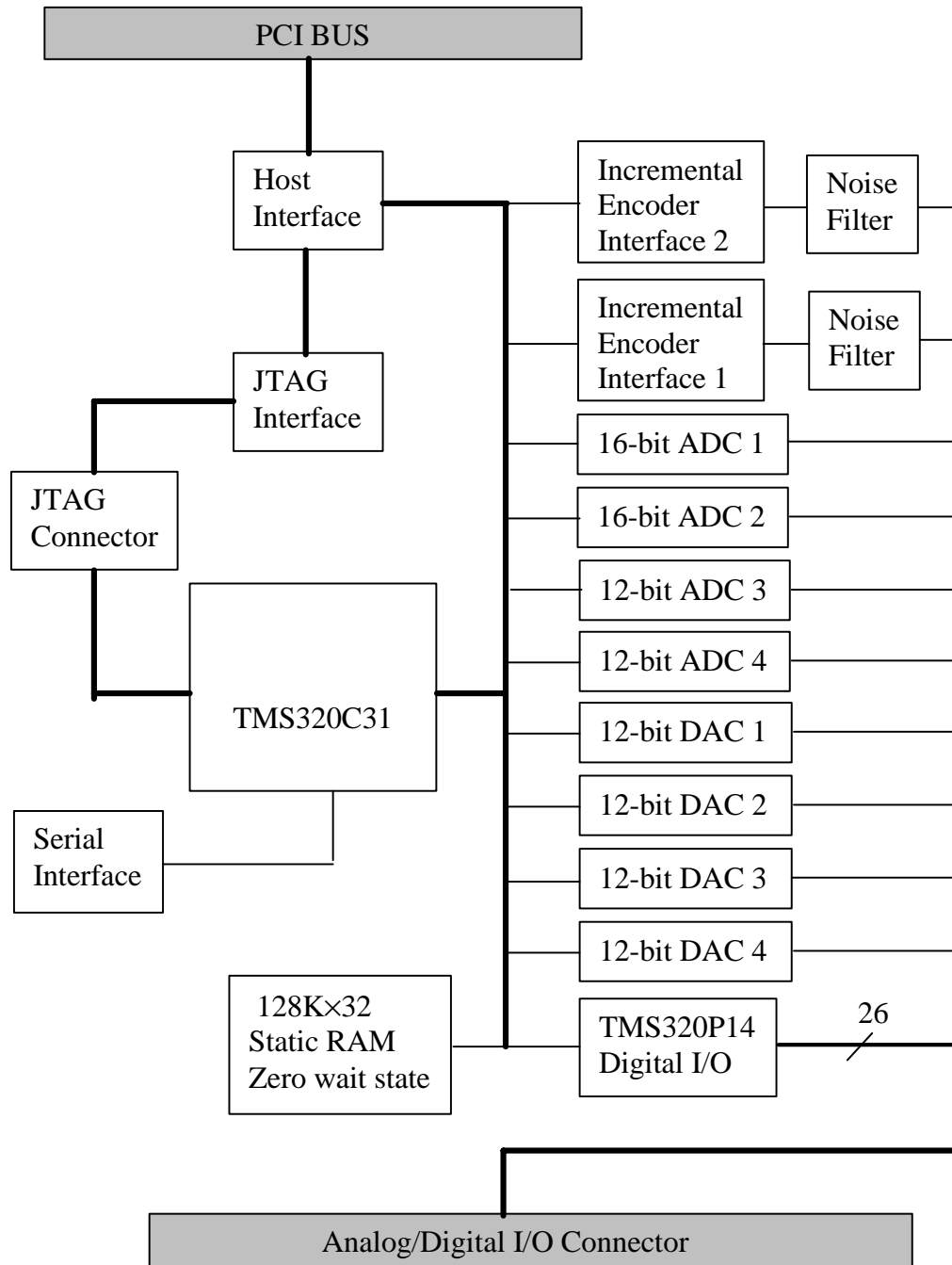


Figure 5.6: Configuration of the controller board used for hardware implementation

5.3.1 DS1102 controller board

The dSPACE DS1102 controller board is specifically designed for the development of high-speed multi variable digital controllers and real-time simulations in various fields such as motor drives. The board consists of a floating-point DSP TMS320C31, a micro controller TMS320P14 acting as a slave-DSP for the digital I/O subsystem, A/D and D/A converters, and encoder interfaces.

The main DSP processes the numerically intensive algorithms at a speed of 60 MHz per instruction cycle. The slave-DSP performs digital I/O and PWM generation. The A/D converters convert the analog feedback signals of $\pm 10V$ into digital format so that the DSP can read in the measured quantity. Such conversions are used on the measured stator current or motor torque feedback signals. Conversely, the D/A converters convert the digital signals in the DSP into analog signals of $\pm 10V$ so that they can be displayed on an analog CRO. The encoder interface provides the interfacing of the DSP with the incremental encoder so that the output of the incremental encoder, which is in discrete pulses, can be quantized into digital form; hence, the data on the rotor-position is acquired. The DS1102 controller board is designed like a PC expansion card so that it can be inserted into the PCI slot of the PC, together with the PC video card or sound card. Using the appropriate software for communication between the PC and the DSP, users can debug the user-program that is loaded in the DSP (via C-programming and the Texas Instruments C-Compiler), tune the experimental parameters on-line or display the experimental variables in real-time.

5.3.2 PWM voltage source inverter

A 3-phase, 750 W PWM inverter is used as the power circuit for driving the PMSM. The inverter used is called PowIRTrain (from International Rectifier), which combines all the power conversion and power control devices and circuitry that are required for building state-of-the-art AC drives into modules or assemblies. The PowIRTrain inverter consists of a 3-phase input rectifier, a 3-phase IGBT inverter with a braking switch, gate drive, power terminations, DC link capacitor with soft charge scheme, surge suppression, current/voltage/temperature sensing with associated protection circuits, system power supply and control interface. The PWM inverter of model IRPT2062C is used in the hardware implementation of the PMSM drive.

5.3.3 Integrated interface platform

In the implementation of the experimental PMSM drive set-up, it is necessary to provide a hardware interface between the motor drive and DSP-DS1102. The hardware interface has the following functions:

- Generating mid-symmetrical PWM signals using EX-OR gates.
- Generating six PWM signals that controls the six switches of the PWM inverter.
- Incorporating dead-time in the PWM signals.

- Setting the over-current/over-voltage protections and RESET/STOP functions of the inverter.
- Buffering the pulse signals generated from the incremental encoder.
- Provide filtering of the measured current and torque signals.

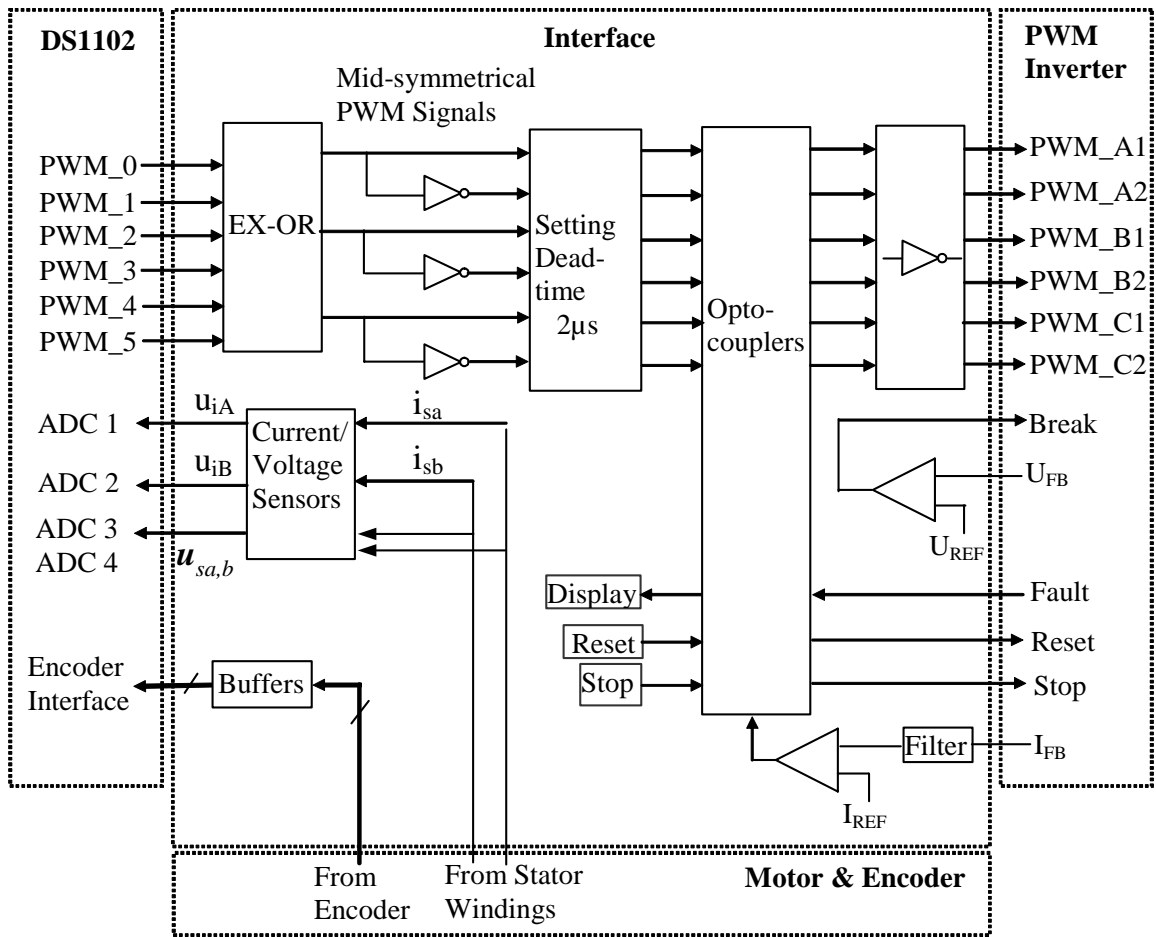


Figure 5.7: Interfacing the controller board with the control circuit

The block diagram of the peripheral interface circuit is shown in Fig. 5.7. Signals of the six PWM channels, which are ch0 and ch1 for phase A, ch2 and ch3 for phase B, and ch4 and ch5 for phase C, are EX-ORed and become three mid-symmetrical PWM signals. Another three complementary signals are obtained

from three logic inverters. Proper "dead time" is then incorporated into these six PWM signals to avoid "mutual-ON" of the upper and lower switches on the same phase of the inverter. The opto-couplers transfer the six PWM signals and isolate the low-side circuit from the high-side circuit. The six PWM signals are inverted into "low-active" signals as required by the inverter and then sent to the inverter. Signals of "Reset" and "Stop" are also sent through opto-couplers to control the inverter. Voltage comparators are used to detect over voltage and over current. "Fault" signals generated by the inverter and the voltage comparators are sent through opto-couplers to the low-side circuit to inhibit the transfer of the PWM signals. The installed current sensors and resistors convert the current signals into voltage signals for the use of A/D converters of DS1102. Signals from the incremental encoder are sent through buffers to shape the waveforms and to drive the encoder interface circuit of ds1102.

5.3.4 Current sensor

Sufficiently accurate measurements of the motor phase currents are essential to ensure high-performance in the PMSM drive system. In the experimental set-up, two current sensors are utilized to measure the phase-a and b currents. The measured currents are converted into voltage signals scaled to the range $\pm 10V$ by using resistors of appropriate resistances. These voltage signals are then fed into the A/D converters of the DS1102. In the PMSM experimental set-up, the LEM module LA 25-NP current sensors are used. The current sensors, resistors and the

power supply for the current sensor are included on the current sensor board.

5.3.5 Loading system

The PMSM drive loading system consists of a DC motor, an externally connected variable resistor R_{load} in series with the armature side of the DC motor which carries an armature current I_a and a DC power supply. Fig. 5.8 shows the configuration for the loading system.

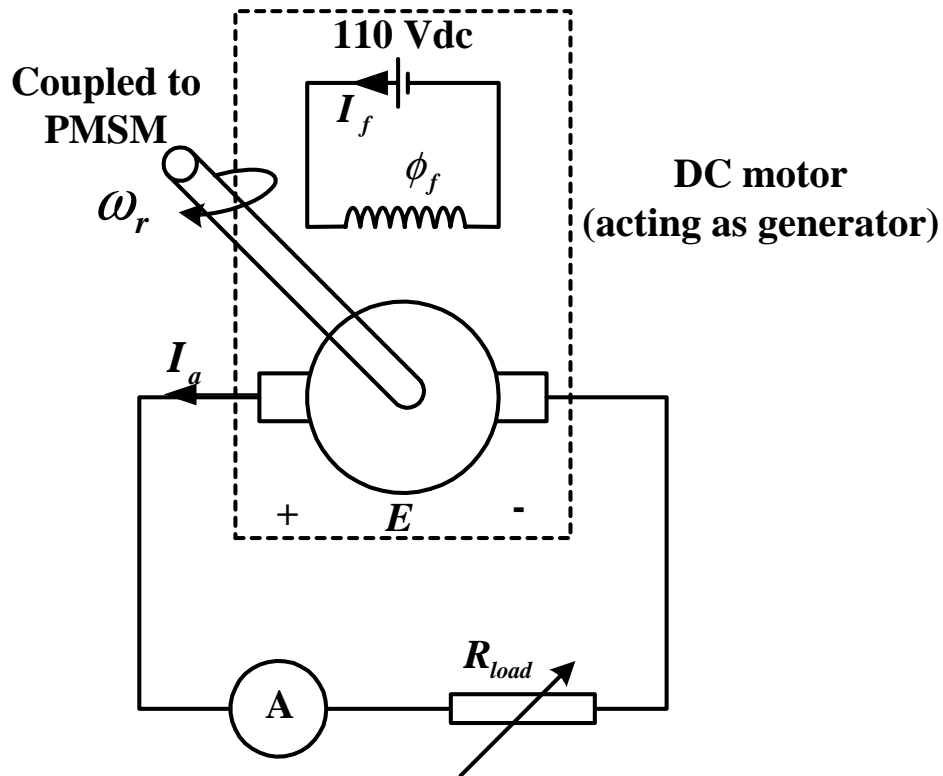


Figure 5.8: Configuration for the interior PMSM loading system

5.4 Experimental Determination of Motor Parameters

The performance of constant power operation for the interior PMSM depends on the motor parameters as introduced in Chapter 2. Hence, the accurate measurement of motor parameters is necessary to improve the control performance of the interior PMSM drives. In this section, an open circuit test and modified load test are conducted to measure the stator PM flux linkage λ_m , d-axis inductance L_d and q-axis inductance L_q .

5.4.1 Permanent magnet flux linkage λ_m

The flux due to the permanent magnets is considered to be constant. If the stator currents are zero ($I_d = I_q = 0$), (2.12) becomes

$$\begin{aligned} V_d &= 0 \\ V_q &= \omega_s \lambda_m \end{aligned} \tag{5.1}$$

The voltage at the fundamental frequency can be calculated by

$$V_s = \sqrt{V_d^2 + V_q^2} = \omega_s \lambda_m \tag{5.2}$$

Therefore, λ_m can be estimated dividing the fundamental voltage by the electrical angular frequency

$$\lambda_m = \frac{V_s}{\omega_s} \tag{5.3}$$

Running the DC motor to rotate the prototype interior PMSM and using volt-meter to measure the open circuit back EMF between any two phase (line voltage), we

get following results as listed in Table 5.1.

Table 5.1: Experimental measurements of back EMF and calculated values of λ_m

speed (rpm)	line back EMF in rms (V)	$\lambda_m(Wb)$
600	45.6	0.296
900	68.7	0.298
1200	91.4	0.297
1500	114.1	0.297
average		0.297

5.4.2 Torque angle measurement

The torque angle of a synchronous machine is defined as the angular displacement between the magnet excitation voltage E_0 and the terminal voltage V_s , as shown in Fig. 5.9.

The magnet excitation voltage E_0 and terminal phase voltage V_s can not be measured at the same time. An alternative procedure depends on the position measurement by incremental encoder. We can find out the position of d-axis of the rotor with respect to phase A axis. The procedure is described in the following steps:

- I.** The increment encoder was installed on the prototype motor shaft. The index channel signal of incremental encoder is sent to the digital oscilloscope. We take phase A voltage as the reference signal for the same digital oscilloscope.
- II.** Running the DC motor to drive the prototype motor at no-load. Then two

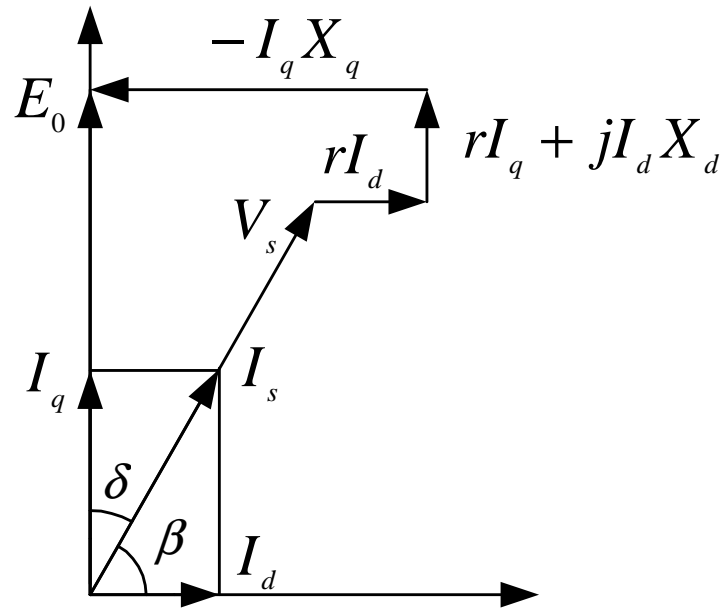


Figure 5.9: PMSM generator phasor diagram for testing

waveforms will be displayed on the screen of digital oscilloscope as shown in Fig.

5.10:

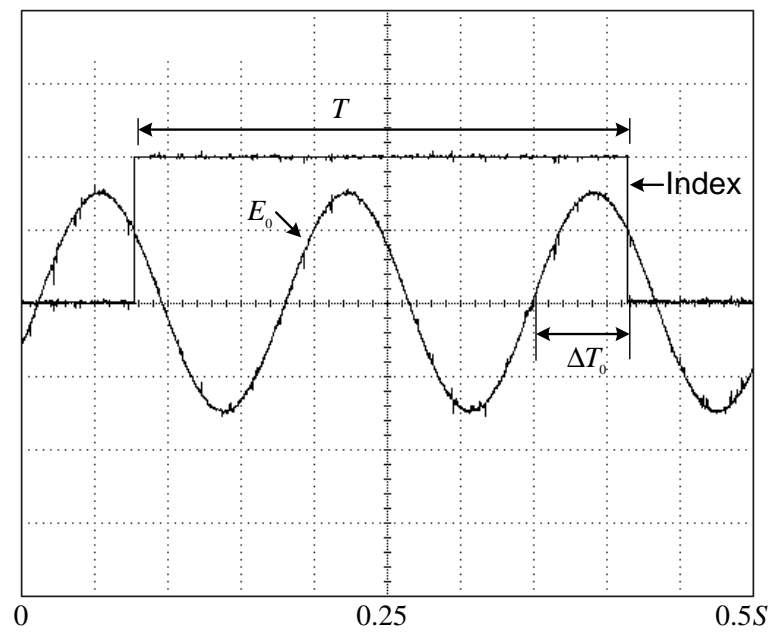


Figure 5.10: Experimental measurement of d-axis position

The sinusoidal waveform represents the magnet excitation voltage E_0 . The

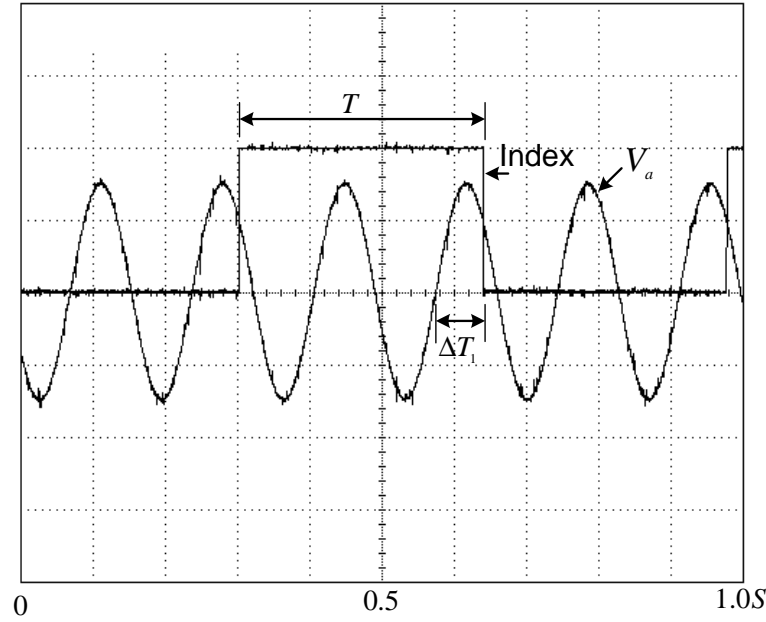


Figure 5.11: Experimental measurement of load angle

flip-flop instant of the square waveform represents index signal. Since the zero crossing of the E_0 indicates the position of d-axis axis and the index signal comes from the incremental encoder fixed with the rotor shaft, we can measure the time displacement ΔT_0 to know the relative position (θ_0) between d-axis and index position as:

$$\theta_0 = \frac{\Delta T_0}{T} \times 2\pi = \frac{\Delta T_1}{T} \times 2\pi \quad (5.4)$$

III. Run the prototype motor as a generator and connect to the adjustable resistant bank for the load test. It is important to keep the rotor speed the same as (II). We obtain the terminal phase A voltage and index signal through the digital oscilloscope as shown in Fig. 5.11. Repeat the procedure in (II) again to measure the time displacement ΔT_1 between two waveforms. Hence, the torque angle will be calculated as:

$$\delta = \frac{\Delta T_0 - \Delta T_1}{T} \times 2\pi \quad (5.5)$$

5.4.3 Load test to measure L_d and L_q

In the load test, the prototype interior PMSM is rotated by DC motor as a PMSM generator, and the motor terminals are connected with the three phase resistor bank which acting as an adjusted resistive load. In this measurement, it is not possible to isolate the stator leakage reactance from the total d-axis and q-axis reactance. It is common practice to lump the leakage inductance into the synchronous reactance, which leads to the modified phasor diagram as shown in Fig. 5.9.

From the phasor diagram, the following can be obtained as

$$\begin{aligned} V_s \sin \delta &= X_q I_q - r I_d \\ V_s \cos \delta &= E_0 - X_d I_d - r I_q \end{aligned} \quad (5.6)$$

where r is phase resistance which is assumed a constant dc value and $E_0 = \lambda_m \omega_s$.

It is noted that once the data of output voltage V_s , current I_s , and torque angle δ are known from the load test, other quantities in (5.6) can be obtained as

$$\begin{aligned} X_d &= \frac{E_0 - r I_s \cos \delta - V_s \cos \delta}{I \sin \delta} \\ X_q &= \frac{V_s \sin \delta + r I_s \sin \delta}{I \cos \delta} \end{aligned} \quad (5.7)$$

and

$$\begin{aligned} L_d &= \frac{X_d}{\omega_s} \\ L_q &= \frac{X_q}{\omega_s} \end{aligned} \quad (5.8)$$

Table 5.2 lists the experimental results of load test for different speeds and loading conditions. The values of L_d in the IPM motor are affected at light load, and these are not affected significantly at high values of load.

Table 5.2: Experimental measurements of L_d and L_q

speed (rpm)	V_s (V)	I_s (A)	δ (degree)	L_d (H)	L_q (H)
600	23.84	0.493	20.2	0.074	0.156
1200	49.42	0.616	25.2	0.079	0.160
1500	64.09	0.269	13.5	0.113	0.186
1500	62.76	0.525	22.5	0.086	0.164
1500	51.04	1.476	53.1	0.083	0.168
1500	48.27	1.588	58.5	0.086	0.184

In Table 5.1 and 5.2 the measured motor parameters (λ_m , L_d and L_q) for the prototype motor through experiments show significant variation and discrepancy with those expected by RSM+GA method. The major reasons for such difference are listed as follows:

(1) The material characteristics used in FEM and RSM are slightly different with those actually used in the fabrication of prototype motors. For example, the measured remanence flux of permanent magnet was found to be less than the value given by the manufacturing data sheet. This explains why λ_m is less than the expected value.

(2) In the proposed design methodology, the unsaturated linear model are

used to estimate the motor parameters. However, the key machine parameters are non-linear functions of design variables and the load condition. Therefore, the performance of the machine is a non-linear function of these parameters. This is another reason why measured performance of the prototype is below the design values.

The major reason for this discrepancy seems to be the use of unsaturated model. Hence a saturated model of motor parameters will give better estimate the machine performance under saturation effect.

5.5 Experimental Evaluation of Wide Speed Operation Performance

Tests have been conducted to evaluate the machine operation performance in a wide speed range. The performance tests include the verification of torque and power vs. speed characteristics, as well as the efficiency and power factor for different operating conditions.

In order to validate the optimal design objective of prototype interior PMSM, the wide speed operation performance for the prototype interior PMSM is compared with a commercial 400W interior PMSM. The comparison is based on the same drive system configuration and control scheme. The motor parameters for these two motors are listed in Table 5.3.

In the tests of the prototype interior PMSM, torque, shaft power, input power

Table 5.3: Comparison of motor parameters with The Commercial and The Prototype

parameter	The Commercial	The Prototype
$\lambda_m(Wb)$	0.369	0.297
$L_d(H)$	0.059	0.087
$L_q(H)$	0.181	0.167

and rms voltage and current were measured. Torque and shaft power were measured by a torque transducer and a speed sensor. Input power was measured directly by two wattmeters. Line-to-line voltages and line currents were measured directly by voltmeters and ammeters. The measured experimental data are listed in Appendix B.

5.5.1 Torque and Power Capability

In order to measure the maximum torque and power capability, the full external DC link voltage (350V) and motor rated current (2A) are applied in the interior PMSM drive system. The control technique based on constant current trajectory as described in Chapter 2 was used to operate the machines in the constant torque region and flux-weakening region.

The two motors were tested under same conditions. These are given in Table 5.4:

Fig. 5.12 shows the maximum torque capability vs. speed for both of the commercial interior PMSM and the prototype interior PMSM based on optimal

Table 5.4: Test Condition with The Commercial and The Prototype

Specifications	The Commercial	The Prototype
Power Rating (W)	400	400
Rated Line Voltage (V)	310	310
Rated Line Current (A)	1.2	1.2
Airgap Flux Density (Tesla)	0.5	0.5
Hardware Drive Circuit	Same	Same
Firmware Control Algorithms	Same	Same
Measurement Device	Same	Same

design. The torque capability for the prototype motor is slightly lower than the commercial motor, however, the prototype motor has higher torque over the flux-weakening region than the commercial one. This shows that the flux-weakening capability for the prototype motor is superior to the commercial one.

Fig. 5.13 compares the maximum power capability and constant power speed range for the prototype and commercial interior PMSMs.

The range of constant power operation achieved is around the ratio of 1 : 2.6, which is also superior to the commercial motor (1:1.77). It is noted that the actual constant speed range for the prototype interior PMSM is lower than the expected value 1:3.6 by numerical analysis. The excessive friction loss and iron loss causes the drop in the power capability in the high speed range. Considering the limitation of numerical analysis method, total loss cannot be computed accurately. Hence the actual constant power speed range is less than the predicted. However, the

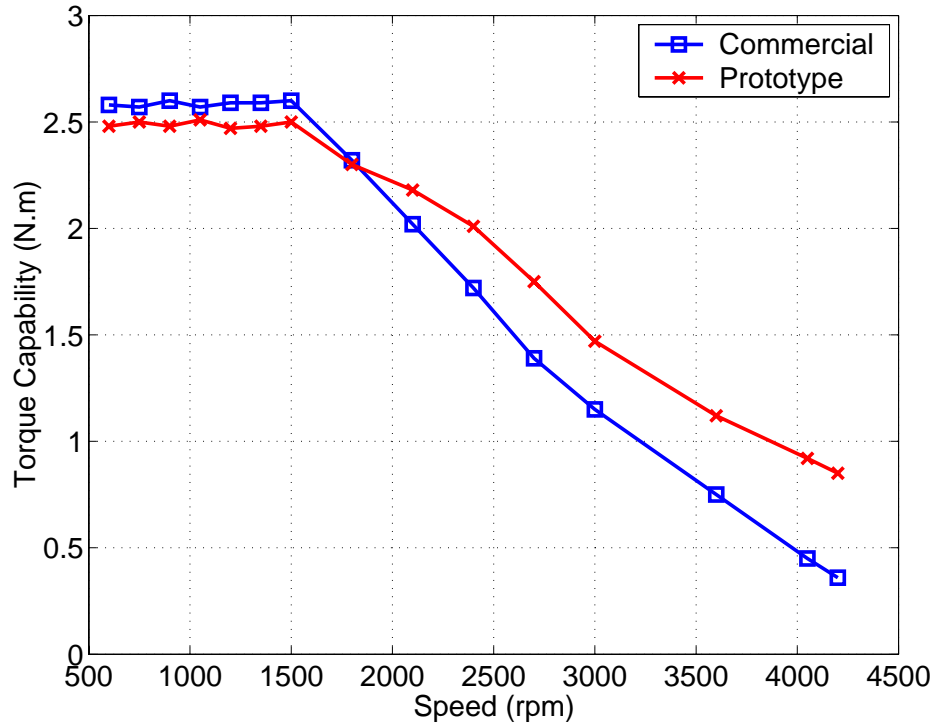


Figure 5.12: Experimental results for the maximum torque capability vs. speed optimization effort to achieve a larger constant power speed range based on design considerations can be validated.

5.5.2 Efficiency and Power Factor

Besides the torque and power capability for the prototype interior PMSM, the efficiency and power factor are the key performance indicators for the whole speed range of operation. These factors affect the motor and the drive in terms of heating and thermal performance as well as power capability over a wide speed range. Efficiency and power factor can be calculated from following equations:

$$\begin{aligned}
 Efficiency &= \frac{Torque \times (speed/60 \times 2\pi)}{P_{in}} \\
 PowerFactor &= \frac{P_{in}}{\sqrt{3}V_{ac}I_a}
 \end{aligned} \tag{5.9}$$

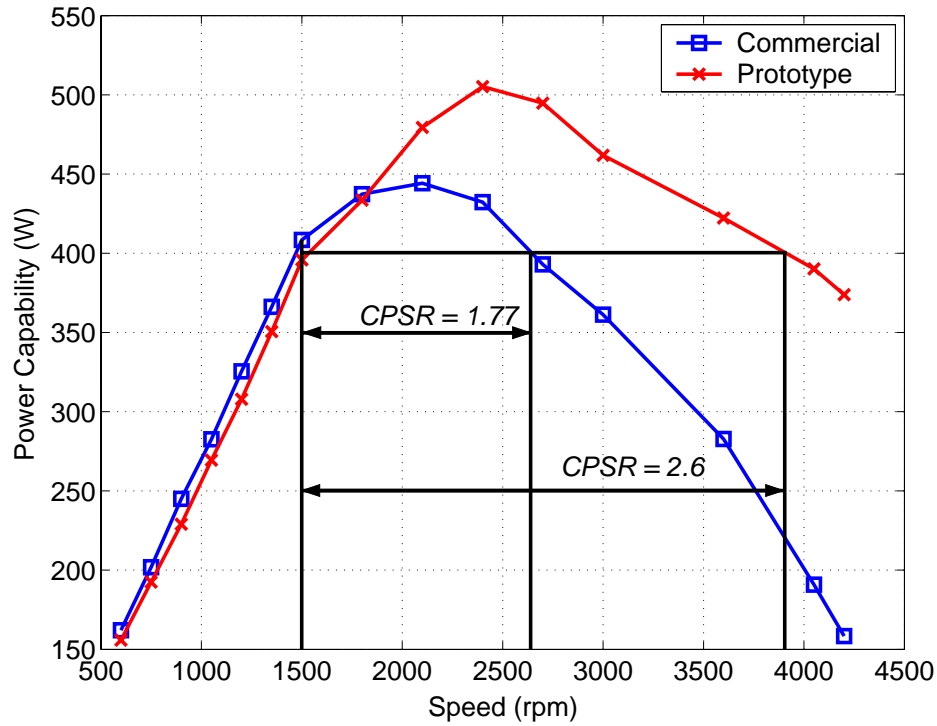


Figure 5.13: Experimental results for the maximum power capability vs. speed

This prototype motor has been tested extensively for steady state operation at different speeds. The efficiency and power factor of the prototype PMSM were derived from the experimental measurements (Appendix B), which are compared with performance for the commercial motor. It is noted that the prototype interior PMSM maintains a good level of efficiency from low speed to rated speed as shown in Fig. 5.14, but its efficiency drops down in the high speed range. The reason is the increased motor core losses in the high speed operation because the harmonic fields increase when the armature current acts to reduce the magnet flux. The power factor for both motors are low in the low speed speed range and light load condition as shown in Fig. 5.15. This is because both motors are supplied by a PWM inverter. The non-sinusoidal voltage and current introduce a distortion factor, which reduces the total power factor. The total power factor is equal to

distortion factor multiplying displacement power factor. The power factor increases to the maximum value beyond the synchronous speed, then it drops again quickly because of most of the current used to weaken the magnet flux.

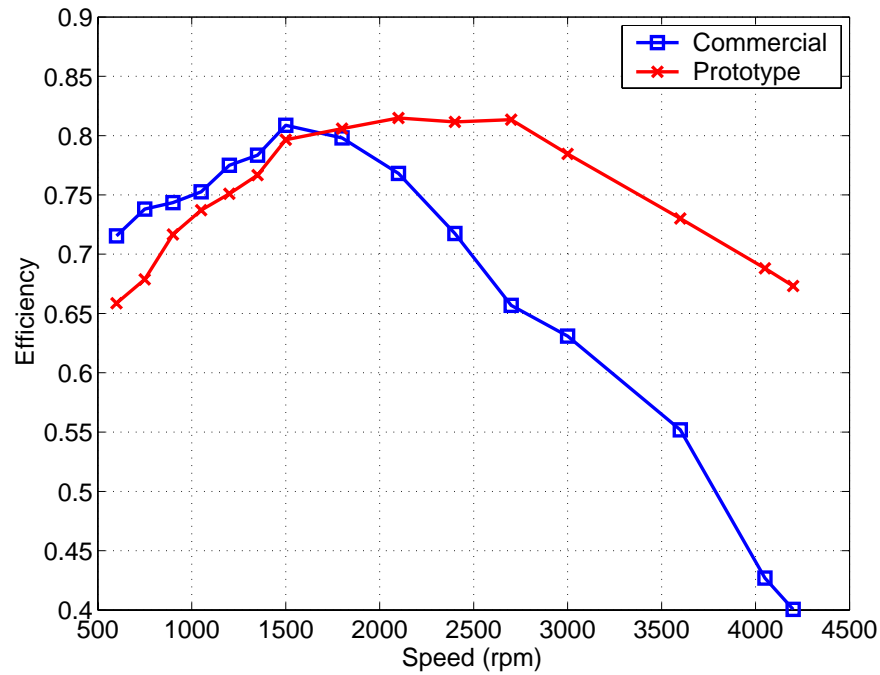


Figure 5.14: Experimental results for the efficiency for constant current and full voltage operation

When compared with the commercial interior PMSM, the efficiency and power factor for the prototype at low speed and rated speed are slightly inferior to the commercial one. This is due to a reduced air-gap magnet flux in the prototype motor as compared to a conventional design. In order to increase the constant power speed range, such a trade-off is necessary. In the flux-weakening speed range, the efficiency and power factor for the prototype are superior to the commercial one. These results further validate the design consideration in order to optimize the constant power speed range rather than the optimal performance in constant torque speed range.

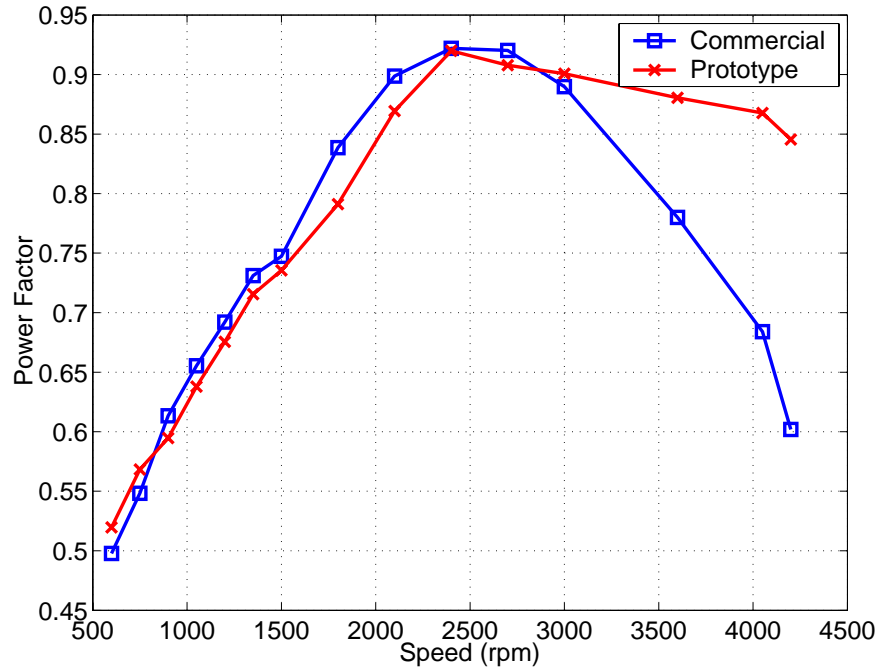


Figure 5.15: Experimental results for the power factor for constant current and full voltage operation

5.5.3 Performance under Reduced DC Link Voltages

In practical application of interior PMSM drives, the input DC link voltage might be decreased due to the uncertainty with external power network. Furthermore, due to the large current change in the dynamics, the dc-link voltage drop on the capacitor is larger than usual. All these unexpected variations can reduce the maximum available voltage in the motor winding terminals and deteriorate the operational performance of the machines. Therefore, tests under reduced DC link voltages are necessary to evaluate the performance of machine to cope with the reduced DC link voltage.

Figs. 5.16 and 5.17 show that the torque and power capability for the prototype motor at 75 percent of the full DC link voltage (262.5V) and at 50 percent

of the full DC link voltage (175V), respectively. It is noted that the speed ranges for constant torque operation are decreased from 1500 rpm to 1150 rpm (75% V_{dc}) and 700 rpm (50% V_{dc}). The available power capability also deteriorates quickly due to the reduction of DC link voltage. However, the torque and power capability for the prototype motor are still slightly better than the commercial one.

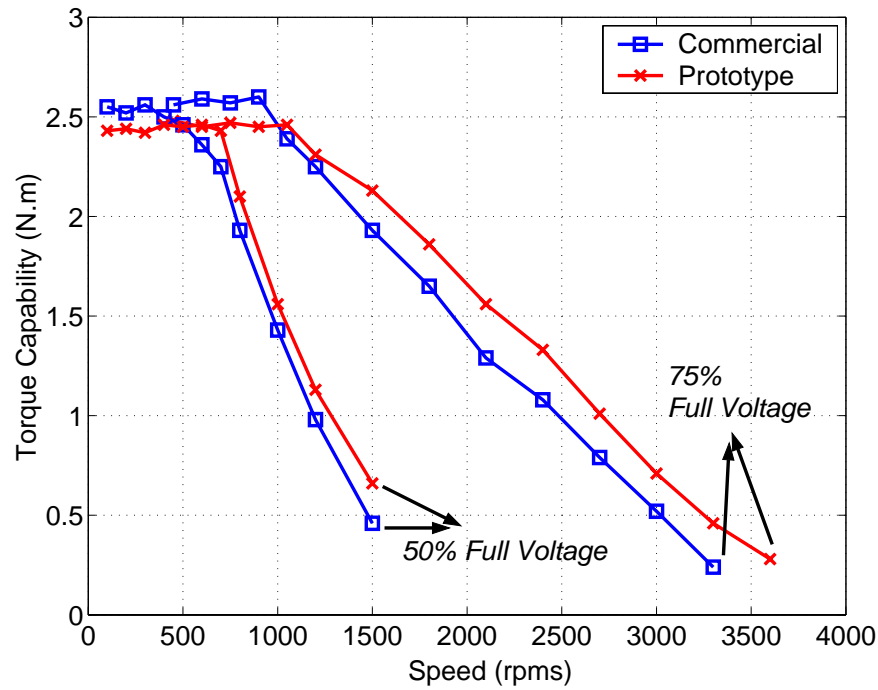


Figure 5.16: Experimental results for the torque capability for constant current and reduced DC link voltage operation

Fig. 5.18 and Fig. 5.19 show the comparison of efficiency and power factor in two machines under reduce DC link voltage. Both machines maintain acceptable efficiency and power factor in lower speed range. However, the prototype interior PMSM displays better performance in the higher speed range because of the improved flux-weakening capability.

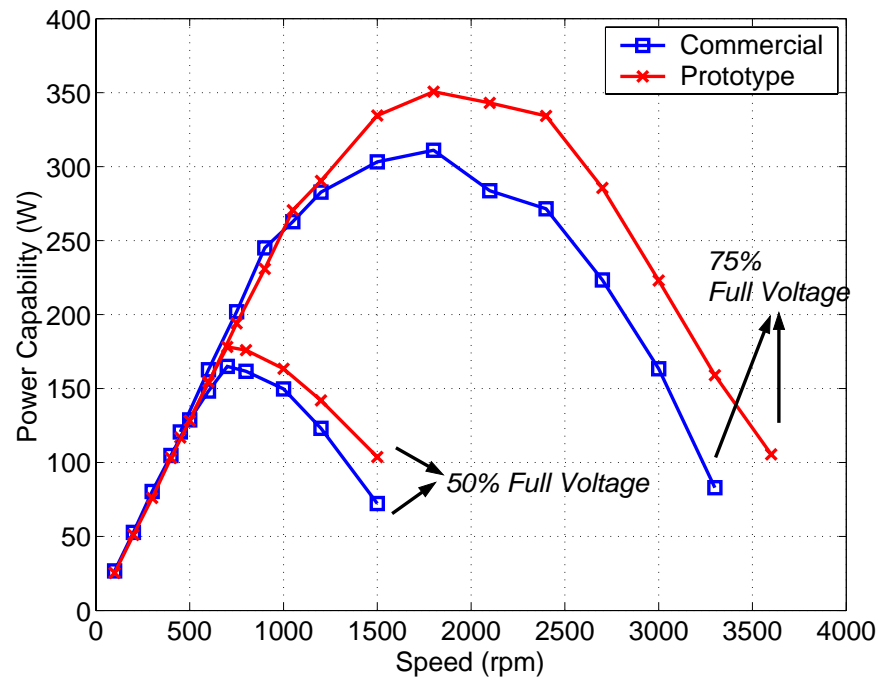


Figure 5.17: Experimental results for the power capability for constant current and reduced DC link voltage operation

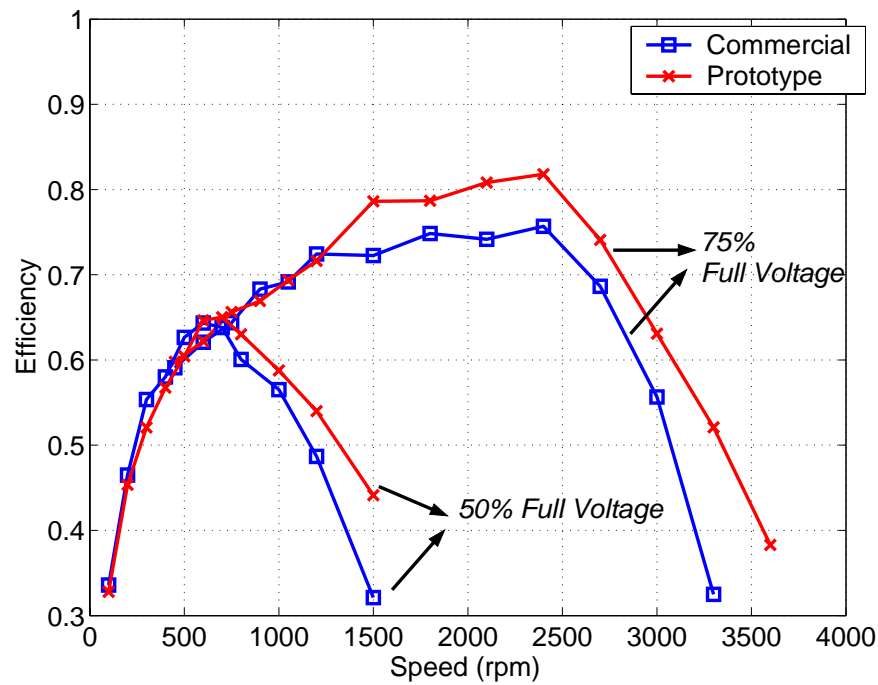


Figure 5.18: Experimental results for the efficiency for constant current and reduced DC link voltage operation

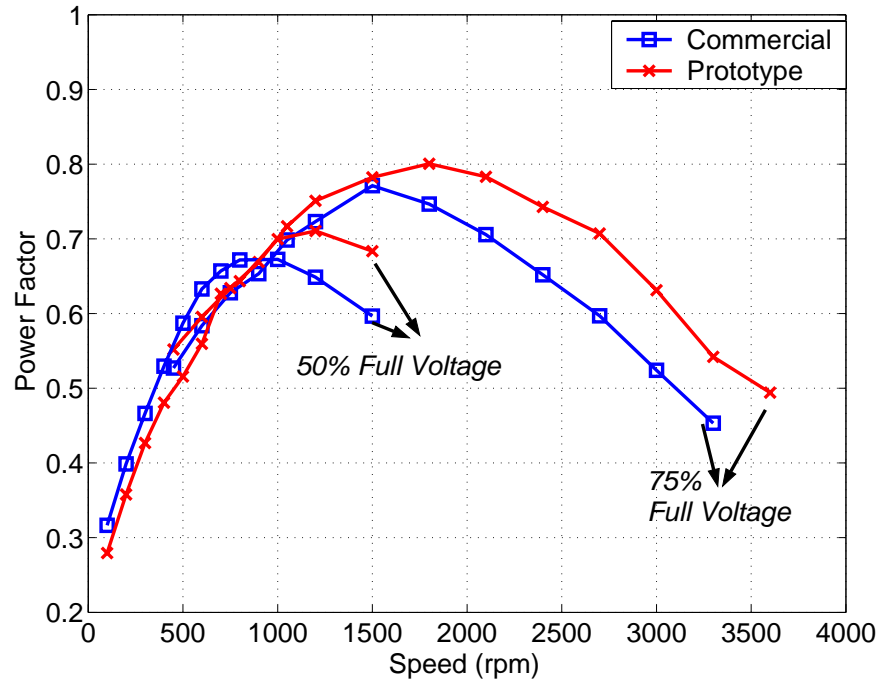


Figure 5.19: Experimental results for the power factor for constant current and reduced DC link voltage operation

5.6 Conclusion

In this chapter, various steady state tests of the prototype interior PMSM have been reported. The tests show that the prototype motor has an excellent torque-speed characteristics and wide speed range of constant power operation. The test results have been compared with the commercial interior PMSMs with the same inverter power rating and control technique.

In open circuit and load test, the measured motor parameters agree with those estimated from the proposed computation approach as specified in Chapter 3. This fact confirms the accuracy of the fitted second order RSM model to estimate the motor parameters.

The efficiency and power factor of the prototype interior PMSM have been measured and compared with those of a commercial 400 W interior PMSM. The comparison indicates that the optimized design realizes the wide-speed constant power operation with no trade-off of its performance on the rated operation.

Chapter 6

Control of The Prototype Interior Permanent Magnet Synchronous Motor

6.1 Introduction

While the design of an interior PMSM for extended speed operation poses several technical challenges, the success of the complete drive system depends on the availability of an appropriate control algorithm that can extract the full performance capabilities from the machine. In particular, special flux weakening control techniques are necessary to achieve constant power operation over a wide speed range. Interior PMSMs are suitable for wide speed operation by flux-weakening method because this kind of machine has a relatively large armature inductance, and as a result, enough flux-weakening effect due to the d-axis armature reaction. The design optimization of interior PMSMs further improves the machines' flux weakening capability and extends the constant power speed range, as discussed in Chapter 3.

Control technique is critical to exploit the power capability of PMSMs in all speed ranges. This chapter first discusses the control performance of traditional field oriented current control scheme for interior PMSMs. More detailed descriptions of this control system are given. The advantages and disadvantages using current regulator in this control method are investigated with theoretical analysis and experimental results. For better speed and torque control performance in the wide-speed range, an improved speed and torque control method for interior PMSMs is proposed in this chapter, and detail comparisons with field oriented current control are presented with experimental results.

6.2 Field Oriented Current Control Scheme

The mathematical model of interior PMSMs in the synchronous d-q coordinates have been presented in Chapter 2 with equations (2.1-2.16). The principle of current control scheme is to force the current vector (I_d, I_q) to follow the optimum current vector trajectory as shown in Fig. 6.1, where the optimal current profile with $\lambda_m > L_d I_{sm}$ is used. Therefore, there are only two operating region divided by the MTPA line (AB) and the current limit line (BM).

6.2.1 Description and features of the current control scheme

Fig. 6.2 illustrates a block diagram of the speed control system implemented with current vector control algorithm [52], which includes three parts: current command generator, current regulator, and flux-weakening voltage controller.

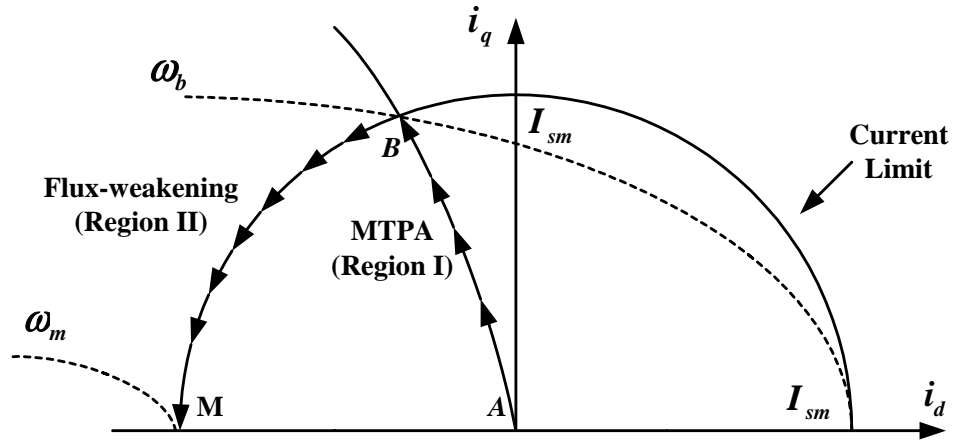


Figure 6.1: The optimum current profile in the d-q coordinate plane for $\lambda_m > L_d I_{sm}$

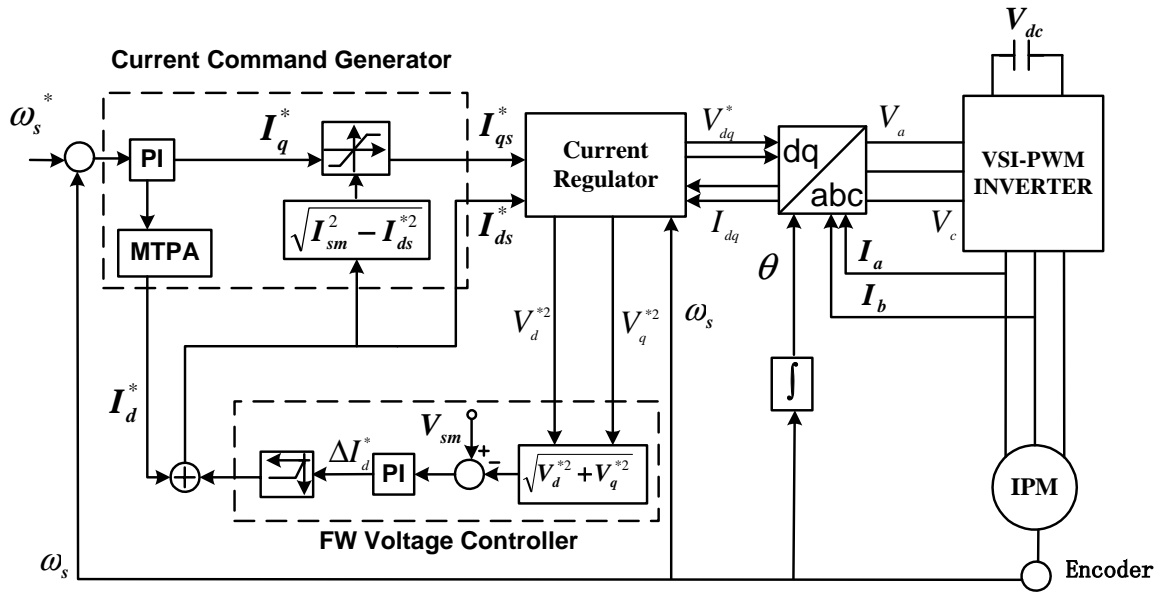


Figure 6.2: Block diagram of current controlled IPMSM drive system

The current command generator provides the reference q-axis current I_q^* and the reference d-axis current I_d^* . I_q^* is decided from the speed error $(\omega_s^* - \omega_s)$ through the proportional-integral controller. The d-axis current command I_d^* is decided by (6.1) in the MTPA line (Region I) until the current regulator begins to saturate.

$$I_d^* = \frac{\lambda_m}{2(L_q - L_d)} - \sqrt{\frac{\lambda_m^2}{4(L_q - L_d)^2} + I_q^{*2}} \quad (6.1)$$

Fig. 6.3 shows the details of current regulator. The d- and q-axis currents cannot be controlled independently by V_d and V_q because of the cross-coupling effects such as $\omega_s L_d I_d$ and $\omega_s L_q I_q$ as shown in (2.12). The cross-coupling effects of the interior PMSM are dominant because the interior PMSMs have relatively large inductances. These effects increase as the speed increases. Therefore, it seems that the current responses as well as torque response are affected by the cross-coupling effects in the high-speed flux-weakening region. The cross-coupling effects can be cancelled by the feed forward compensation as shown in Fig. 6.3. The voltage commands are decided by the PI controller and decoupling feed forward compensation, thus the d- and q-axis current control loops can be linearized by the above decoupling current control.

Without a proper flux-weakening operation, the current regulator would be saturated and lose its controllability at a higher speed. Since the onset of the current regulator saturation varies according to load condition and the machine parameters, the beginning point of flux weakening and the flux level should be changed. A delay in flux-weakening may result in undesired output torque drop

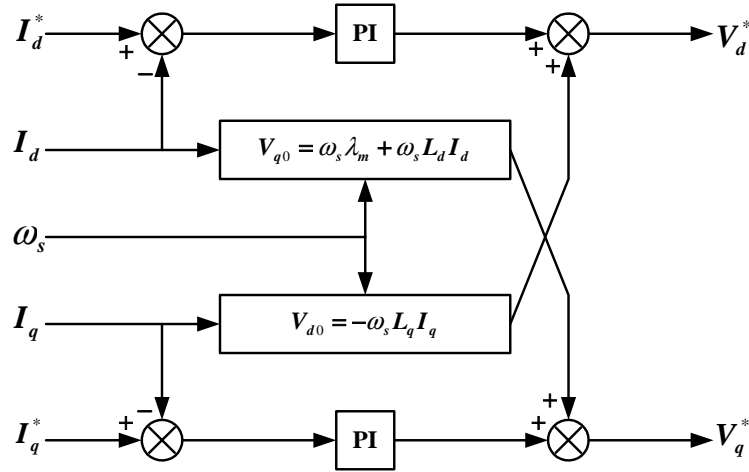


Figure 6.3: Current regulator with decoupling feedforward compensation

according to the saturation of the current regulator, but an early start deteriorates the acceleration performance. Therefore, it is desirable to change the onset point of flux-weakening according to load condition and the machine parameters.

The main idea of flux-weakening voltage controller in current control scheme is the use of the output reference voltage of the synchronous PI current regulator to identify the onset of the flux-weakening. As the speed of the interior PMSM gets higher during acceleration, the output of the current regulator, especially the q-axis current regulator, increases and approaches to the boundary of the pulse width modulator. Without a proper counter measure, the performance of the current regulator gets worse due to the reduced margin of the voltage and finally it loses its controllability. As shown in Fig. 6.2, the voltage regulator ensures the margin of the voltage and increases the d-axis current towards the negative direction to prevent saturation of the current regulators. With this outer voltage regulating loop the flux level is inherently adjusted and the flux-weakening operation is accomplished

automatically. At the low and intermediate speed region, the magnitude of the output voltage of the current regulator V_s is usually less than V_{sm} and thus flux-weakening controller is not activated. Even in this case, if the dc link voltage V_{dc} drops suddenly, the flux-weakening operation can be carried out automatically. The incremental d-axis current ΔI_d^* serves as the control input to the d-axis current for flux-weakening operation.

The basic action of q-axis current limiter is to decrease the q-axis current command I_q^* in response to the presence of a growing d-axis current command I_d^* , so that the total current is within the limit. By decreasing the q-axis current command I_q^* in current limiter and increasing d-axis current command I_d^* towards the negative direction at the same time, the current regulators are able to regain the practical ability of regulating the d-axis and q-axis current (I_d^*, I_q^*) along the current limit circle ($B \rightarrow M$) in Fig. 6.1. The PI output of I_q^* is limited by I_{qmax} , which is determined from (6.2) as shown in Fig. 6.2.

$$I_{qmax} = \sqrt{I_{sm}^2 - I_{ds}^2} \quad (6.2)$$

In the constant torque region, current limiter is not activated, the d- and q-axis current (I_{ds}^*, I_{qs}^*) are on the MTPA trajectory. If current limiter is activated, the current vector (I_{ds}^*, I_{qs}^*) , which initially lies on the MTPA trajectory and inside the voltage limit ellipse at a given speed (Region I: $A \rightarrow B$, in Fig. 6.1) is forced to move along the boundary of the current limit circle (Region II: $B \rightarrow M$) as the speed increases. No additional feedback signal is required to implement the flux-weakening algorithm except the phase currents, the rotor position, V_{dc} and the

speed feedback, which are already available for the speed control in the constructed system as shown in Fig. 6.2.

6.2.2 Discussions on current control schemes

The current vector control scheme for flux-weakening does not utilize the model of interior PMSM but the reference output voltage of the synchronous PI current regulator and the outer voltage control loop, and thus it is robust and less sensitive to load condition and the machine parameters. The current control algorithm described above, works well under the voltage and current limit from zero to base speed. This method can theoretically achieve effective flux-weakening control because it attempts to stop voltage saturation and expand the operating range. However, the voltage references produced by this method must pass the saturated voltage region. Consequently, the original reference output voltages by the current control loop must be replaced by references with modified overmodulation strategy. This result effectively changes the current controller to an unknown stability and performance characteristics, and may not achieve the original control objectives. Therefore, all the four PI gains must be selected appropriately to ensure stability in the voltage saturation region. Generally, current control schemes based on the approach with optimal current profile have at least two more drawbacks: deviations from the prescribed control trajectories due to saturation of current regulator, whereas in the dynamics the available power capability of the inverter is not completely exploited.

6.3 Space Vector Modulation based Direct Torque Control Scheme

In order to overcome some problems in current vector control, we proposed an improved space vector modulation (SVM) based DTC (DTC-SVM) scheme method for IPMSM drive operating not only in constant torque region but also in the flux weakening region. The proposed scheme uses constant switching frequency operation similar to the modulation algorithms discussed by [90]. In addition, using maximum voltage vector with over modulation technique, it provides a faster torque control during dynamic operation and larger constant power speed range in steady state operation.

6.3.1 Principle of torque production in interior PMSMs

The basic idea of the proposed scheme is in the control of the stator flux vector (in amplitude and angular position) with feedback of observed torque and stator flux from measured voltages and currents from motor terminals. The stator flux linkage vector λ_s and rotor flux linkage vector λ_m can be drawn in the $d - q$ coordinate, Fig. 6.4. The angle between the stator and rotor flux linkages, δ , is the load angle or torque angle.

The IPMSM stator flux linkage and electromagnetic torque equations in the $d - q$ coordinate are as follows:

$$\lambda_d = L_d i_d + \lambda_m$$

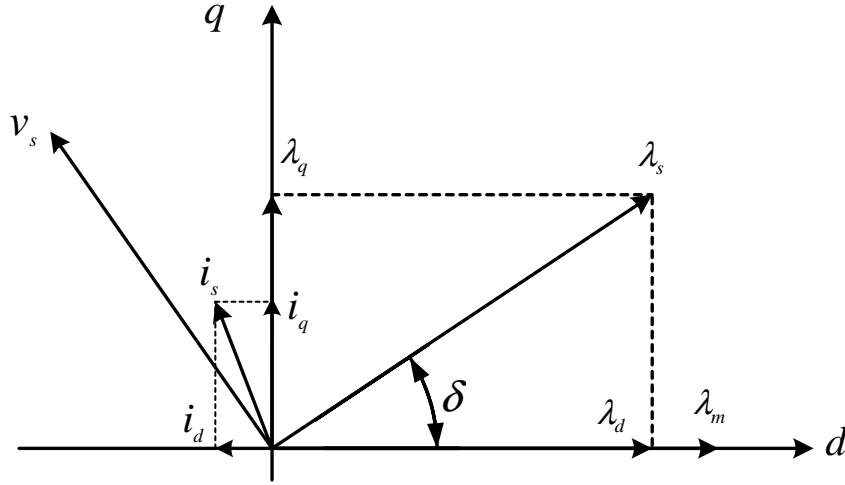


Figure 6.4: The stator flux linkage in the dq reference frame

$$\begin{aligned}\lambda_q &= L_q i_q \\ |\lambda_s| &= \sqrt{\lambda_d^2 + \lambda_q^2}\end{aligned}\tag{6.3}$$

where λ_m , L_d , and L_q are the rotor flux linkage provided by the permanent magnet and two-axis inductances. The torque equation is given as:

$$T_{em} = \frac{3}{2}p(\lambda_d i_q - \lambda_q i_d)\tag{6.4}$$

where p is the pole pairs of the motor. The $d-q$ coordinate current and flux linkage equation can be rewritten as:

$$\begin{aligned}i_d &= \frac{\lambda_d - \lambda_m}{L_d} \\ i_q &= \frac{\lambda_q}{L_q} \\ \lambda_d &= \lambda_s \cos \delta \\ \lambda_q &= \lambda_s \sin \delta\end{aligned}\tag{6.5}$$

The torque expression, substituted (6.5) into (6.4), in terms of the amplitude

of the stator flux linkage and its angle with respect to rotor flux linkage is as follows:

$$T_{\text{em}} = \frac{3}{2}p \cdot \frac{|\lambda_s|}{2L_d L_q} [2\lambda_m L_q \sin \delta - |\lambda_s|(L_q - L_d) \sin 2\delta] \quad (6.6)$$

We can see from (6.6) that by controlling the torque angle between stator and rotor flux, and the magnitude of the stator flux, the electromagnetic torque can be changed accordingly. The torque angle can be changed by changing the position of the stator flux vector with respect to permanent magnet flux vector using the actual voltage vector supplied by PWM inverter. In the steady state, δ is constant and corresponds to a load torque, whereas stator and rotor fluxes rotate at synchronous speed. In transient or dynamic operation, δ varies and the stator and rotor fluxes rotate at different speeds.

6.3.2 Stator flux control in DTC-SVM

In stator coordinate (α - β axis) the stator flux linkage and current can be expressed as:

$$\begin{aligned} \lambda_s &= \lambda_\alpha + j\lambda_\beta \\ i_s &= i_\alpha + ji_\beta \end{aligned} \quad (6.7)$$

Rewriting (6.4) in terms of α - β components the following torque expression is obtained:

$$T_{\text{em}} = \text{Im}\left\{\frac{3}{2}p(\lambda_s \times i_s)\right\} = \frac{3}{2}p(\lambda_\alpha i_\beta - \lambda_\beta i_\alpha) \quad (6.8)$$

The major difference between DTC-SVM and conventional current vector control lies in the absence of the current regulator in the flux and torque control.

Thus, the stator flux components are directly driven by the stator voltage vector in the stator coordinate. The stator flux linkage of a PMSM that can be expressed in the stationary reference frame is

$$\boldsymbol{\lambda}_s = \int (\mathbf{v}_s - r_s \mathbf{i}_s) dt \quad (6.9)$$

During the switching interval, each voltage vector is constant, and (6.9) is then written as:

$$\boldsymbol{\lambda}_s = \mathbf{v}_s t - r_s \int \mathbf{i}_s dt + \boldsymbol{\lambda}_{s|t=0} \quad (6.10)$$

The initial value of $\boldsymbol{\lambda}_{s|t=0}$ is not zero for PMSM's because of the existence of permanent magnet. It can be obtained from the initial rotor positions. In digital implementation the integration of the stator flux is as follows:

$$\begin{aligned} \lambda_\alpha(k) &= [v_\alpha(k) - r i_\alpha(k)] T_s + \lambda_\alpha(k-1) \\ \lambda_\beta(k) &= [v_\beta(k) - r i_\beta(k)] T_s + \lambda_\beta(k-1) \end{aligned} \quad (6.11)$$

where T_s is the sampling period and k represents the actual discrete time. The $\alpha - \beta$ components of the command stator flux can be written as:

$$\begin{aligned} \lambda_\alpha^*(k) &= \lambda_s^*(k) \cos(\theta_s(k) + \omega_s(k) T_s + \Delta\delta(k)) \\ \lambda_\beta^*(k) &= \lambda_s^*(k) \sin(\theta_s(k) + \omega_s(k) T_s + \Delta\delta(k)) \end{aligned} \quad (6.12)$$

where $\omega_s(k)$ is the present speed of stator flux and $\Delta\delta(k)$ is the change of torque angle; $\theta_s(k)$ is the position of the present stator flux linkage vector as shown in Fig. 6.5, which can be estimated by the present $\alpha - \beta$ component of stator flux vector:

$$\theta_s(k) = \arctan\left(\frac{\lambda_\beta(k)}{\lambda_\alpha(k)}\right) \quad (6.13)$$

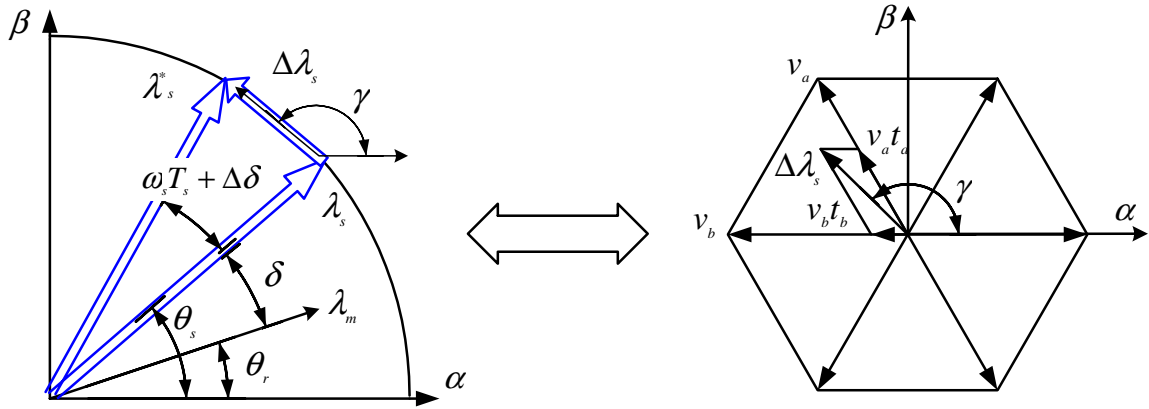


Figure 6.5: The steady state operation of stator flux control

The flux error between the command stator flux vector and actual stator flux vector can be obtained by:

$$\Delta\lambda_\alpha(k) = \lambda_\alpha^*(k) - \lambda_\alpha(k)$$

$$\Delta\lambda_\beta(k) = \lambda_\beta^*(k) - \lambda_\beta(k)$$

$$\Delta\lambda_s(k) = \Delta\lambda_\alpha(k) + j\Delta\lambda_\beta(k) \quad (6.14)$$

In stator flux control, we strive to achieve zero error for the stator flux vector in one sampling time. This condition gives us the requirements for the on-time and choice of the switching state vectors of a voltage source inverter.

$$\Delta\lambda_s(k) = \mathbf{v}_a t_a + \mathbf{v}_b t_b \quad (6.15)$$

where \mathbf{v}_a and \mathbf{v}_b are the voltage vectors produced by adjacent active switching states of a three phase voltage source inverter as shown in Fig. 6.5; t_a and t_b are the switching on time of two adjacent active voltage vectors.

For dynamic operations, the reference stator flux vector is forced to rotate faster than rotor flux. Meanwhile, it is important that the magnitude of stator flux

vector is increased in the constant torque operation to achieve maximum torque per ampere (MTPA) as described in [91], while in the flux weakening region, the magnitude of stator flux vector has to be reduced as the speed increases. The principle to adjust stator flux amplitude in different operating region will be discussed later.

6.3.3 Calculation of switching on time

A three-phase machine being fed from a switched power converter, Fig. 6.6 (a), have the switch pairs $S1 - S4$ ($S2 - S5$, and $S3 - S6$) form half-bridge; one, and only one switch in a half-bridge is closed at a time. The waveform of the phase voltage (V_a , V_b and V_c) is displayed in the upper trace of Fig. 6.6 (b) and the peak value of phase voltage is $\frac{2}{3}V_{dc}$. Therefore, there are six active switching state vectors as shown in Fig. 6.8, where in brackets the switching polarities of three half-bridge are indicated. The switching state vectors describe the inverter output voltages. At operation with PWM waveforms, the two zero vectors V_0 and V_7 are included in the pattern in Fig. 6.8 which are associated with those inverter states with all upper or all lower half-bridge switches closed, respectively [92].

The modulation index is the normalized fundamental voltage, define as:

$$m = \frac{V_s}{V_{smax}} \quad (6.16)$$

where V_s is the fundamental voltage of the modulated switching sequence and V_{smax} is the fundamental voltage at six-step operation as shown in Fig. 6.6 (b), which is

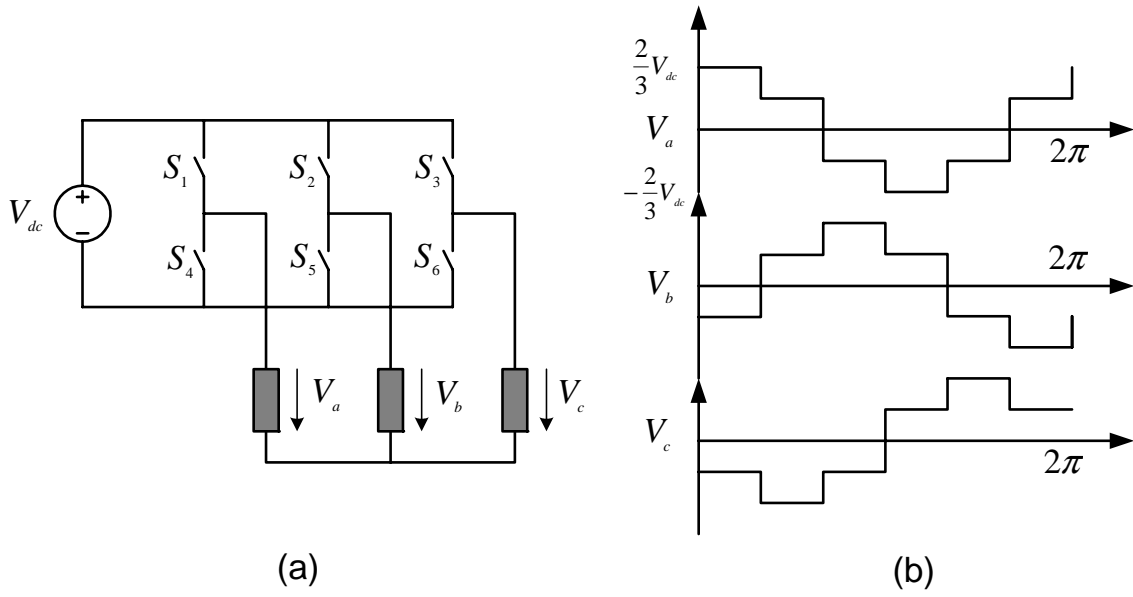
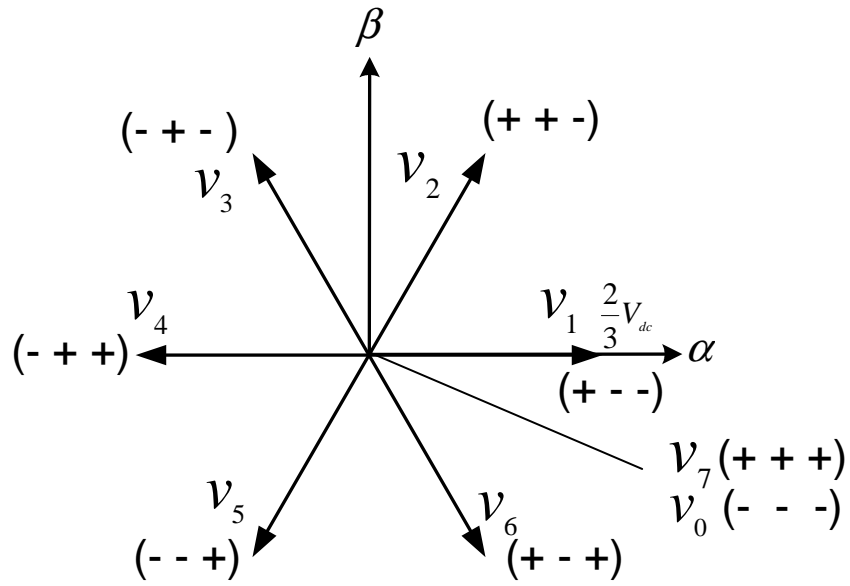


Figure 6.6: Three-phase converter and phase voltage

Figure 6.7: Switching state vectors in the $\alpha - \beta$ plane

calculated by Fourier transformation as:

$$V_{\text{smax}} = \frac{2}{\pi} V_{\text{dc}} \quad (6.17)$$

Using space vector modulation technique, we can achieve $0 \leq m \leq 1$, and unity modulation index can be obtained only in six-step mode. As the maximum power of a PWM converter is proportional to the maximum power voltage at the ac side, the maximum modulation index m_{\max} constitutes an important utilization factor of the equipment.

6.3.3.1 Normal modulation range

In the normal modulation range, the reference voltage vector V_s is always within the hexagon as shown in Fig. 6.8 (a).

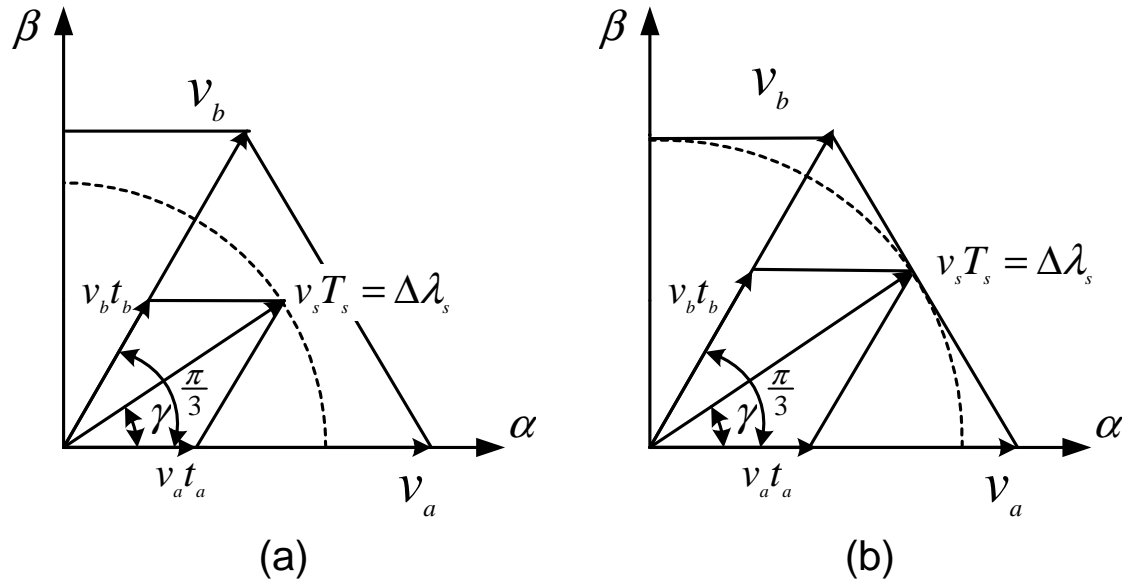


Figure 6.8: Space vector modulation with switching state vectors

Based on geometric relationship in triangle, we can obtain the following equations:

$$\begin{aligned} \frac{|V_a t_a|}{|\Delta \lambda_s|} &= \frac{\sin(\pi/3 - \gamma)}{\sin(\pi/3)} \\ \frac{|V_b t_b|}{|\Delta \lambda_s|} &= \frac{\sin \gamma}{\sin(\pi/3)} \end{aligned} \quad (6.18)$$

where $|\mathbf{v}_a| = |\mathbf{v}_b| = \frac{2}{3}V_{dc}$; γ is the position of stator flux error vector $\Delta\lambda_s$, which can be estimated as:

$$\gamma = \arctan\left(\frac{\Delta\lambda_\beta}{\Delta\lambda_\alpha}\right) \quad (6.19)$$

Hence the switching on-times of the respective vectors are given as:

$$\begin{aligned} t_a &= \frac{3}{2V_{dc}} \cdot \frac{|\Delta\lambda_s| \sin(\pi/3 - \gamma)}{\sin(\pi/3)} \\ t_b &= \frac{3}{2V_{dc}} \cdot \frac{|\Delta\lambda_s| \sin(\gamma)}{\sin(\pi/3)} \\ t_0 &= T_s - t_a - t_b \end{aligned} \quad (6.20)$$

6.3.3.2 In overmodulation range

As the angular velocity of stator flux ω_s is increased, $|\Delta\lambda_s|$ increases. The on-times of active states could be so large that no zero vector can be switched, which means that the reference voltage vector eventually touches the boundary of the hexagon as shown in Fig. 6.8 (b). The controllable range of linear modulation methods terminates at this point. Further increasing the modulation index up to 1, overmodulation technique has to be applied [92]. On the hexagon sides, the stator flux error amplitude can be obtained as:

$$|\Delta\lambda_s| = \frac{T_s |\mathbf{v}_a| \sin(\pi/3)}{\sin(\pi/3 + \gamma)} \quad (6.21)$$

Hence, the modified switching on time of active voltage states are derived by substituting (6.21) into (6.20):

$$\begin{aligned} t_a &= \frac{T_s \sin(\pi/3 - \gamma)}{\sin(\pi/3 + \gamma)} \\ t_b &= T_s - t_a \end{aligned} \quad (6.22)$$

An additional singular operating point exists in the six step mode. It is characterized by the switching sequence $\mathbf{v}_1 - \mathbf{v}_2 - \mathbf{v}_3 - \mathbf{v}_4 - \mathbf{v}_5 - \mathbf{v}_6$ and the maximum possible stator flux error can be calculated as:

$$|\Delta\lambda_{\text{smax}}| = V_1 T_s = \frac{2V_{\text{dc}}}{3} \cdot T_s \quad (6.23)$$

6.3.4 Stator flux estimation

Voltage model (6.9) has been used for estimating the stator flux vector. To prevent integrator saturation in voltage model of stator flux vector estimation, low pass filtering is employed. For the operating angular frequencies greater than the cut off frequency of this filter, faithful results are obtained. However, at frequencies close to the filter cut off, large magnitude and phase error occur. To mitigate this problem, inverse magnitude and phase angle gains was used to compensate for the error created due to low pass filtering. The poles of this modified low pass filter are made to change with respect to the angular velocity of operation. However, the extent of shifting of poles is decided by trial and error. Figure 6.9 shows the method [90].

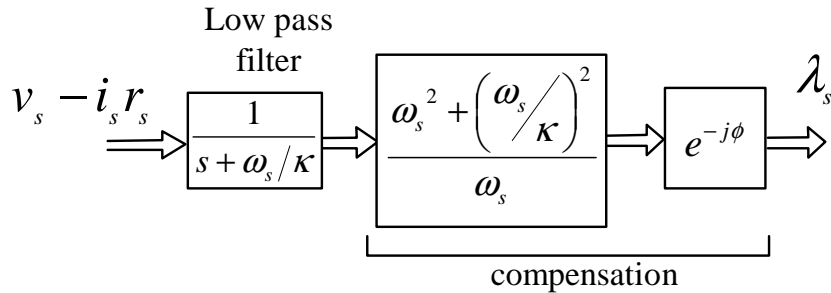


Figure 6.9: Modified voltage model for flux estimation

Compensation in the magnitude and angle of the stator flux vector is done after low pass filtering. This method is good at discarding high frequency noise but the dc-offset still appears at the output of the filter, specially at very low operating velocities. Moreover, the closed loop operation at speeds around zero will depend upon the parameter κ which needs to be tuned by trial and error. Following equation is used for stator flux estimation,

$$\boldsymbol{\lambda}_s = \int \{(1 - j\kappa \text{sign}(\omega_s))(\mathbf{v}_s - \mathbf{r}_s \mathbf{i}_s) - \kappa \omega_s \boldsymbol{\lambda}_s\} dt \quad (6.24)$$

here, ω_s is the synchronous speed (angular velocity) and κ is a tuning parameter. The poles of the resulting low pass filter will change corresponding to the operating angular velocity. This model will work well only if the following two conditions are satisfied. (a) amount of dc-offset is same for the sensed currents and (b) analog gains provided by the anti noise/aliasing filters are exactly equal. Implementation of the modified voltage model helps to deal with the problems of noise and drift.

6.3.5 Operating Limits for DTC-SVM scheme in IPMSM drives

The critical condition for DTC which can be applied to IPMSM drive system is that a positive $dT_{em}/d\delta$ should be ensured within the normal operating condition of the motor [69].

$$\frac{dT_{em}}{d\delta} = \frac{3}{2}p \cdot \frac{|\lambda_s|}{L_d L_q} [\lambda_m L_q \cos \delta - |\lambda_s| (L_q - L_d) \cos 2\delta] \geq 0 \quad (6.25)$$

According to (6.6), the torque vs. load angle characteristic with respect to different stator flux amplitude is plotted in Fig. 6.10 (motor parameters are given in Table

5.3). The derivative of torque w.r.t δ near the region where $\delta = 0^\circ$ is negative when

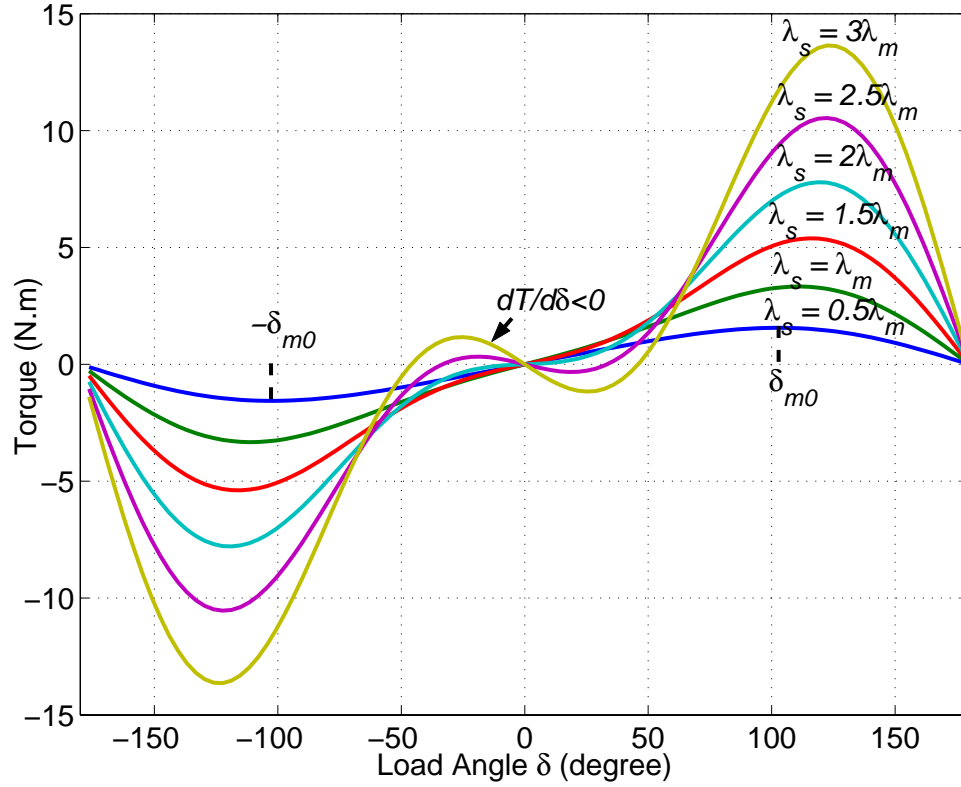


Figure 6.10: The torque vs. load angle characteristics

the stator flux $|\lambda_s| = 3\lambda_m$, which will cause unstable operation of IPMSM drive by using direct torque control.

Therefore, by (6.25), the condition for positive $dT_{em}/d\delta$ around $\delta = 0^\circ$ is given by:

$$|\lambda_s| < \frac{L_q}{L_d - L_q} \lambda_m \quad (6.26)$$

Meanwhile, the maximum allowable angle δ_{m0} which ensure a positive $dT_{em}/d\delta$ can be obtained by solving (6.25) as:

$$\frac{3}{2}p \cdot \frac{|\lambda_s|}{L_d L_q} [-2|\lambda_s|(L_q - L_d) \cos^2 \delta + \lambda_m L_q \cos \delta + |\lambda_s|(L_q - L_d)] \geq 0 \quad (6.27)$$

Therefore,

$$\delta_{m0} = \cos^{-1} \left(-\frac{b_0}{2a_0} + \sqrt{\frac{b_0^2 - 4a_0c_0}{4a_0^2}} \right) \quad (6.28)$$

where

$$\begin{aligned} a_0 &= -2\lambda_s(L_q - L_d) \\ b_0 &= \lambda_m L_q \\ c_0 &= \lambda_s(L_q - L_d) \end{aligned} \quad (6.29)$$

6.3.6 Current Constraints

The analysis for maximum load angle ensures the proper operation of stator flux oriented DTC in interior PMSM drives. However, the current constraint is not considered in maximum allowable angle δ_{m0} as shown in (6.28). As the stator flux linkage is the vector sum of armature flux linkage and permanent magnet flux linkage, in the stator flux based DTC-SVM, the magnitude of stator flux linkage and load angle δ must be limited to prevent the current exceeding the inverter rating or motor thermal rating I_{smax} .

$$i_s^2 = i_d^2 + i_q^2 < I_{smax}^2 \quad (6.30)$$

By substituting (6.5) into (6.30), we get the relation of stator flux magnitude and phase current as shown in (6.31).

$$i_s^2 = \left(\frac{|\lambda_s| \cos \delta - \lambda_m}{L_d} \right)^2 + \left(\frac{|\lambda_s| \sin \delta}{L_q} \right)^2 \quad (6.31)$$

Fig. 6.11 shows phase current vs. load angle characteristics when stator flux linkage $|\lambda_s|$ is varied. It suggests that the phase current varies with the load angle

increasing from 0° to 180° .

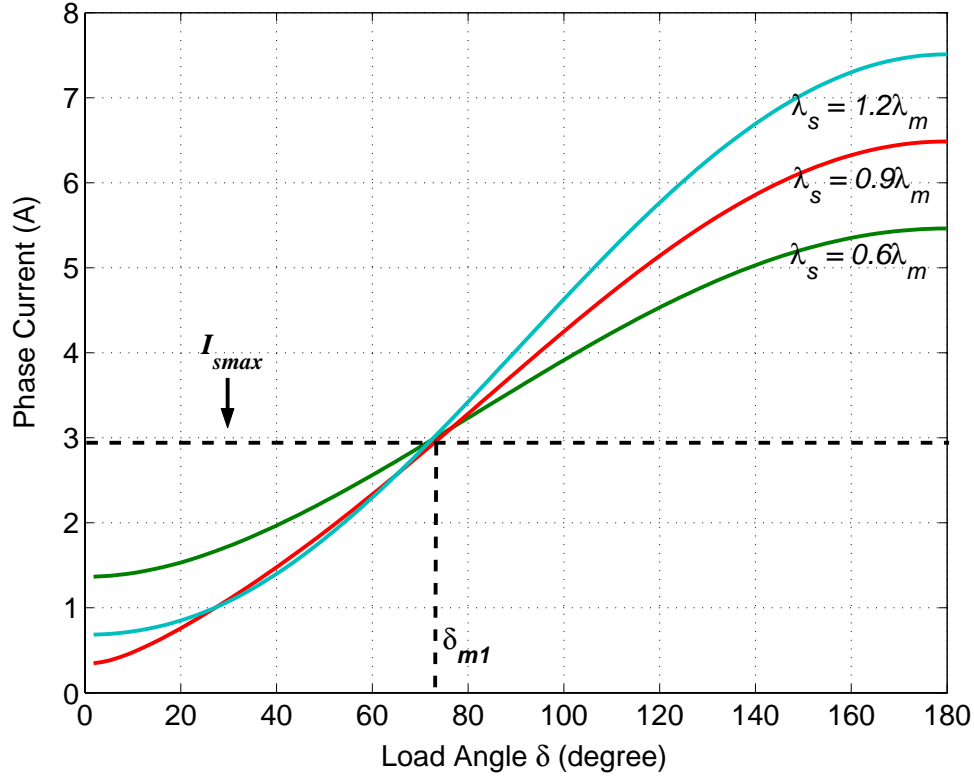


Figure 6.11: The phase current vs. load angle characteristics

In order to prevent phase current exceeding the constraint, we must limit the load angle. Rewriting (6.31) and equating $i_s = I_{\text{smax}}$, we have following equation:

$$(L_q^2 - L_d^2)\lambda_s^2 \cos^2 \delta + 2L_q^2\lambda_s\lambda_m \cos \delta + L_d^2(\lambda_s^2 - I_{\text{smax}}^2 L_q^2) = 0 \quad (6.32)$$

Therefore, the maximum load angle δ_{m1} with current limitation can be obtained by solving (6.32) as:

$$\delta_{m1} = \cos^{-1}\left(-\frac{b_1}{2a_1} + \sqrt{\frac{b_1^2 - 4a_1c_1}{4a_1^2}}\right) \quad (6.33)$$

where

$$a_1 = (L_q^2 - L_d^2)\lambda_s^2$$

$$\begin{aligned}
b_1 &= 2L_q^2\lambda_s\lambda_m \\
c_1 &= L_d^2(\lambda_s^2 - I_{smax}^2L_q^2)
\end{aligned} \tag{6.34}$$

The two maximum load angle curves with respect to stator flux linkage for positive $dT_{em}/d\delta$ requirement and current limitation requirement can be plotted in the same graph as shown in Fig. 6.12. The two trajectories cross at point (λ_{s0}, δ_m) , and divide the λ_s - δ plane into four regions. It is obvious that IPMSM drive can only operate inside region 1 in Fig. 6.12, which ensures both current limitation and positive $dT_{em}/d\delta$ requirement.

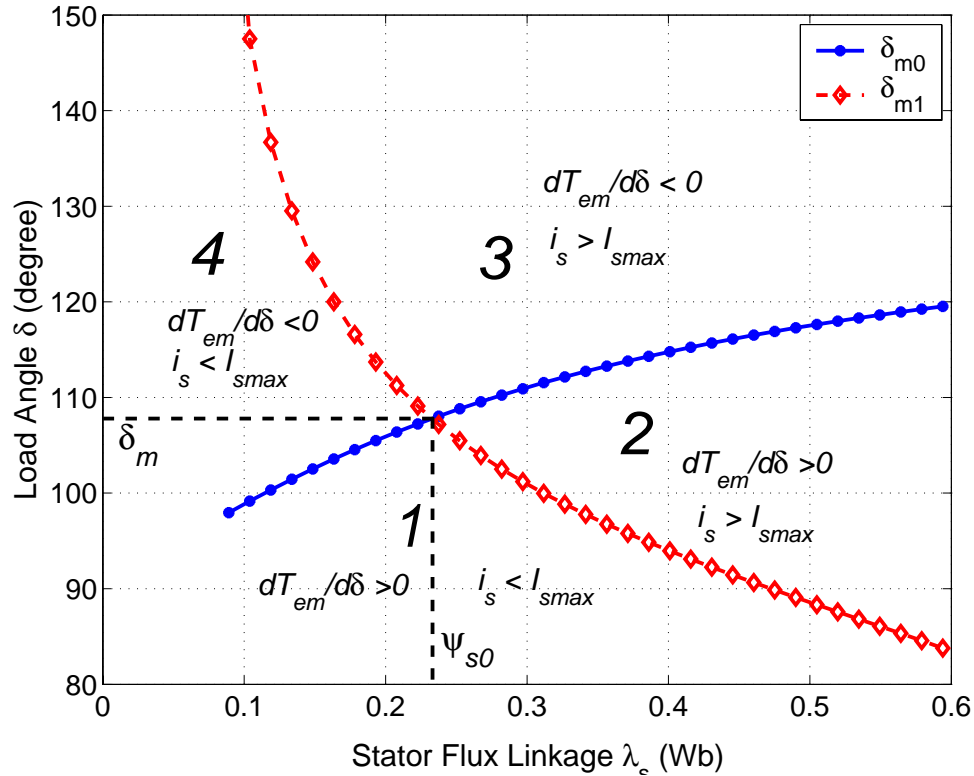


Figure 6.12: The comparison of maximum load angle: δ_{m0} and δ_{m1} Vs. λ_s

6.3.7 Proposed Wide Speed Operation

In interior PMSM drives, operating in constant torque region, the torque capability is limited by current constraint only. The maximum torque per ampere (MTPA) control has been applied to field oriented current controlled IPMSM drives in constant torque operation as described in [7]. In space vector modulation based DTC scheme, the direct control of current is not possible. However, the stator flux linkage is produced by both of armature flux and permanent magnet flux. Therefore, the stator flux reference can be selected to realize the MTPA control indirectly. Fig. 6.13 illustrates the characteristics of torque capability with respect to stator flux reference and load angle. The constant current trajectory described in pervious section is also plotted in the same graph with the dash lines. Fig. 6.13 is used to determine the maximum torque capability for different current ratings. Conversely, the optimal stator flux reference for MTPA control is determined for certain torque reference.

In many applications such as electric traction drives, the flux weakening is required due to increasing motor speed or decreasing dc link voltage. The torque capability in flux weakening operation is limited by both current and voltage constraints. In order to extract the full performance capabilities from the machine and achieve fast speed and torque control dynamics, the proposed flux weakening control technique is based on feed forward stator flux control. In the flux weakening operation, the stator flux level is reduced by the increment of motor speed.

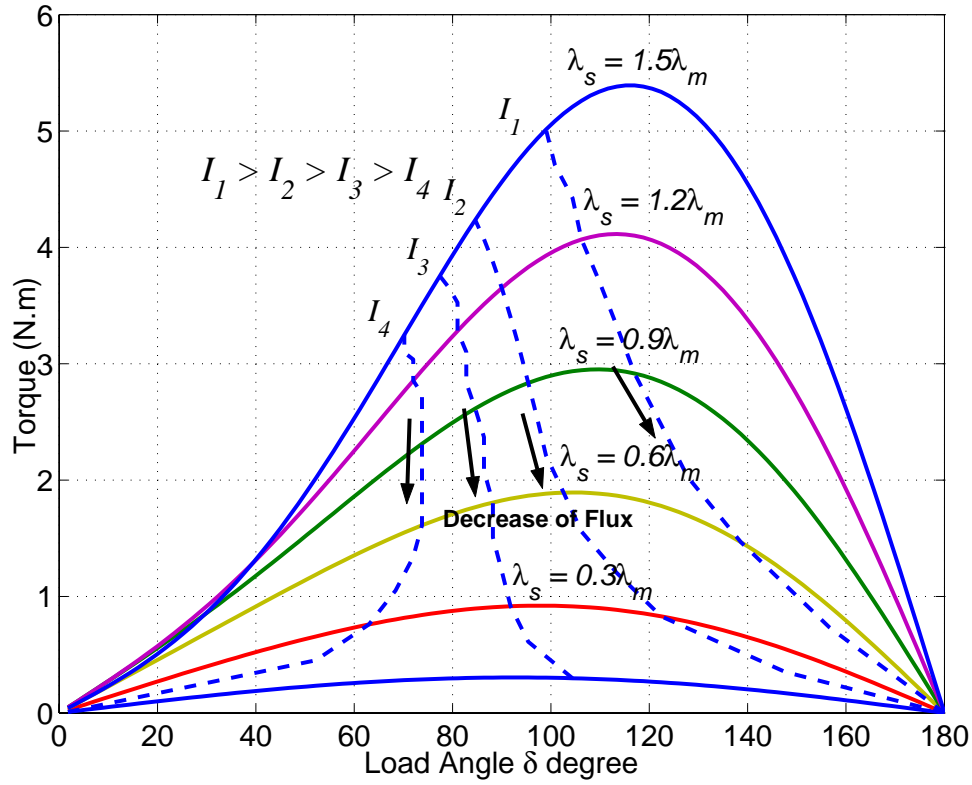


Figure 6.13: The characteristics of torque capability vs. stator flux linkage

Torque capability varies according to stator flux level. Therefore, torque capability also decreases as the motor speed increases. Considering the maximum current constraint, the torque capability is further limited. Again, Fig.6.13 is used to determine the torque capability through the stator flux reference and current rating.

Therefore, the stator flux reference profile in constant torque region and flux-weakening region can be plotted in Fig. 6.14. Fig. 6.14 and Fig. 6.12 can be used to compute the stator flux reference and load angle limit, respectively. In practical applications, it is not desirable to calculate the stator flux reference and load angle limit using the figures and equations because the machine parameters may change due to saturation and other conditions. In order to cope with the nonlinearity in

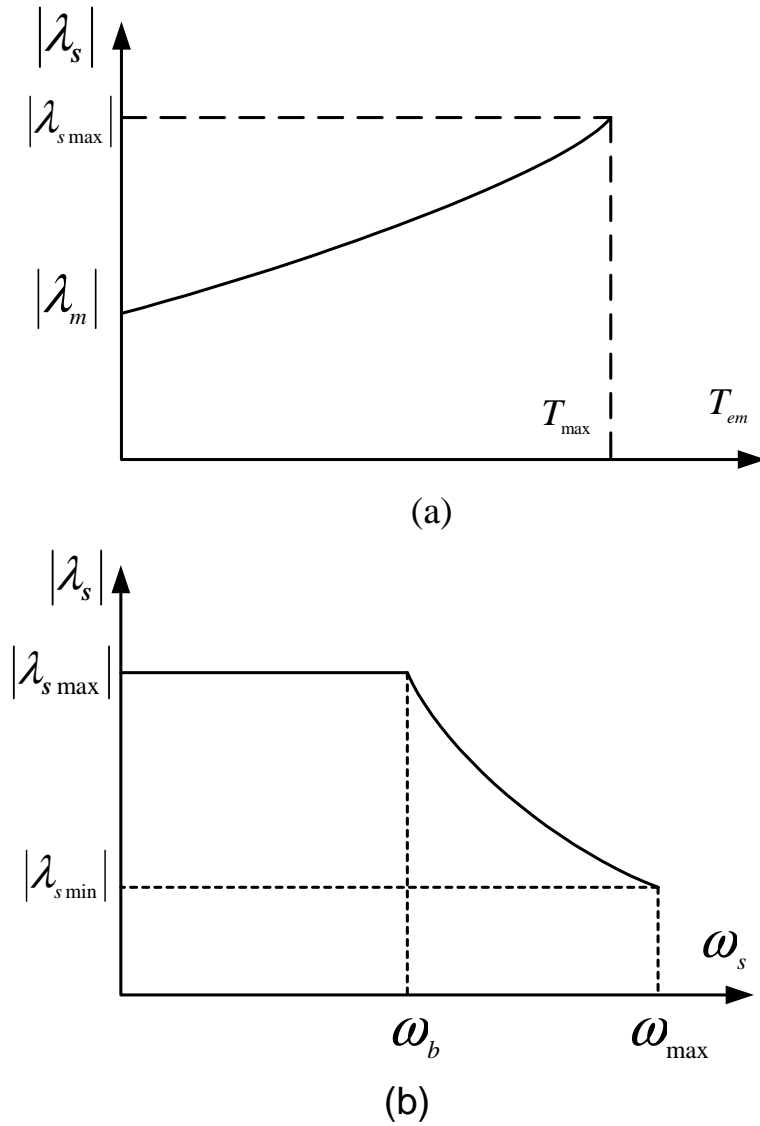


Figure 6.14: The Stator Flux Reference Profile: (a) Constant torque operation with MTPA control; (b) Flux-weakening Operation

interior PMSMs, the stator flux reference and load angle limit can be derived from tables which include the measured values from off-line experiments.

6.4 Description and Features of the Proposed Scheme

Fig.6.15 illustrates a block diagram of the speed and torque control system implemented with the proposed flux weakening control algorithm.

6.4.1 Speed Range for Operation at Constant Torque

The command speed ω_s^* is compared with the encoder feedback speed ω_s and the speed error is used as the input of speed controller. When the output of speed controller (reference torque T^*) is higher than the estimated torque T , the torque controller will force the stator flux λ_s to rotate at a higher speed to increase the angle between the stator flux and rotor flux, which is the load angle δ , such that the torque error is zero. The torque reference is also used to generate the reference stator flux level $|\lambda_s|$ according to the MTPA principle described earlier.

The motor torque is controlled by the torque regulator, which includes a PI controller and load angle limiter. The load angle limitation is to prevent the motor phase current exceeding the maximum current constraint. The output torque and stator flux linkage are estimated based on the phase current and voltage. The stator flux vector generator is used to determine reference stator flux linkage vector. Voltage space vector and their duration are selected and calculated according to the error flux linkage vector by using (6.20), such that the flux error can be fully compensated.

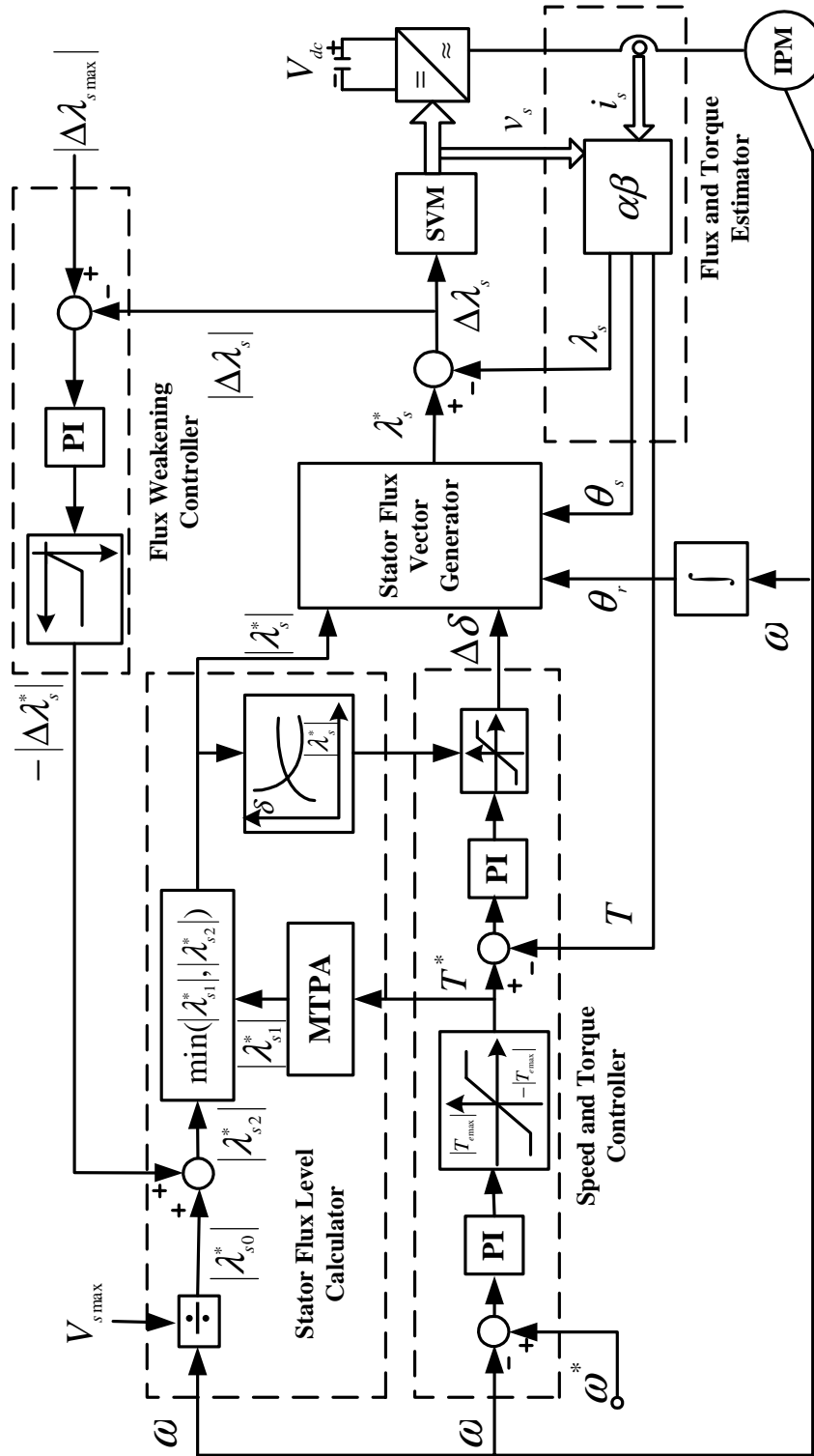


Figure 6.15: Block diagram of IPMSM drive system

6.4.2 Operating in flux-weakening speed range

The principle of speed and torque control is similar in the whole speed range. However, in the flux-weakening speed range, the stator flux reference calculator is used to produce two stator flux reference $|\lambda_{s1}^*|$ and $|\lambda_{s2}^*|$. $|\lambda_{s1}^*|$ is taken from Fig. 6.14 (a) for MPTA control only, while $|\lambda_{s2}^*|$ is calculated with the available maximum voltage from inverter and actual motor speed. The proposed feed forward stator flux control compares these two stator flux reference and selects the smaller one as the input of stator flux vector generator. Meanwhile, the load angle limit is determined from the selected stator flux reference according to Fig. 6.12. By the feed forward stator flux control, the desired stator linkage can be controlled with fast dynamics. However, the magnetic characteristics can change due to the temperature or manufacturing tolerances. The supplied voltage is composed of not only the back-EMF voltage, but the resistance drop and the core loss components, as well. Therefore, the closed-loop control is added and flux error is compared with the maximum flux error by the PI regulator with anti-windup as described in Fig. 6.15 with flux weakening controller.

6.5 Experimental Results and Discussions

Experiments were performed on the 400 W prototype interior PMSM run with a voltage source inverter. The DC link voltage was deliberately reduced to 160V (or 0.636 p.u., the base values of motor parameters are listed in Table. 6.1) in order

to let flux weakening come earlier in the lower speed range.

Table 6.1: Base values of motor parameters

Base Item	Value
Phase Voltage (V)	163.3
Phase Current (A)	2.8
Rated Frequency (Hz)	50
Pole Pairs	2

The implementation was carried out on a dSPACE/DS1102 card. In order to verify that the proposed control scheme is better than conventional method, the conventional field oriented current vector control scheme [52] is also implemented in the same control board. The two control programs have the same sampling period and switching frequency.

The comparison of current vector control and SVM based DTC for the dynamic response of step speed change in the normal range is shown in Fig. 6.16 and Fig. 6.17, respectively. When changing the speed from 0 to 1.0 pu. (0 - 1500rpm), the settling time for current control is 80ms, while it is 60ms only for SVM based DTC. The two estimated torques for current control and SVM based DTC are also compared in the Figs. 6.16 and 6.17, which shows that the average torque production for SVM based DTC is larger than that for current control. This result helps to explain the reason that the speed response for SVM based DTC is faster than that of current control. The estimated stator flux (6.9) for SVM based DTC plotted in Fig. 6.17 shows that, with MTPA control, the flux level is changing from

1.0 to 1.4 p.u. with respect to 1.0 p.u. torque production in the dynamics.

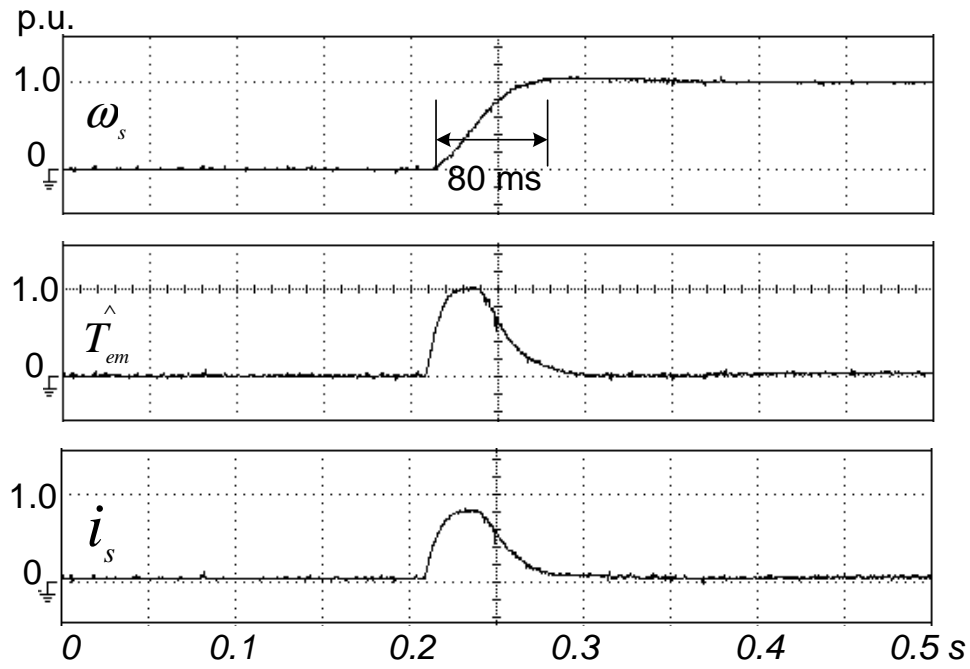


Figure 6.16: Current Control: The dynamic response with step speed change in the normal range

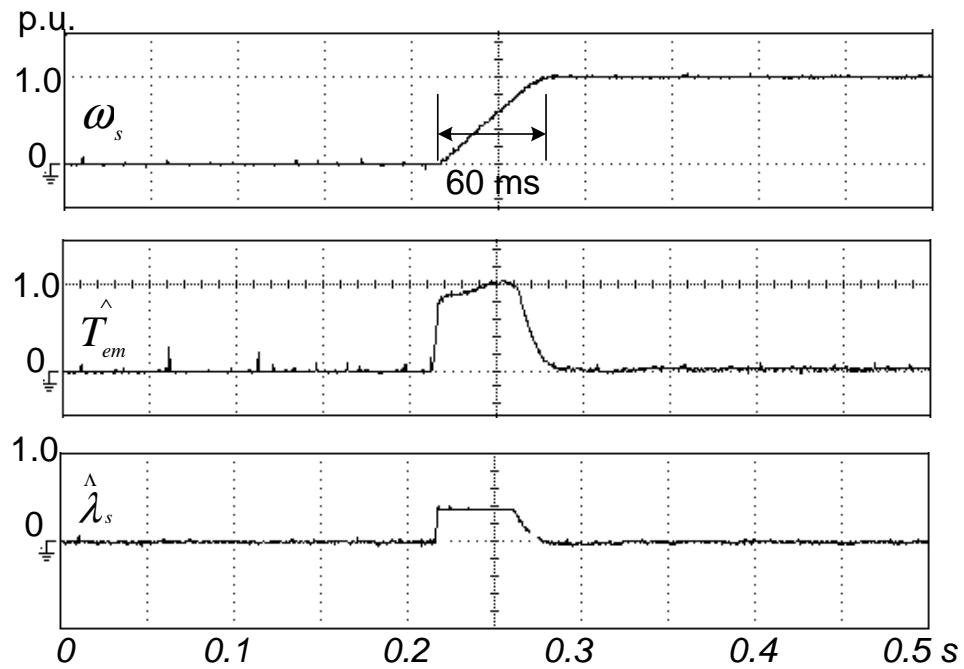


Figure 6.17: SVM based DTC: The dynamic response with step speed change in the normal range

Fig. 6.18 and Fig. 6.19 show the dynamic response for the loading torque

step change from 0.1 to 1.0 p.u., while the speed is kept at 900rpm. It is shown the building-up time of torque response for SVM based DTC (40ms) is faster than that of current control (80ms). The stator flux level for SVM based DTC is increased from 1.1 to 1.35 p.u. in SVM based DTC. The current responses are also plotted in the same figures, which show that the current magnitude for SVM based DTC is equal to that of current control. These results confirm that the current in SVM based DTC is under the MTPA control.

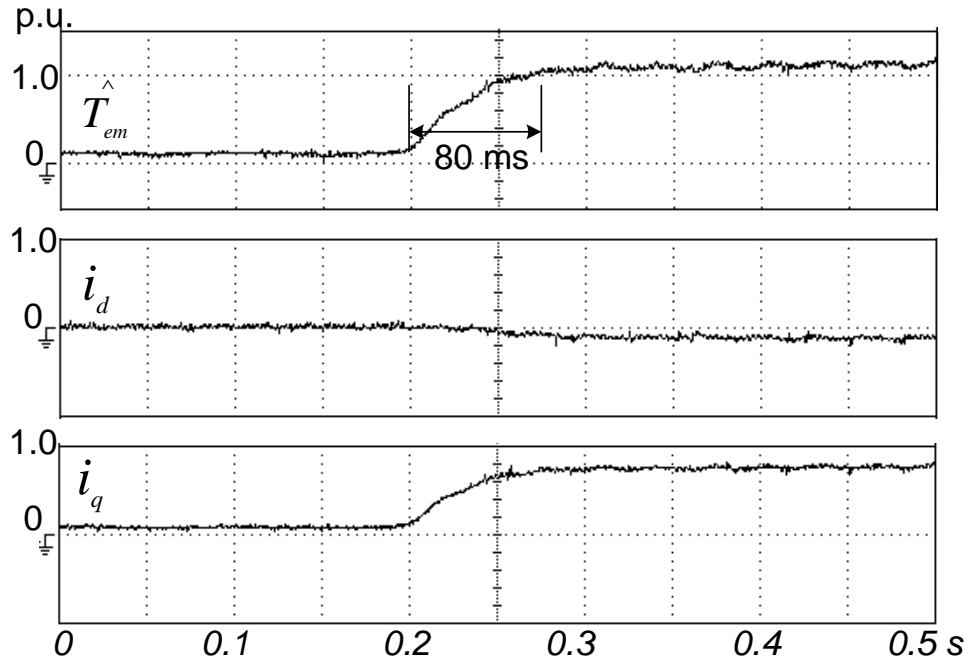


Figure 6.18: Current Control: The dynamic response with step loading torque change in constant torque speed range

From the comparison of two control schemes in the constant torque speed range, it is seen that the proposed strategy improves torque performance and the current is under control even when there is no current regulator.

To verify the effectiveness of the proposed SVM based DTC in flux-weakening range, the actual dynamic responses in two control schemes are shown in Figs. 6.20

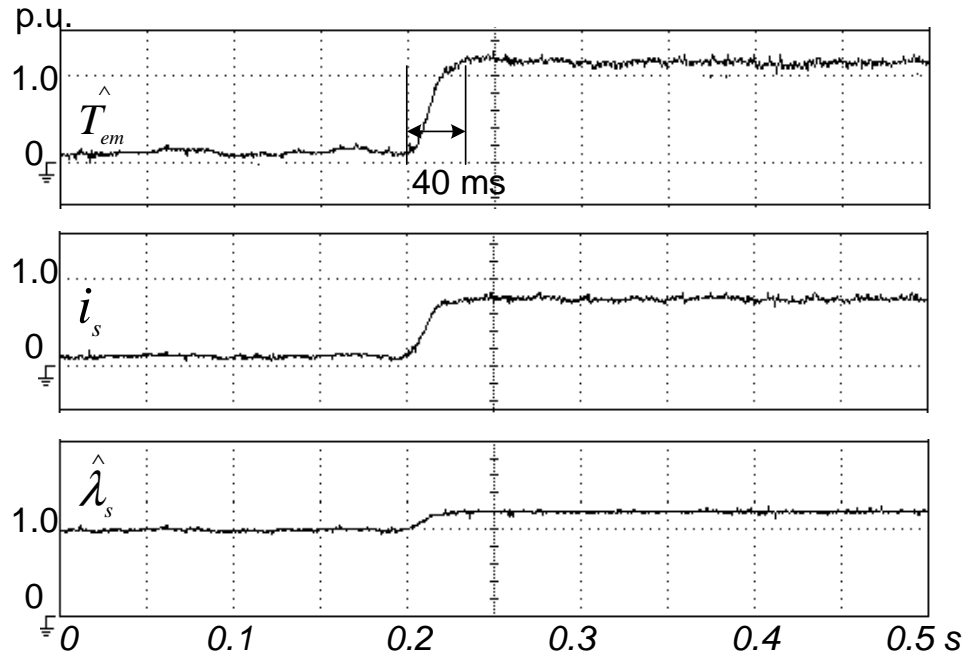


Figure 6.19: SVM based DTC: The dynamic response with step loading torque change in constant torque speed range

and 6.21, with the step speed change above the base speed. From the comparison of the speed tracking performance, it is seen that SVM based DTC provides significantly improved dynamic response. The comparison shows that torque performance of current control is deteriorated, Fig. 6.20, while the torque for SVM based DTC is still under control because of the overmodulation strategy applied in flux-weakening region. The results in the speed settling time of SVM based DTC is reduced by 35% compared with that of current control. It is noted that the flux level is reduced by 35% compared with that of current control. It is noted that the flux level is reduced from 1.0 to 0.5 p.u., when the speed is increasing from 1.0 to 2.0 p.u. in the flux-weakening range, Fig. 6.21.

Fig. 6.23 shows the flux weakening operation with a reduction and an increase in the DC link voltage with the constant speed operation at 2250rpm. The output of flux weakening controller $\hat{\lambda}_s$ is changed according to the variation of inverter

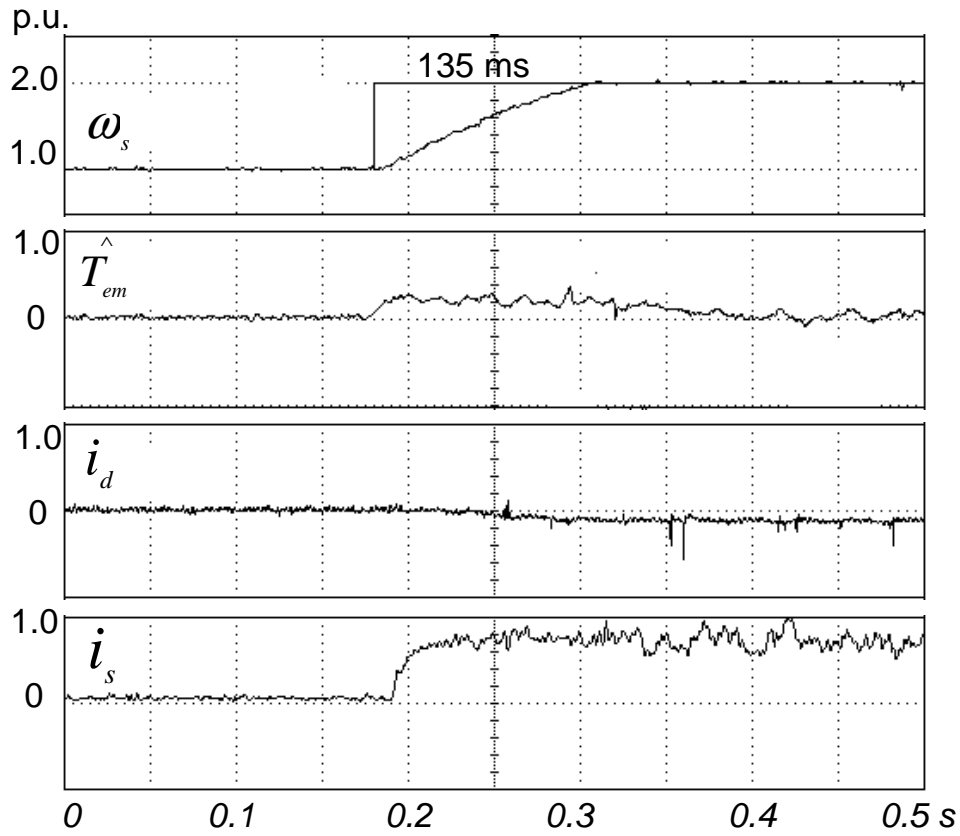


Figure 6.20: Current Control: The dynamic response with step speed change in flux-weakening range

voltage output. Even with the rapid change of DC link voltage, the proposed control scheme can adjust the stator flux reference to compensate the DC link voltage variations.

Fig. 6.22 shows the transient response of torque and flux with SVM based DTC controlled IPSMSM drive during the ramp speed change (600rpm – 2100rpm) from constant torque region to flux-weakening region. The torque and flux control are smooth during the transition of MTPA control and flux-weakening control.

The experimental results of SVM based DTC as shown in Fig. 6.24 is plotted to observe the flux and voltage variations in the overmodulation range. It shows

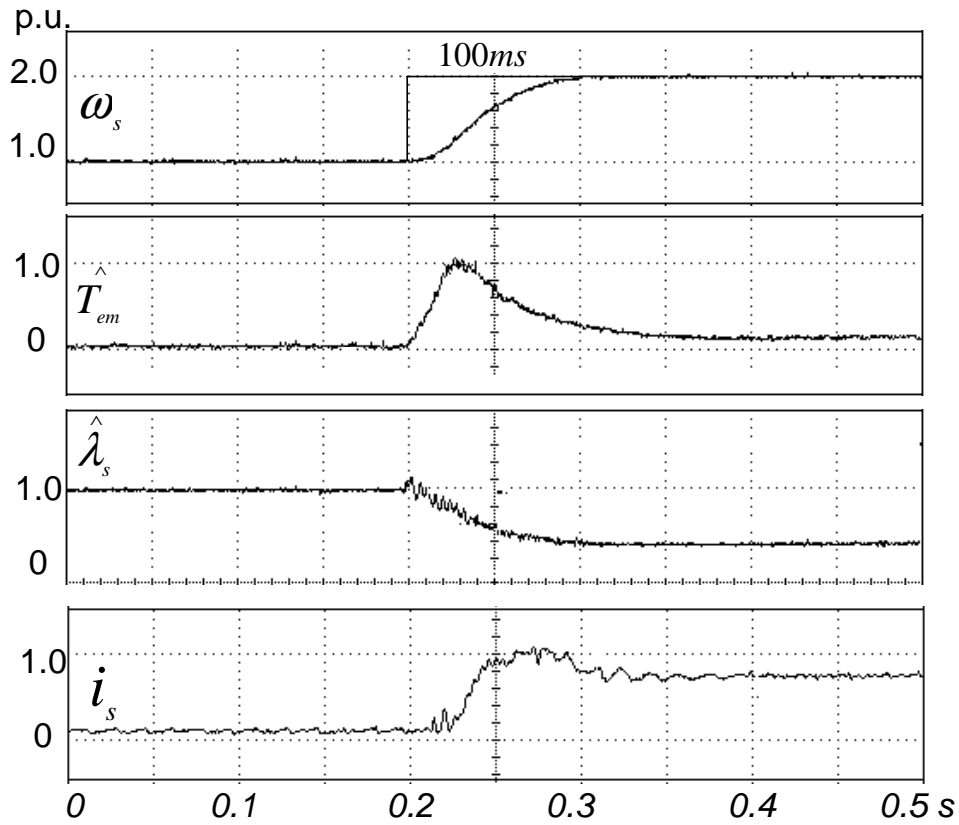


Figure 6.21: SVM based DTC: The dynamic response with step speed change in flux-weakening range

that when there is large step change in speed (from 900rpm to 1800rpm), the system automatically comes into six step mode operation to provide faster dynamic response.

Fig. 6.25 and Fig. 6.26 illustrates the operation performance under full DC link voltage (350V) in a wide speed range with respect to two control schemes: SVM based DTC and Field Oriented Current Control. As shown in Fig. 6.25, the maximum torque capability for current control scheme in constant torque region is better than SVM based DTC scheme, since with field oriented control, the current vector can be properly controlled (without the voltage saturation) to fully exploit the reluctance torque and magnet torque. However, the wide speed operation

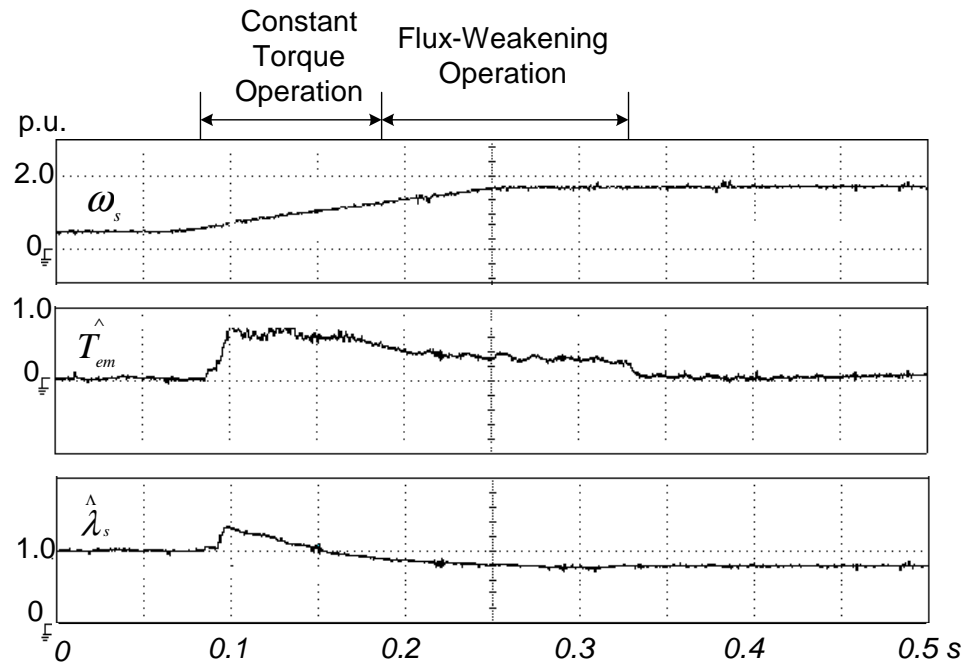


Figure 6.22: Dynamic response of the IPMSM drive system in transition from constant torque to flux-weakening regions

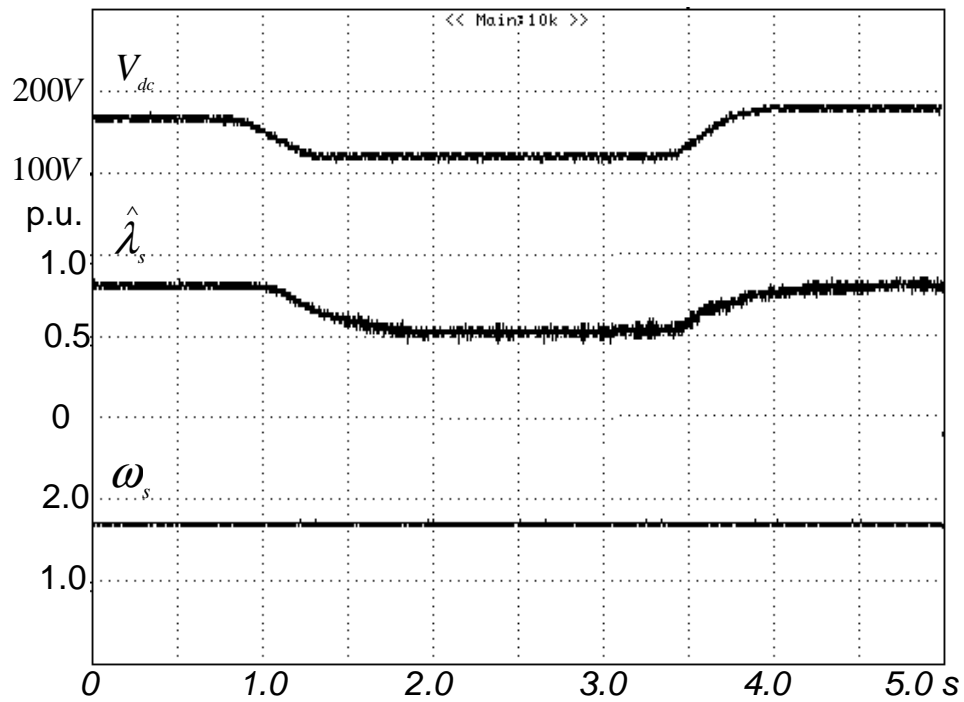


Figure 6.23: Flux Weakening Operation with the variation of DC link voltage

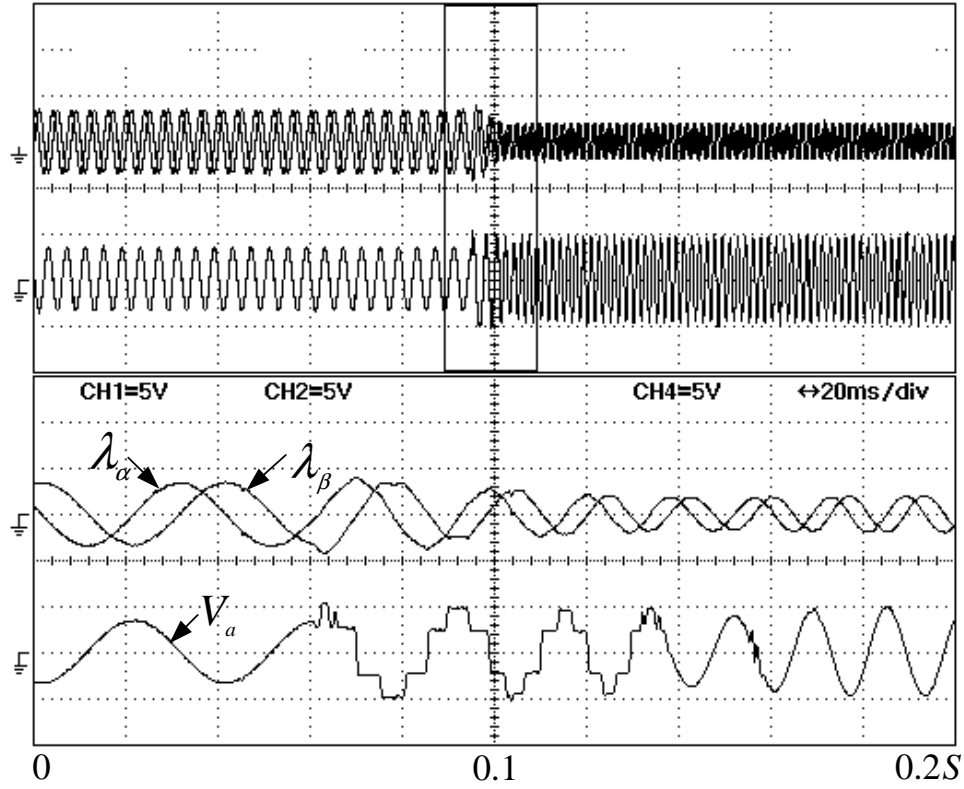


Figure 6.24: Transient performances of flux and voltage for step speed change in flux-weakening range

performance for SVM based DTC is superior than current control as shown in Fig. 6.26 because of the excellent flux-weakening control performance in the SVM based DTC scheme.

6.6 Conclusion

In this chapter, a novel control strategy for speed and torque control of interior PMSM drives has been presented and compared with traditional current vector control. The control scheme is derived from the basic direct torque control scheme; it has the advantages of constant switching frequency and reduced torque and flux ripples. The application of SVM based DTC for interior PMSM drives was inves-

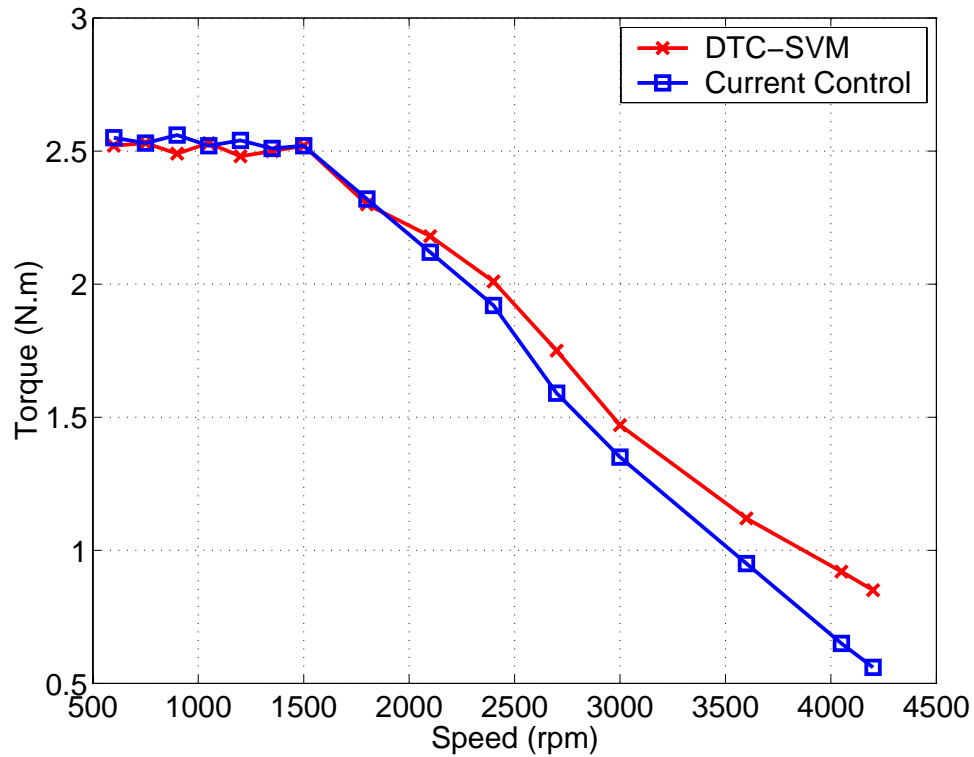


Figure 6.25: Torque performance of SVM based DTC and Current Control for a wide speed operation

igated through analysis and experimental implementation. Important conditions which are necessary for the applicability of SVM based DTC to an interior PMSM has been put forward. Compared with conventional current vector control, the new control scheme improves the dynamic response of speed and torque control over the wide-speed operation. Current regulator saturation, the worst degrading factor of torque production in the extended flux-weakening range, is eliminated.

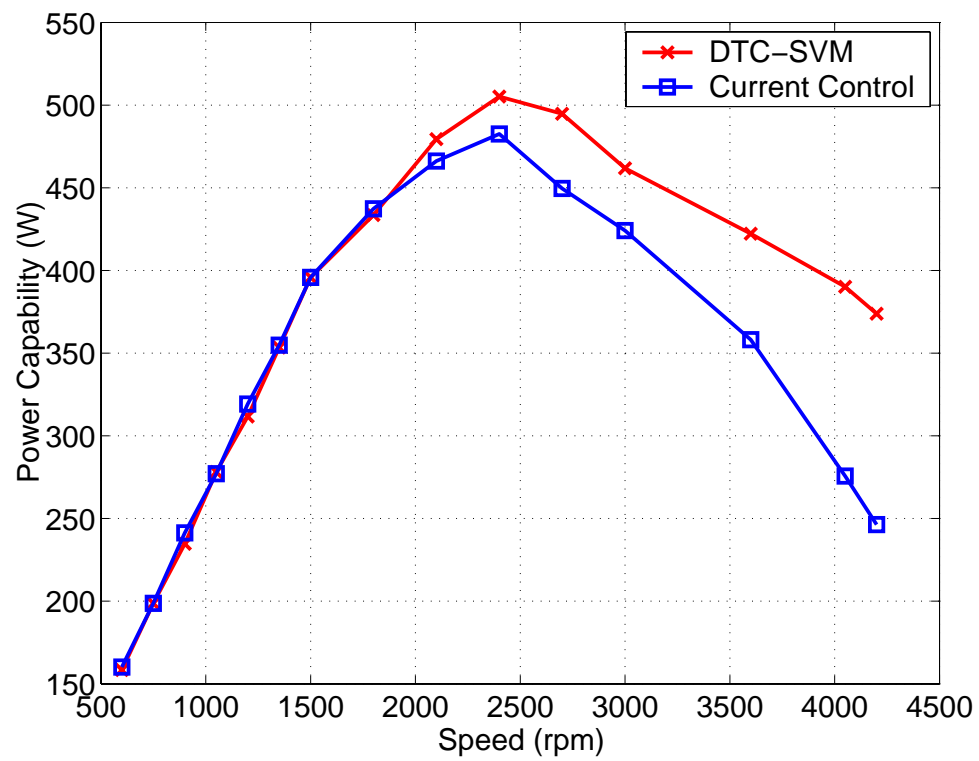


Figure 6.26: Power performance of SVM based DTC and Current Control for a wide speed operation

Chapter 7

Discussions and Conclusions

This thesis examined various aspects of design and control applied to interior PMSM drive, which required for a wide speed constant power operation. The two main topics of discussion are the design optimization of a 400W prototype interior PMSM and the control techniques to exploit the power capability of the prototype.

7.1 Discussions of Major Work

7.1.1 Analysis of constant power operation

In order to match the interior PMSM with the variable speed control system, an analysis of the effect of motor parameters on the steady state performance was presented in Chapter 2. The main purpose is to find out how the parameters affect the constant power speed range. The torque-speed characteristics under three different operating regions (current limited constant torque region, voltage and current

limit region, and voltage limited maximum power region) were introduced. Based on the analysis, the constant power speed range of an interior PMSM drive can be estimated from the motor parameters (L_d , L_q and λ_m) and voltage and current constraints. It was suggested that the constant power speed range can be theoretically extended if the interior PMSM is designed with an optimum combination of motor parameters.

In the mathematical analysis presented, the steady state performance of an interior PMSM was modelled by constant motor parameters. However, λ_m , L_d , and L_q are nonlinear functions of the machine flux level. The simplification of the interior PMSM's equivalent circuits to include only three parameters means that all electrical loss components were ignored. This included both the stator resistance, as well as hysteresis and eddy-current losses in the machine. The impact of neglecting iron losses gradually increases as the speed increases because these iron loss components increase with speed. Magnetic saturation effects were not included in the analysis. This has particular relevance for interior PMSMs with high saliency ratios for which q-axis inductance can be significantly affected by saturation. Therefore, the availability using constant motor parameters in the analysis has to be justified by following assumptions in the design procedure:

- The prototype interior PMSM was designed with small iron loss at rated speed, so ignoring these losses did not affect the major predicted trends.
- The developed design methodology was presented with the understanding

that the saturation is not dominant effect in the prototype interior PMSM.

7.1.2 Design optimization methodology

In order to design an interior PMSM with the optimum constant power speed range under certain constraints, an effective design methodology was introduced in Chapter 3. The key element of the proposed approach is the determination of motor parameters (L_d , L_q and λ_m) based on design variables (l_m , γ and α), which was developed using fitted second order RSM models instead of FEM computation. Hence the time for iterative field computation can be reduced significantly in the design procedure. These RSM models were built by central composite design with 15 sets of FEM numerical results. Motor parameters (L_d , L_q and λ_m) obtained by conventional analytical models and RSM models were compared with the numerical results by FEM. It was noted that the results by RSM models agree well with that by FEM. The residual analysis shows the fitted second-order RSM model can explain about 99% of the variability observed in the responses.

Although the overall accuracy is satisfactory in the design of the prototype interior PMSM, it has to be reminded that this is only valid when the available design area is relatively small because of a cubic CCD is used to fit the second order RSM models. The potential optimal solution could be missed by such simplifications. In order to select appropriate design area, the empirical knowledge from previous designs can be used to determine the the appropriate range of design variables.

Evolution computation is an optimization technique based on ideas of adaptation and evolution, which uses primarily real-vector coding, mutation, recombination, and selection as its primary operators. Mutation is performed by adding a gaussian distributed random value. The step size (ie. the variance of this distribution) is usually adapted during the optimization, which should keep the evolutionary process within the Evolution Window. The evolution strategy is robust and efficient to locate the global optimal area for most complex optimization problem, however the implementation of such method is complicated and it would take lots of time to develop the programming and parameter tuning work. The major objective of my thesis is to develop a systematic technique which combines the RSM methodology and optimization algorithms to design the rotor structure. Using analytical model and numerical analysis, we have concluded that the motor parameters which determine the motor performances are significantly affected by only three design variables (l_m , γ , α). Therefore, considering the simplicity of optimization work in our application, the basic GAs can fulfil this task to look for the optimal design. The FEM verifications also confirm the optimal results provided by the proposed design methodology. However, evolution computation is more suitable for the design optimization which includes more design variables, especially for the non-linear model of motor parameters.

The basic Genetic algorithms were used as the optimization technique to search for the optimum rotor structure which can realize the largest constant power speed range under voltage and current constraints. The objective function (con-

stant power speed range) was calculated from the motor parameters (L_d , L_q and λ_m), which was determined by fitted RSM models. It is important to note that the solution by GAs can be near the optimal but may not be the true optimal because not all domain of design variables have been explored. The fact is that GAs have no convergence guarantees in arbitrary problems. But they do sort out interesting areas of a space quickly and provide solution close to the global optimal. On the other hand, in this thesis work, we have only three design variables (l_m , γ and α) and the search space is $32 \times 32 \times 32$. The GAs may not be the most efficient optimization method to deal with such an simple design case. However, considering the increased design variables or larger search space in the future work, the GAs together with RSM models may show their advantages to locate the optimum area quickly.

7.1.3 Steady state tests of the prototype interior PMSM

A 400W prototype interior PMSM has been fabricated based on the optimized design described in Chapter 4. Various steady state tests of the prototype interior PMSM have been reported in Chapter 5. For open circuit and load test, the measured motor parameters have only 5% variation from those estimated from the proposed computational approaches as specified in Chapter 3 and Chapter 4. This fact validates the fitted second order RSM model to estimate the motor parameters. The tests show that the prototype motor has better torque-speed characteristics and larger wide speed range of constant power operation than commercial interior

PMSM. However, when compared with those predicted from the analysis of the steady state operation, it has to be pointed out that the experimental constant power speed range is less than the predicted one. This can be explained as the iron loss and magnetic saturation were neglected in the design procedure.

The efficiency and power factor of the prototype interior PMSM have been measured and compared with those of a commercial 400 W interior PMSM. The comparison indicates that the optimized design realizes the wide-speed constant power operation with little trade-off in its performance on the rated operation.

7.1.4 Speed and torque control by DTC-SVM

An improved control strategy for speed and torque control of interior PMSM drives using space vector modulation based on direct torque control in Chapter 6, was presented and compared with traditional current vector control. The control scheme is derived from the basic direct torque control scheme; it has the advantages of constant switching frequency and reduced torque and flux ripple. The maximum torque per ampere control and flux-weakening control using proposed control scheme was investigated through analysis and experimental implementation in the prototype interior PMSM. Important conditions which are necessary for the applicability of SVM based DTC to an interior PMSM has been put forward. Compared with conventional current vector control, the new control scheme improves the dynamic response (25% more) on speed and torque control over the wide-speed operation. However, the selection of stator flux reference level has to be based on the accu-

racy of motor parameters under different loading condition, which requires off-line measurements. Hence, it is also difficult to tune the flux weakening controller.

7.2 Major Contributions of the Thesis

- Analytical model has been developed based on equivalent circuit model of interior PMSMs, which was used to determine the influence of motor parameters and inverter power rating on motor output power capability over a wide speed range. This analysis provides design criterion to obtain optimal combination of motor parameters in order to achieve a wide speed range of constant power operation.
- A fitted second-order response surface model for the estimation of motor parameters has been established based on the central composite design of finite element computations. The developed RSM model provides an accurate description of effects of rotor geometric design of the motor parameters of interior PMSMs.
- A design methodology that combines the RSM model with the GA technique has been proposed and implemented for the design optimization of an interior PMSM to realize an optimal constant power speed range. Compared to traditional analytical methods and finite element methods, the new computational method reduce computing time and effort in estimation of motor parameters.
- An experimental method for the determination of d- and q-axis inductances

has been proposed based on the load test with rotor position feedback. The measurement of motor parameters not only validate the developed numerical computation approach, but also improves the speed and torque control performance of interior PMSMs over a wide speed range.

- The conventional current vector control of interior PMSMs has been implemented for a smooth and accurate stator current control. This method is particularly suitable for DSP based speed and torque control and leads to improved torque capability below the rated speed. It is noted that the field-weakening performance of current vector control is deteriorated because of the saturation effects of current regulator in the high speed and high current condition.
- Space vector modulation based direct torque control has been proposed to overcome the difficulties met in the current vector control. The application of SVM based DTC for the prototype interior PMSM drive has been investigated through analysis and experimental implementation. Important conditions which are necessary for the applicability of SVM based DTC in an interior PMSM has been put forward.

7.3 Suggestions for Future Research

There are many aspects relevant to permanent magnet synchronous motors that need to be explored in the future. The following suggestions are made based on the developments reported in this thesis research:

- In Chapter 2 of this thesis, the analysis of interior PMSMs for constant power operation is based on the theoretical steady state operation of lossless, linear model of interior type PMSMs. However, actual power capability is limited, especially at high speed, by motor core losses. Stator core loss has strong influence on the time harmonics of stator flux density. These harmonic fields increase as the armature current acts to reduce the magnet flux. Therefore, a numerical model to calculate the stator core loss is required for accurate prediction of the power capability of interior PMSMs over a wide speed range. The second or higher order response surface model may be used to build the empirical model of stator loss estimation based on the selected design of finite element experiments.
- In Chapter 3, motor parameters are estimated using fitted second order RSM models, which are based on geometrical variables only. However, the saturated model of motor parameters are not considered. The potential optimal design may be missed because of such simplification. Therefore, a saturated model of motor parameters is necessary for the estimation of saturation effect due to armature reaction. More design variables including the armature current can be considered in the fitted RSM models.
- The idea of hybrid optimization method may be used in the similar research. We can start the search using a genetic algorithm to sort out the interesting peaks in the problem. Once the GA finds out the best regions, then a locally convergent scheme can be used to climb the local peaks. In this way, we can

combine the globality and parallelism of the GA with the more convergent method by the local technique.

- In the proposed space vector modulation based direct torque control of interior PMSM presented in Chapter 6, the stator flux linkage is selected to realize the maximum output torque with minimum input armature current. The selection is actually an off-line calculation based on the motor parameters, which is seriously parameter dependent and may not result in an ideal control performance over a wide speed range. The intelligent optimal control theory may be applied in the control algorithms to select the stator flux linkage with on-line calculations.

Reference

- [1] J. F. Gieras and M. Wing, *Permanent Magnet Motor Technology (Design and Application)*. Marcel. Dekker, Inc, second edition, revised and expanded ed., 2002.
- [2] P. Pillay and R. Krisnan, “Modeling, simulation, and analysis of permanent magnet motor drives,” *IEEE Trans. on Industry Application*, vol. IA-25, pp. 265–279, March/April 1989.
- [3] T.-S. Low, M. A. Jabbar, and M. A. Rahman, “Permanent-magnet motors for brushless operation,” *IEEE Transactions on Industry Applications*, vol. 26, pp. 124–129, Jan/Feb 1990.
- [4] T. M. Jahns, “Motion control with permanent-magnet ac machines,” *Proceedings of The IEEE*, vol. 82, pp. 1241–1252, August 1994.
- [5] G. R. Slemon, “Electrical machines for variable-frequency drives,” *Proceedings of The IEEE*, vol. 82, pp. 1123–1139, August 1994.
- [6] M. Satoh, M. Tomita, and S. Kanedo, “Comparison between spm motors and ipm motors for compressors of air-conditioners,” *IPEC, Tokyo*, pp. 1286–1289, 2000.

- [7] T. M. Jahns, "Interior permanent-magnet synchronous motors for adjustable-speed drives," *IEEE Transactions on Industry Application*, vol. IA-22, pp. 738–746, July/August 1986.
- [8] G. R. Slemon, *Electric Machines and Drives*. Addison Wesley, 1992.
- [9] T. J. E. Miller, *Brushless permanent-magnet and reluctance motor drive*. Oxford, London: Claredon Press, 1989.
- [10] P. C. Sen, *Principles of electric machines and power electronics*. New York: J. Wiley and Sons, second ed., 1997.
- [11] R. Krishnan, *Electric Motor Drives: Modeling, Analysis, and Control*. Prentice Hall, 2001.
- [12] B. Stumberger, A. Hamler, M. Trlep, and M. Jesenik, "Analysis of interior permanent magnet synchronous motor designed for flux weakening operation," *IEEE Tranaction on Magnetics*, vol. 37, pp. 3644–3647, September 2001.
- [13] T. M. Jahns, "Flux-weakening regime operation of an interior permanent-magnet synchronous motor drive," *IEEE Transaction on Industry Application*, vol. IA-23, pp. 681–689, July/August 1987.
- [14] R. F. Schiferl and T. A. Lipo, "Power capability of salient pole permanent magnet synchronous motors in variable speed drive applications," *IEEE Transactions on Industry Applications*, vol. 26, pp. 115–123, January/February 1990.
- [15] D. M. Ionel, J. F. Eastham, T. J. E. Miller, and E. Demeter, "Design considerations for pm synchronous motors for flux weakening applications," *Inter-*

- national Conference on Electrical Machines and Drives*, no. 444, pp. 371–375, 1997.
- [16] W. L. Soong, D. A. Staton, and T. J. E. Miller, “Design of a new axially-laminated interior permanent magnet motor,” *IEEE Transaction on Industry Application*, vol. 31, pp. 358–367, Mar/Apr 1995.
- [17] D. M. Ionel, J. F. Eastham, and T. Betzer, “Finite element analysis of a novel brushless dc motor with flux barriers,” *IEEE Transacion of Magnetics*, vol. 31, pp. 3749–3751, November 1995.
- [18] N. Bianchi, S. Bolognani, and B. J. Chalmers, “Salient-rotor pm synchronous motors for an extended flux-weakening operation range,” *IEEE Transaction on Industry Application*, vol. 36, pp. 1118–1125, July/August 2000.
- [19] G. R. Slemon, “On the design of high-performance surface-mounted pm motors,” *IEEE Transaction on Industry Application*, vol. 30, pp. 134–140, January 1994.
- [20] G. R. Slemon and X. Liu, “Modelling and design optimization of permanent magnet motors,” *Electric Machines and Power Systems*, vol. 20, pp. 71–92, 1992.
- [21] B. P. Panigrahi and K. C. Patra, “Design of a permanent magnet synchronous motor,” *Electric Machine and Power System*, vol. 27, pp. 771–779, 1999.
- [22] L. Qinghua, M. A. Jabbar, and A. M. Khambadkone, “Design optimisation of wide-speed permanent magnet synchronous motors,” in *Proceedings of Inter-*

- national Conference on Power Electronics, Machines and Drives*, (Bath, UK), pp. 404–408, April 2002.
- [23] L. Qinghua, M. A. Jabbar, and A. M. Khambadkone, “Design optimisation of interior permanent magnet synchronous motors for wide-speed operation,” in *Proceedings of The 4th IEEE International Conference on Power Electronics and Drive Systems*, (Bali, Indonesia), pp. 475–478, October 2001.
- [24] L. Xu and L. Ye, “A new design concept of permanent magnet machine for flux weakening operation,” *IEEE Transaction on Industry Application*, vol. 31, pp. 373–378, March/April 1995.
- [25] J. C. Teixeira, C. Chillet, and J. P. Yonnet, “Structure comparison of buried permanent magnet synchronous motors for flux weakening operation,” *International Conference on Electrical Machines and Drives*, pp. 365–370, 1993.
- [26] M. Hippner and R. G. Harley, “Looking for an optimal rotor for high speed permanent magnet synchronous machine,” *Industry Applications Society Annual Meeting*, vol. 1, pp. 265–270, 1992.
- [27] Z. P. M. A. Rahman and M. A. Jabbar, “Field circuit analysis of permanent magnet synchronous motors,” *IEEE Transaction on Magnetism*, vol. 30, pp. 1350–1359, July 1994.
- [28] O. A. Mohammed and G. F. Uler, “A hybrid technique for the optimal design of electromagnetic devices using direct search and genetic algorithms,” *IEEE Transaction on Magnetism*, vol. 33, pp. 1892–1895, May 1997.

- [29] A. Gottvald, K. Preis, C. Magele, O. Biro, and A. Savini, "Global optimization methods for computational electromagnetics," *IEEE Transaction on Magnetics*, vol. 28, pp. 1537–1540, Mar 1992.
- [30] N. Bianchi and S. Bolognani, "Brushless dc motor design: an optimization procedure using genetic algorithms," in *Proceedings of IEE Electrical machines and drives conference*, (Cambridge, UK), pp. 16–20, IEE, September 1997.
- [31] G. F. Uler, O. A. Mohammed, and C.-S. Koh, "Utilizing genetic algorithms for the optimal design of electromagnetic devices," *IEEE Transaction on Magnetics*, vol. 30, pp. 4296–4298, November 1994.
- [32] N. Bianchi and S. Bolonani, "Design optimization of electric motors by genetic algorithms," *IEE Proceeding on Electric and Power Application*, vol. 145, pp. 475–483, September 1998.
- [33] T. Renyuan and Y. Shiyoun, "Combined strategy of improved simulated annealing and genetic algorithm for inverse problem," in *10th Conference on the Computation of Electromagnetic Fields COMPUMAG'95*, (Berlin, Germany), pp. 196–197, 1995.
- [34] M. Kasper, "Shape optimization of by evolution strategy," *IEEE Transaction on Magnetics*, vol. 28, pp. 1556–1560, Mar 1992.
- [35] T. Higuchi, J. Oyama, and E. Yamada, "Optimization procedure of surface pm synchronous motors," *IEEE Transaction on Magnetics*, vol. 33, pp. 1943–1946, March 1997.

- [36] C. Schatzer and A. Binder, "Design optimization of a high-speed permanent magnet machine with the vekopt algorithms," *Industry Application Conference, IEEE*, vol. 1, pp. 439–444, 2000.
- [37] J. K. Lahteenmaki, "Optimization of high-speed motors using a genetic algorithm," *International Conference on Electric Machines and Drives, IEE*, vol. 1, pp. 26–30, September 1997.
- [38] R. H. Myers and D. C. Montgomery, *Response Surface Methodology, Press and Product Optimization Using Designed Experiments*. JOHN WILEY SONS, INCQ, 2002.
- [39] A. I. Khuri and J. A. Cornell, *Response Surfaces, Designs and Analysis*. Marcel Dekker, Inc, 1996.
- [40] R. Rong and D. A. Lowther, "Applying response surface methodology in the design and optimization of electromagnetic devices," *IEEE Transaction on Magnetism*, vol. 33, pp. 1916–1919, March 1997.
- [41] F. Gillon and P. Brochet, "Screening and response surface method applied to the numerical optimization of electromagnetic devices," *IEEE Transaction on Magnetism*, vol. 36, pp. 1163–1167, July 2000.
- [42] G. X. Ke, T. S. Low, L. Z. Jie, and C. S. Xin, "Robust design for torque optimization using response surface methodology," *IEEE Transaction on Magnetism*, vol. 38, pp. 1141–1144, March 2002.

- [43] Y. Fujishima, S. Wakao, A. Yamashita, and T. Katsuta, "Design optimization of a permanent magnet synchronous motor by the response surface methodology," *Journal of Applied Physics*, vol. 91, pp. 8305–8307, May 2002.
- [44] D.-H. Cho, H.-K. Jung, and D.-J. Sim, "Multiobjective optimal design of interior permanent magnet synchronous motors considering improved core loss formula," *IEEE Transaction on Energy Conversion*, vol. 14, pp. 1347–1352, December 1999.
- [45] B. K. Bose, "A high-performance inverter-fed drive system of an interior pm synchronous machine," *IEEE Transaction on Industry Application*, vol. 24, pp. 987–997, Nov/Dec 1988.
- [46] A. B. Kulkarni and M. Ehsani, "A novel position sensor elimination technique for the interior pm synchronous motor drive," *IEEE IAS Annual Meeting Record*, pp. 773–779, 1989.
- [47] G. R. Slemon, "Operating limits of inverter-driven permanent magnet motor drives," *IEEE Transaction on Industry Applications*, vol. IA-23, pp. 327–332, March/April 1987.
- [48] M. P. Kaxmeirkowski and M. A. Dzieaniakowski, "Novel current regulator for vsi-pwm inverters," *Proceed of European Power Electronics Conference, Aachen*, 1989.

- [49] M. N. Uddin, T. S. Radwan, G. H. George, and M. A. Rahman, "Performance of current controllers for vsi-fed ipmsm drives," *IEEE Transaction on Industry Applications*, vol. 36, pp. 1531–1538, November/December 2000.
- [50] S. Morimoto, Y. Takeda, and T. Hirasaka, "Current phase control methods for permanent magnet synchronous motors," *IEEE Trans. Power Electronics*, vol. 5, pp. 133–139, Apr. 1990.
- [51] S. Morimoto, M. Sanada, and Y. Takeda, "Wide-speed operation of interior permanent magnet synchronous motors with high-performance current regulator," *IEEE Trans. Ind. Applicat.*, vol. 30, pp. 920–926, July/Aug 1994.
- [52] J. M. Kim and S. K. Sul, "Speed control of interior permanent magnet synchronous motor drive for the flux weakening operation," *IEEE Transaction on Industry Applications*, vol. 33, pp. 43–48, January/February 1997.
- [53] B. J. Chalmers, "Influence of saturation in brushless permanent-magnet motor drives," *IEE Proc.*, vol. 139, pp. 51–52, Jan 1992.
- [54] B. J. Chalmers, R. Akmes, and L. Musada, "Validation of procedure for prediction of field-weakening performance of brushless synchronous machines," *Proc. ICEM 1998, Istanbul, Turkey*, vol. 1, pp. 320–323, 1998.
- [55] E. C. Lovelance, T. M. Jahns, and J. H. Lang, "Impact of saturation and inverter cost on interior pm synchronous machine drive optimization," *IEEE Trans. Ind. Applicat.*, vol. 36, pp. 723–729, MAY/JUNE 2000.

- [56] C. Mademlis and V. G. Agelidis, "On considering magnetic saturation with maximum torque to current control in interior permanent magnet synchronous motor drives," *IEEE Trans. on Energy Conversion*, vol. 16, pp. 246–252, September 2001.
- [57] J. H. Song, J. M. Kim, and S. K. Sul, "A new robust spmsm control to parameter variations in flux weakening region," *IEEE IECON*, vol. 2, pp. 1193–1198, 1996.
- [58] H. Le-Huy, K. Slimani, and P. Viarouge, "A predictive current controller for synchronous motor drives," *Proceeding of EPE Conf.*, vol. 2, pp. 114–119, 1991.
- [59] A. Verl and M. Bodson, "Torque maximization for permanent magnet synchronous motors," *IEEE Trans. Contr. Syst. Technol.*, vol. 6, pp. 740–745, Nov. 1998.
- [60] E. Cerruo, A. Consoli, A. Raciti, and A. Testa, "Adaptive fuzzy control of high performance motion systems," *IEEE Proceeding of Industrial Electronics Conf. (IECON)*, pp. 88–94, 1992.
- [61] Z. Q. Zhu, Y. S. Chen, and D. Howe, "Online optimal flux-weakening control of permanent-magnet brushless ac drives," *IEEE Trans. on Ind. Applicat*, vol. 36, pp. 1661–1668, Nov/Dec 2000.

- [62] S. Henneberger, U. Pahner, and R. Belmans, "Computation of a highly saturated permanent magnet synchronous motor for a hybrid electric vehicle," *IEEE Trans. Magnetics*, vol. 33, Sept 1997.
- [63] R. B. Colby and D. W. Novotny, "An efficiency-optimizing permanent magnet synchronous motor drive," *IEEE Trans. Industry Applications*, vol. 24, pp. 462–469, May/June 1988.
- [64] J.-J. Chen and K.-P. Chin, "Minimum copper loss flux-weakening control of surface mounted permanent magnet synchronous motors," *IEEE Transactions on Power Electronics*, vol. 18, pp. 929–936, July 2003.
- [65] S. Morimoto, T. Ueno, and M. Sanada, "Effects and compensation of magnetic saturation in permanent magnet synchronous motor drives," *IEEE IAS Annual Meeting*, vol. 3, no. 6, pp. 59–64, 1993.
- [66] R. B. Sepe and J. H. Lang, "Real-time adaptive control of the permanent magnet synchronous motor," *IEEE Trans. Ind. Applicat*, vol. 27, pp. 706–714, July/Aug 1991.
- [67] J. K. Seok and S.-K. Sul, "A new overmodulation strategy for induction motor drive using space vector pwm," *Proc. IEEE APEC*, vol. 1, pp. 211–216, Mar 1995.
- [68] J. Shi and Y. S. Lu, "Field-weakening operation of cylindrical permanent-magnet motors," *Proc. IEEE Int. Conf. Contr. Applicat*, pp. 864–869, Sept. 1996.

- [69] L. Zhong, M. F. Rahman, W. Y. Hu, and K. W. Lim, "Analysis of direct torque control in permanent magnet synchronous motor drives," *IEEE Transaction on Power Electronics*, vol. 12, pp. 528–536, May 1997.
- [70] M. F. Rahman, L. Zhong, and K. W. Lim, "A direct torque-controlled interior permanent magnet synchronous motor drive incorporating field weakening," *IEEE Transaction on Industry Application*, vol. 34, pp. 1246–1253, November/December 1998.
- [71] J. Faiz and S. H. Mohseni-Zonoozi, "A novel technique for estimation and control of stator flux of a salient-pole pmsm in dtc method based on mtpf," *IEEE Transaction on Industrial Electronics*, vol. 50, pp. 262–271, April 2003.
- [72] I. Takahashi and T. Noguchi, "A new quick-response and high-efficiency control strategy of an induction motor," *IEEE Transaction on Industry Application*, vol. 22, pp. 820–827, September/October 1986.
- [73] M. Depenbrock, "Direct self-controlled (dsc) of inverter fed induction machine," *IEEE Transaction on Power Electronics*, vol. 3, pp. 420–429, October 1988.
- [74] D. Casadei, F. Profumo, G. Serra, and A. Tani, "Foc and dtc: Two viable scheme for induction motors torque control," *IEEE Transaction on Power Electronics*, vol. 17, pp. 779–787, September 2002.
- [75] P. Vas, *Sensorless Vector and Direct Torque Control*. Oxford University Press, 1998.

- [76] C. Martins, X. Roboam, T. A. Meynard, and A. S. Carylho, "Switching frequency imposition and ripple reduction in dtc drives by using a multilevel converter," *IEEE Transaction on Power Electronics*, vol. 17, March 2002.
- [77] C. Lascu, I. Boldea, and F. Blaabjerg, "A modified direct torque control for induction motor sensorless drive," *IEEE Transaction on Industry Application*, vol. 36, pp. 122–130, Jan/Feb 2000.
- [78] Y. S. Lai and J. H. Chen, "A new approach of induction motor drives for constant inverter switching frequency and torque ripple reduction," *IEEE Transaction on Energy Conversion*, vol. 16, pp. 220–227, September 2001.
- [79] C. E. Moucary, E. Mendes, and A. Razeq, "Decoupled direct control for pwm inverter-fed induction motor drives," *IEEE Transaction on Industry Applications*, vol. 38, pp. 1307–1315, September 2002.
- [80] D. Novotny and T. Lipo, *Vector control and dynamics of AC drives*. London: Clarendon Press, 1996.
- [81] L. W. Matsch and J. D. Morgan, *Electromagnetic and Electromechanical Machines*. John Wiley and Sons, thrid ed., 1986.
- [82] T. Sebastian, G. R. Slemon, and M. A. Rahman, "Modelling of permanent magnet synchronous motors," *IEEE Transaction on Magnetics*, vol. Mag-22, pp. 1069–1071, September 1986.

- [83] M. A. Rahman and A. M. Osheiba, "Performance of large line-start permanent magnet synchronous motors," *IEEE Transaction on Energy Conversion*, vol. 5, pp. 211–217, March 1990.
- [84] P. C. Krause, O. Wasynczuk, and S. D. Sudhoff, *Analysis of Electric Machinery and Drive Systems*. IEEE Press: Wiley-Interscience, second ed., 2002.
- [85] T. Sebastian, G. R. Slemon, and M. A. Rahman, "Design consideration for variable speed permanent magnet motors," *Proceedings, International Conference on Electrical Machines*, pp. 1099–1102, September 1986.
- [86] D. E. Goldberg, *Genetic Algorithms in Search, Optimization and Machine Learning*. MA: Addison Wesley, 1989.
- [87] L. Tang, L. Zhong, M. F. Rahman, and Y. Hu, "An investigation of a modified direct torque control strategy for flux and torque ripple reduction for induction machine drive system with fix switching frequency," in *Conf. Rec. IAS'02, 37th IEEE IAS Annual Meeting*, (Pittsburgh, USA), 13-18 Oct. 2002.
- [88] M. Fu and L. Xu, "A sensorless direct torque control technique for permanent magnet synchronous motors," in *Industry Applications Conference, 1999. Thirty-Fourth IAS Annual Meeting. Conference Record of the 1999 IEEE*, vol. 1, pp. 159–164, 3-7 Oct 1999.
- [89] L. Tang, L. Zhang, M. F. Rahman, and Y. Hu, "A novel direct torque controlled interior permanent magnet synchronous machine drive with low ripple

- in flux and torque and fixed switching frequency,” *Power Electronics, IEEE Transactions on*, vol. 2, pp. 346–354, March 2004.
- [90] A. Tripathi, A. M. Khambadkone, and S. K. Panda, “Predictive stator flux control with overmodulation and dynamic torque control at constant switching frequency in ac drives,” in *Conf. Rec. IECON’02*, pp. 1219–1224, Nov 30– Dec 4 2002.
- [91] L. Qinghua, A. M. Khambadkone, and M. A. Jabbar, “Direct flux control of interior permanent magnet synchronous motors for wide-speed operation,” in *Power Electronics and Drive Systems, 2003. PEDS 2003. The Fifth International Conference on*, vol. 2, pp. 1680 – 1685, NOV. 2003.
- [92] A. M. Khambadkone and J. Holtz, “Compensated synchronous pi current controller in overmodulation range and six-step operation of space-vector-modulation-based vector-controlled drives,” *IEEE Transaction on Industrial Electronics*, vol. 49, pp. 574–579, June 2002.

Appendix A

Design Details for The Prototype Interior PMSM

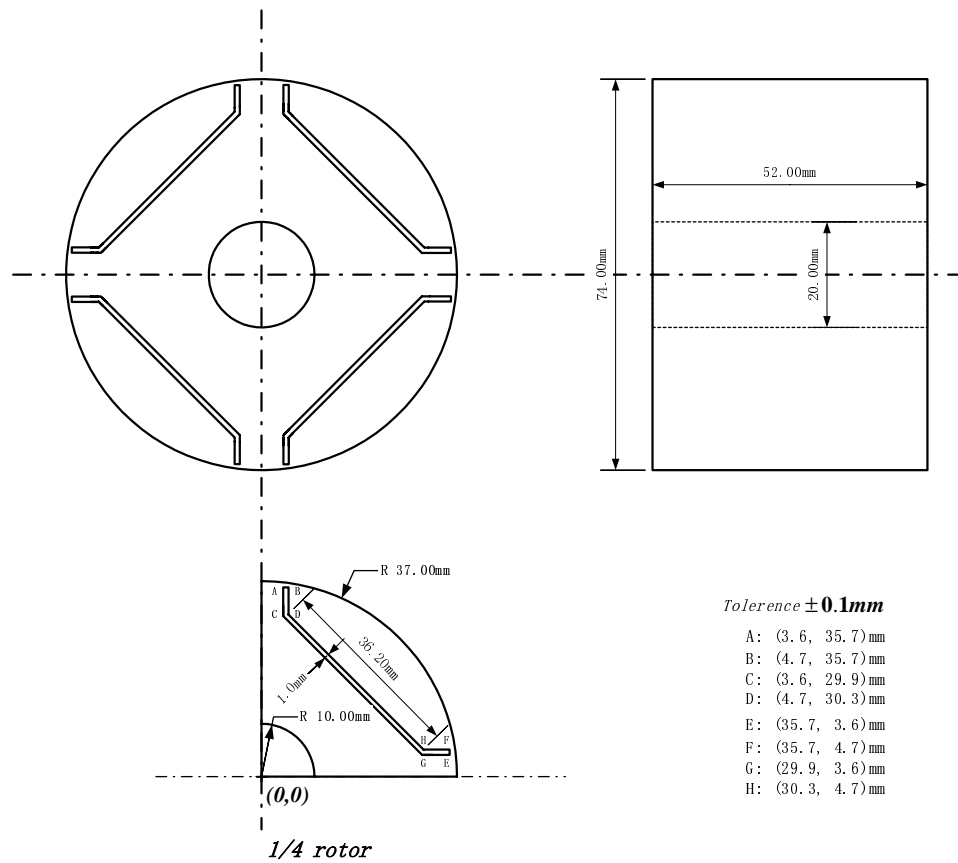
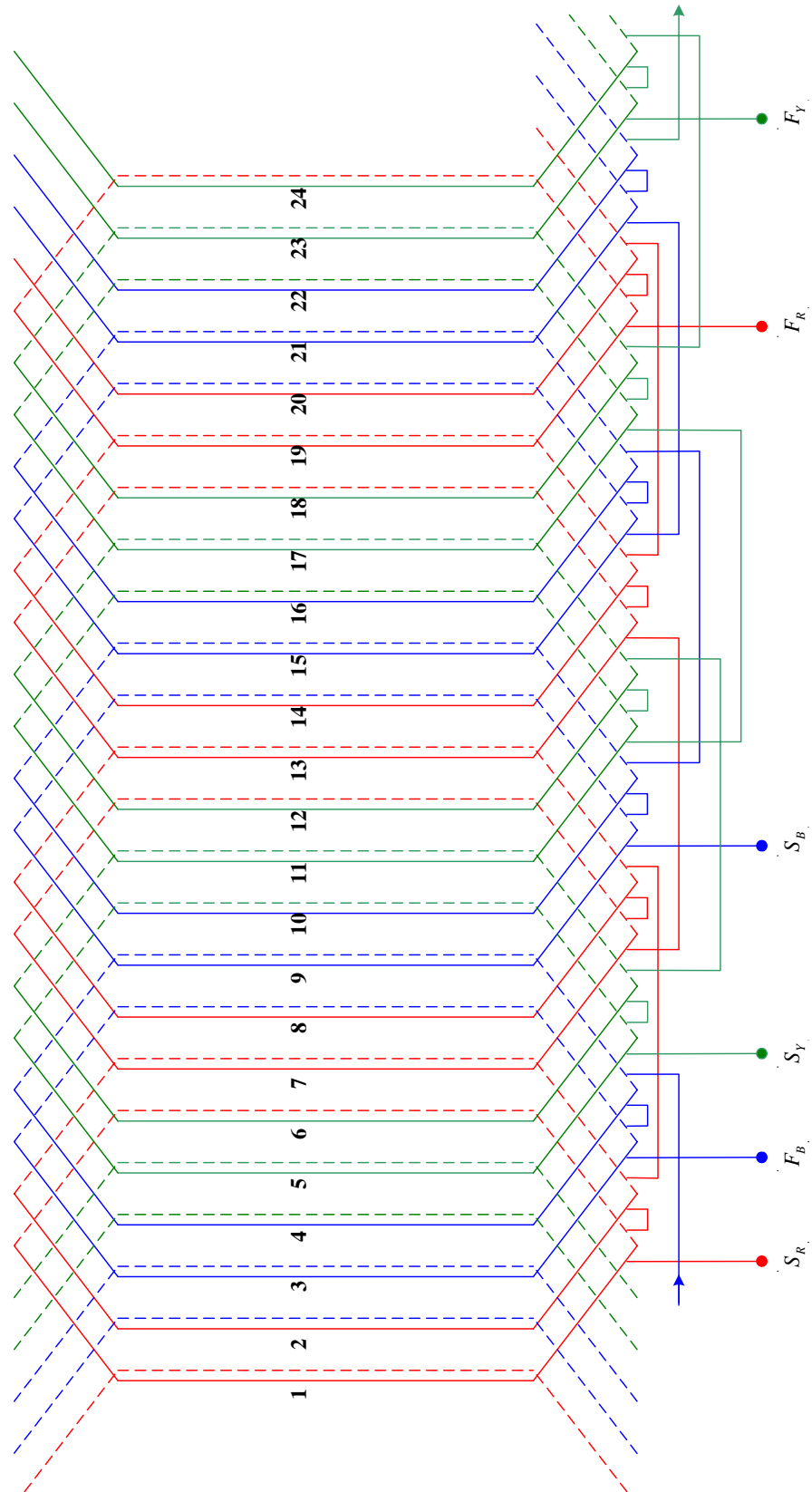
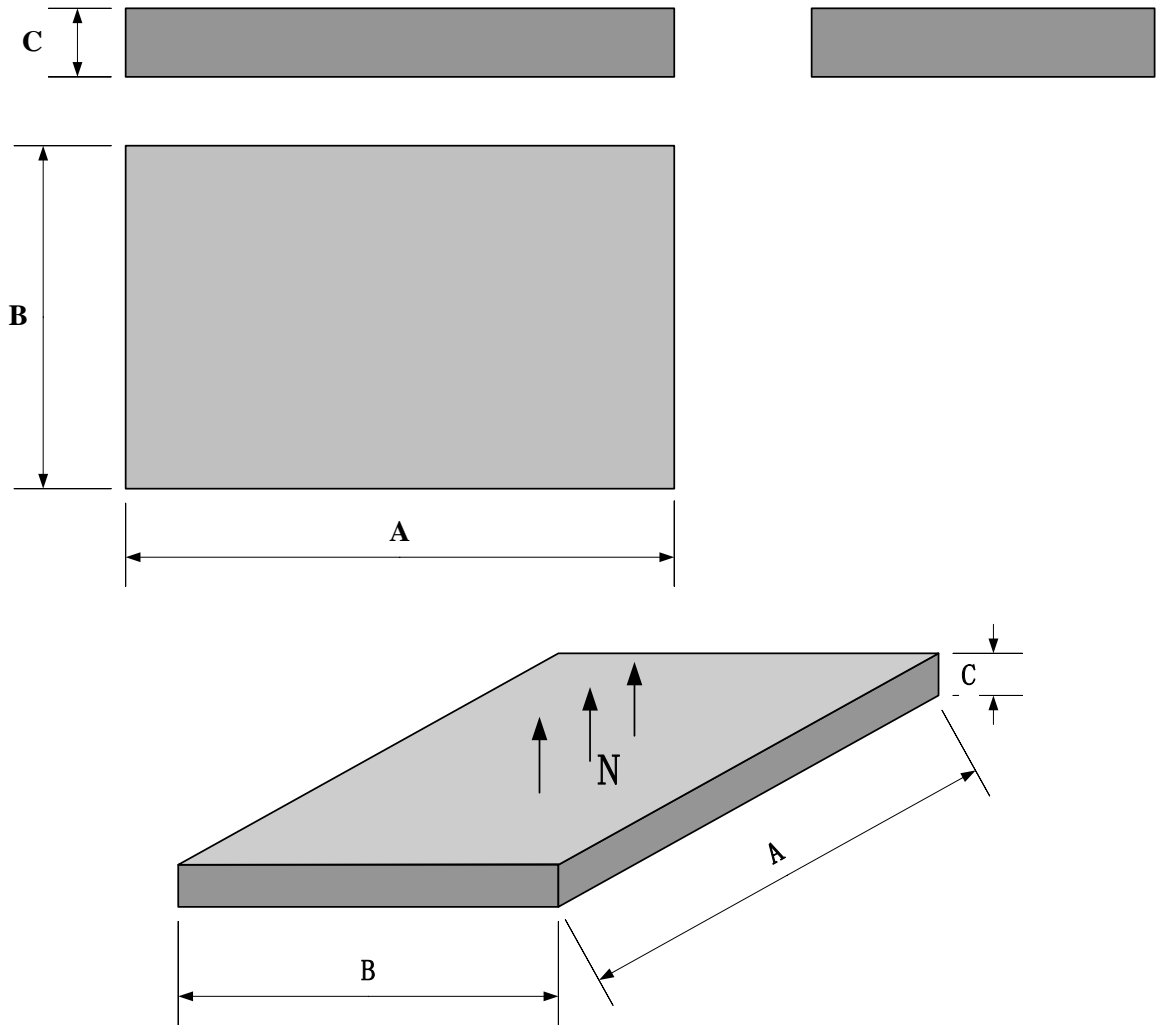


Figure A.1: Rotor mechanical design drawing



**3 phase, 24 slots, 4 pole,
Double Layer Lap Winding**

Figure A.2: Stator winding distribution



Block Magnet $\pm 0.1\text{mm}$

Description	A	B	C
Bonded NdFeB	52 mm	36.2 mm	1.0 mm

Specifications

Residual flux density	Br	> 0.9 Tesla
Coercive force	Hcb	> 450 KA/m
Maximum energy product	(BH)max	> 80 KJ/m ³
Max. operating temperature	(°C)	> 150

Figure A.3: Magnet design specification

Appendix B

Additional Experimental Data

**Table D. 1 Experimental Data for Constant Current Operation
under Full DC Link Voltage**

YASKAWA					Prototype			
speed	Vac	Ia	Input Power	Torque	Vac	Ia	Input Power	Torque
rpm	V	A	W	N.m	V	A	W	N.m
600	136.9	1.92	226.6	2.58	136.9	1.92	236.6	2.48
750	150	1.92	273.5	2.57	150	1.92	283.5	2.45
900	161.6	1.92	329.6	2.6	161.6	1.92	319.6	2.43
1050	172.3	1.92	375.5	2.57	172.3	1.92	365.5	2.45
1200	182.5	1.92	420	2.59	182.5	1.92	410	2.45
1350	192.2	1.92	467.3	2.59	192.2	1.92	457.3	2.48
1500	203.2	1.92	505	2.6	203.2	1.92	497	2.52
1800	196.5	1.92	548	2.32	204.5	1.92	538	2.3
2100	193.5	1.92	578.3	2.02	203.5	1.92	588.3	2.18
2400	196.5	1.92	602.5	1.72	203.5	1.92	622.5	2.01
2700	195.5	1.92	598.3	1.39	201.5	1.92	608.3	1.75
3000	193.5	1.92	572.6	1.15	196.5	1.92	588.6	1.47
3600	197.5	1.92	512.3	0.75	197.5	1.92	578.3	1.12
4050	196.5	1.92	447	0.45	196.5	1.92	567	0.92
4200	197.5	1.92	395.3	0.36	197.5	1.92	555.3	0.85

**Table D. 2 Experimental Data for Constant Current Operation
under 75% Full DC Link Voltage**

YASKAWA					Prototype			
speed	Vac	Ia	Input Power	Torque	Vac	Ia	Input Power	Torque
rpm	V	A	W	N.m	V	A	W	N.m
450	116.5	1.92	204.2	2.56	106.5	1.92	195.5	2.48
600	135	1.92	262.1	2.59	125	1.92	247.5	2.45
750	150.2	1.92	313.6	2.57	140.2	1.92	295.6	2.47
900	165.1	1.92	358.7	2.6	155.1	1.92	345	2.45
1050	163.6	1.92	380	2.39	163.6	1.92	390	2.46
1200	162.3	1.92	390.3	2.25	162.3	1.92	405.3	2.31
1500	163.6	1.92	419.6	1.93	163.6	1.92	425.6	2.13
1800	167.4	1.92	415.6	1.65	167.4	1.92	445.6	1.86
2100	163	1.92	382.5	1.29	163	1.92	424.5	1.56
2400	165.4	1.92	358.6	1.08	165.4	1.92	408.6	1.33
2700	163.9	1.92	325.4	0.79	163.9	1.92	385.4	1.01
3000	168.4	1.92	293.5	0.52	168.4	1.92	353.5	0.71
3300	169.3	1.92	255.2	0.24	169.3	1.92	305.2	0.46
3600					167.8	1.92	275.7	0.28

**Table D. 3 Experimental Data for Constant Current Operation
under 50% Full DC Link Voltage**

YASKAWA					Prototype			
speed	Vac	Ia	Input Power	Torque	Vac	Ia	Input Power	Torque
rpm	V	A	W	N.m	V	A	W	N.m
100	75.5	1.92	79.5	2.55	83.5	1.92	77.6	2.43
200	85.6	1.92	113.5	2.52	94.7	1.92	112.7	2.44
300	93.7	1.92	145.3	2.56	102.9	1.92	146	2.42
400	102.5	1.92	180.5	2.5	113.6	1.92	181.6	2.46
500	105.3	1.92	205.6	2.46	123.8	1.92	212.3	2.45
600	109.5	1.92	230.5	2.36	128.5	1.92	239.1	2.46
700	118.3	1.92	258.5	2.25	131.5	1.92	274	2.43
800	120.5	1.92	269.2	1.93	130.5	1.92	279.2	2.1
1000	118.5	1.92	265	1.43	119.5	1.92	278	1.56
1200	117.3	1.92	253	0.98	111.3	1.92	263	1.13
1500	113.4	1.92	225	0.46	103.4	1.92	235	0.66

List of Publications

Conferences

1. Jabbar, M.A.; Khambadkone, A.M. and Liu Qinghua, “Design and Analysis of Exterior and Interior Type High-Speed Permanent Magnet Motors”, *Australasian Universities Power Engineering Conference (AUPEC)*, Sep-2001, Pages: 472-476
2. Liu Qinghua; Jabbar, M.A. and Khambadkone, A.M., “Design optimization of interior permanent magnet synchronous motors for wide- speed operation”, *The 4th IEEE International Conference on Power Electronics and Drive Systems, 2001*. Proceedings Volume: 2 , 22-25 Oct. 2001, Pages:475 - 478
3. Liu Qinghua; Jabbar, M.A. and Khambadkone, A.M., “Design optimization of wide-speed permanent magnet synchronous motors”; *International Conference on Power Electronics, Machines and Drives, PEMD2002*. (Conf. Publ. No. 487) , 4-7 June 2002 Pages:404-408
4. Liu Qinghua; Khambadkone A.M. and Tripathi A. and Jabbar M.A., “Torque Control of IPMSM Drives using Direct Flux Control for Wide Speed Operation,” *IEEE International Electric Machines and Drives Conference*, June

2003, Pages: 188 - 193.

5. Liu Qinghua; Khambadkone, A.M. and Jabbar, M.A., “Direct flux control of interior permanent magnet synchronous motor drives for wide-speed operation” *The Fifth International Conference on Power Electronics and Drive Systems, 2003, PEDS 2003*. Volume: 2 , 17-20 Nov. 2003 Pages:1680 - 1685
6. Liu Qinghua; Jabbar, M.A. and Khambadkone, A.M., “Response surface methodology based design optimisation of interior permanent magnet synchronous motors for wide-speed operation”, *The Second International Conference on Power Electronics, Machines and Drives (PEMD 2004)*, Conf. Publ. No. 498 ,Volume: 2 , March 31, - April 2, 2004 Pages:546 - 551

Submitted for Review

1. Liu Qinghua; Jabbar, M.A. and Khambadkone, A.M., “Design And Experimental Verification Of An Interior Permanent Magnet Synchronous Motor For Wide Speed Operation”, *IEE Journal on Electric Power Applications*

To be Submitted

1. Liu Qinghua; Jabbar, M.A.; and Khambadkone, A.M., “Response Surface Methodology Based Design Optimisation of Interior Permanent Magnet Synchronous Motors for Wide-Speed Operation ”, *IEE Journal on Electric Power Applications*

2. Liu Qinghua; Jabbar, M.A. and Khambadkone, A.M., “Space Vector Modulation based Direct Torque Control of Interior Permanent Magnet Synchronous Motor Drives for the Flux Weakening Operation”, *IEEE Transactions on Energy Conversion*